

METHODOLOGICAL ADVANCES AND APPLICATION OF FUNCTIONAL NEAR-
INFRARED SPECTROSCOPY TO GUIDE CORTICAL STIMULATION FOR PHYSICAL
RECOVERY IN PATIENTS WITH BRAIN INJURY

by

BILAL KHAN

Presented to the Faculty of the Graduate School of
The University of Texas at Arlington in Partial Fulfillment
of the Requirements
for the Degree of

DOCTOR OF PHILOSOPHY

THE UNIVERSITY OF TEXAS AT ARLINGTON

May 2014

Copyright © by Bilal Khan 2014

All Rights Reserved

Acknowledgements

Over the past five years I have received support and encouragement from many individuals. First I would like to thank Dr. George Alexandrakis who has been a mentor and friend. His guidance has made this a thoughtful and rewarding journey. I would like to thank my dissertation committee of Dr. Khosrow Behbehani, Dr. Hanli Liu, Dr. Duncan MacFarlane, and Dr. Mario Romero-Ortega for their support and advice over the past few years. In addition, Dr. Timea Hodics and Dr. Ann Stowe who have both provided valuable guidance in the past couple of years.

While struggling there were others struggling right alongside me. I would like to thank Nathan Hervey for the many hours he spent with me collecting data. I would also like to thank Dr. Tamer Desouky for the advice, help, and support he gave me as we both worked towards completing our doctoral studies.

I would especially like to acknowledge members of my family, because without them I would not have made it this far. I would like to thank my mother, Rubina Khan, for always being there and for her love and support. I would like to also thank my father, Aslam Khan, for his support and heartfelt advice throughout my life. And of course, there is my brother, Hamza Khan, who never fails to make me laugh and bring a smile to my day. I would like to also thank my lovely wife, Sana Muntajibuddin, for her love and support. My family members are the most valuable people to me.

Jazak Allahu Khair and Alhamdulillah.

April 16, 2014

Abstract

METHODOLOGICAL ADVANCES AND APPLICATION OF FUNCTIONAL NEAR-
INFRARED SPECTROSCOPY TO GUIDE CORTICAL STIMULATION FOR PHYSICAL
RECOVERY IN PATIENTS WITH BRAIN INJURY

Bilal Khan, PhD

The University of Texas at Arlington, 2014

Supervising Professor: George Alexandrakis

Non-invasive cortical stimulation used in conjunction with physical therapy can enhance the motor performance of persons with brain injury. Transcranial direct current stimulation (tDCS) is a non-invasive cortical stimulation technique that modulates cortical activation by delivering weak current through a pair of anodal-cathodal (excitation-suppression) electrodes, placed on the scalp over the targeted cortical centers. Recently, application of tDCS over the sensorimotor cortex of stroke patients in conjunction with physical therapy has been shown to induce beneficial plasticity in the injured brain resulting in improved motor performance. However, in all currently reported tDCS-based interventions the locations of electrode pairs used to apply stimulation are kept the same across all patients without taking into account individual differences in their residual sensorimotor networks. The resulting study outcomes remain variable and there is no current consensus as to what electrode pair montage could yield optimal outcomes. These observations indicate the possibility that no single electrode pair montage exists that is optimal for all patients and that a method capable of personalize tDCS electrode placement could be very helpful for improving therapy outcomes.

The objective of this work was to propose and test a new non-invasive cortical stimulation method based on the tDCS principle that could identify the electrode montage maximizing the performance of a given motor task in each subject and thus potentially personalize future treatments. Functional near-infrared spectroscopy (fNIRS) was used as a means of assessing the effects of stimulation on cortical function. Though fNIRS can only measure activation related changes in cortical hemodynamics, it can acquire data concurrently with electrical stimulation, which is not possible with functional magnetic resonance imaging (fMRI) due to electrical interference. Arm muscle activation and motor performance were recorded synchronously with fNIRS during an isometric wrist-flexion task, so as to enable the study of how changes in cortical activation lead to changes in arm muscle activity and subsequent motor performance. The road towards developing this new method for tDCS treatment personalization involved the three following steps:

- 1) Development of a novel fNIRS hardware attachment that we call the brush optode that enabled performing measurements on all subjects, irrespective of high hair densities and dark hair colors, thus resolved this long-standing optical contact problem in the fNIRS field.
- 2) Development and testing of a method to simultaneously measure fNIRS, muscle activity, and arm performance before, during, and after tDCS. The findings of this work demonstrated that tDCS produced cortical perturbations that are measurable with fNIRS. Furthermore, fNIRS produced cortical connectivity maps that helped explain how stimulation-induced changes in the cortex resulted in changes of muscle activity output and arm performance.
- 3) Based on the groundwork performed in Step 2 a novel perturbation tDCS (ptDCS) paradigm was developed for determining a personalized electrode montage with which a subsequent tDCS intervention yields maximal motor task performance improvements during and immediately after stimulation. Unexpected and surprising results were found for the tDCS electrode montage maximizing the performance of an isometric wrist flexion task performed by a group of ten healthy adults, as this optimal montage did not match any of the ones being explored in current literature as a means of improving the motor performance of patients. Furthermore, in five hemiparetic stroke patients

measured with this ptDCS the optimal electrode montage was found to be different in each patient.

The findings from this newly developed ptDCS method present a paradigm shift in current practices as they indicate that not all patients benefit from the same stimulation montage. Rather than treating all patients uniformly, personalization of treatment may be a preferable route for improving therapy outcomes. The above findings are very exciting due to the potential generalized application of the ptDCS method to many other types of brain injury and to the possible performance enhancement of healthy adults. Nevertheless, clinical studies employing ptDCS-guided tDCS treatment, combined with physical therapy where appropriate, would need to be performed in the future to confirm the potential of this method.

Table of Contents

| | |
|---|------|
| Acknowledgements | iii |
| Abstract | iv |
| List of Illustrations | xii |
| List of Tables | xxii |
| Chapter 1 Introduction..... | 1 |
| Chapter 2 Background | 10 |
| 2.1 Brain Response to Injury and its Effects on Motor Function | 10 |
| 2.1.1 Brain Acute Response to Injury..... | 10 |
| 2.1.2 Neuroplasticity Following Brain Injury | 12 |
| 2.1.2.1 Changes in the Synapse..... | 13 |
| 2.1.2.2 Angiogenesis..... | 13 |
| 2.1.2.3 Changes in Neuron Excitation | 14 |
| 2.1.2.4 Maladaptive Neuroplasticity..... | 14 |
| 2.1.3 Motor System and Hemiparesis | 15 |
| 2.2 Promoting Beneficial Neuroplasticity by Transcranial Direct Current Stimulation (tDCS) | 17 |
| 2.2.1 tDCS Effects on Neuroplasticity | 18 |
| 2.2.2 tDCS Effects on Motor Function..... | 20 |
| 2.3 Principles of Functional Near-Infrared Spectroscopy | 21 |
| 2.3.1 Principles of Functional Near-Infrared Spectroscopy..... | 21 |
| 2.3.2 Modified Beer-Lambert Law | 24 |
| 2.3.3 Neurovascular Coupling | 25 |
| 2.3.4 Monitoring Cortical Plasticity Post-Injury with fNIRS..... | 28 |
| Chapter 3 Improving Measurement Success Rate | 30 |

| | |
|---|----|
| 3.1 Introduction | 30 |
| 3.2 Methods and Materials | 32 |
| 3.2.1 Experimental Methods..... | 32 |
| 3.2.1.1 Subjects | 32 |
| 3.2.1.2 The fNIRS Experimental Setup..... | 33 |
| 3.2.1.3 Subject Measurements | 36 |
| 3.2.1.4 FNIRS Signal Filtering, Identification of Source-Detector Pairs with Significant Activation and Image Reconstruction..... | 38 |
| 3.2.1.5 Detected Signal and Image Metrics | 41 |
| 3.2.1.6 Statistical Analysis | 42 |
| 3.2.2 Monte Carlo Simulation of Photon Transport through Hair and Scalp Tissue | 42 |
| 3.2.3 Analytical Model of Photon Transport through Hair and Scalp Tissue | 46 |
| 3.3 Results and Discussion | 52 |
| 3.3.1 Experimental Measurements..... | 52 |
| 3.3.2 Comparison of fNIRS Signal Attenuation Measurements with Corresponding Monte Carlo Simulations and Analytic Model Estimates..... | 62 |
| 3.4 Conclusions | 66 |
| Chapter 4 FNIRS Maps Cortical Plasticity Underlying Altered Motor Performance Induced by tDCS | 69 |
| 4.1 Introduction | 69 |
| 4.2 Materials and Methods | 72 |
| 4.2.1 Subjects..... | 72 |
| 4.2.2 Imaging with fNIRS and tDCS Setup..... | 72 |

| | |
|--|-----|
| 4.2.3 sEMG and Torque Measurement Setup | 76 |
| 4.2.4 Protocol | 77 |
| 4.2.5 fNIRS Signal Filtering and Image Analysis | 80 |
| 4.2.6 sEMG Signal Analysis | 83 |
| 4.2.7 Torque Task Performance Metrics | 84 |
| 4.2.7.1 Initial Speed | 84 |
| 4.2.7.2 Accuracy | 85 |
| 4.2.8 Statistical Analysis..... | 85 |
| 4.3 Results and Discussion | 87 |
| 4.3.1 tDCS Effects on Changes in HbO in the Rest Condition..... | 87 |
| 4.3.2 tDCS Induced Changes in Cortical Activity during an Active Isometric Task | 88 |
| 4.3.3 tDCS Effects on Muscle Activity and Reaction Time..... | 90 |
| 4.3.4 tDCS Effects on Torque Task Performance | 93 |
| 4.4 Conclusions | 98 |
| Chapter 5 Perturbation Transcranial Direct Current Stimulation (ptDCS) | 99 |
| 5.1 Introduction | 99 |
| 5.2 Methods and Materials | 101 |
| 5.2.1 Subjects..... | 101 |
| 5.2.2 Instrumentation Setup | 102 |
| 5.2.3 ptDCS Protocol..... | 104 |
| 5.2.4 fNIRS Signal Filtering and Image Analysis | 107 |
| 5.2.5 Performance, EMG, and fNIRS Metrics | 108 |
| 5.2.6 Neuromuscular Prediction | 108 |
| 5.2.7 Statistical Analysis..... | 109 |

| | |
|---|-----|
| 5.3 Results..... | 110 |
| 5.3.1 Short-Lasting ptDCS-Induced Cortical Effects in Healthy Adults..... | 110 |
| 5.3.2 Overview of ptDCS Montage-Specific Effects on Performance in Healthy Adults | 111 |
| 5.3.3 Comparison of Montage-Specific Effects on Performance Between Subjects..... | 115 |
| 5.3.4 Comparison of Montage-Specific Effects on Muscle Activity Between Subjects..... | 116 |
| 5.3.5 Comparison of Montage-Specific Effects on Connectivity and Cortical Activation Between Subjects..... | 118 |
| 5.3.6 Different Optimal tDCS Montages for Each Stroke Patient..... | 119 |
| 5.3.7 Neuromuscular Prediction | 121 |
| 5.4 Discussion | 122 |
| 5.4.1 tDCS Montage-Specific Performance Differences Between Healthy Subjects..... | 123 |
| 5.4.2 tDCS Effects on Muscle Activity in Healthy Subjects | 125 |
| 5.4.3 tDCS Effects on Cortical Plasticity in Healthy Subjects | 125 |
| 5.4.4 Personalizing tDCS in Stroke Patients | 126 |
| 5.4.5 Risks Versus Benefits of tDCS..... | 127 |
| 5.4.6 tDCS Limitations..... | 128 |
| Chapter 6 Conclusions and Future Work..... | 130 |
| Appendix A Spatiotemporal Relations of Primary Sensorimotor and Secondary Motor Activation Patterns Mapped by FNIR Imaging | 133 |
| Appendix B CCA Algorithm for FNIR Imaging | 162 |
| Appendix C Setup for ptDCS Titration and Scalp Effects | 167 |

| | |
|--------------------------------|-----|
| References..... | 170 |
| Biographical Information | 188 |

List of Illustrations

| | |
|--|----|
| Figure 2-1 A flowchart describing the order of events that happen after brain injury. | 11 |
| Figure 2-2 (a) Location of the primary motor cortex, premotor cortex, and supplementary motor area, and (b) motor area Homunculus..... | 15 |
| Figure 2-3 Pyramidal system. | 17 |
| Figure 2-4 The absorption spectra for oxyhemoglobin (HbO ₂), deoxyhemoglobin (Hb), and water (H ₂ O). The range of near-infrared wavelengths are highlighted in blue showing how HbO and Hb are highly absorbing before this optical window, and water is after..... | 23 |
| Figure 2-5 Banana-Shaped path of photons when introduced at the scalp. Short (r_N) source-detector pairs sample shallower depths, whereas longer (r_F) source-detector pairs sample deeper. | 24 |
| Figure 2-6 Flowchart giving an overview of neurovascular coupling. | 28 |
| Figure 3-1 Pictures of the brush-fiber optode showing (a) the brush-fiber end to be placed on an individual's head, (b) how the brush optode fibers could thread through hair to attain improved optical contact, and (c) the distal end of the brush optode that was designed to attach onto the commercial system's flat-ended fiber bundles. | 34 |
| Figure 3-2 Probe configuration setup on a human subject. The Cz position according to the EEG International 10/20 system and its relation to the location of the probe configuration is shown. The filled 'X' symbols identify the locations of detectors, and the filled circles identify the locations of sources. | 36 |
| Figure 3-3 Schematics of (a) the overall MC simulation setup, and (b) a zoomed-in view of the hair layers, hair follicles, and the placement of a couple of brush fibers among the 64 brush fibers used in the simulations. In (a), the red solid lines are the simulated rays inside the scalp tissue (10 x 10 x 4 mm ³), becoming red dashed lines once they left the scalp tissue. In (b), the short light blue cylinder indicates a brush fiber blocked by hair, | |

and the long light blue cylinder a brush fiber that had good optical contact with the scalp.46

Figure 3-4 A comparison of ΔHbO and ΔHb (a) SNR, (b) CBR, and (c) dAoA between flat and brush optode sets. The single ($p < 0.05$), double ($p < 0.005$), and triple ($p < 0.0005$) asterisks identify the significance in activation metric mean difference between the flat and brush optode measurements.53

Figure 3-5 (a) A scatter plot comparing the activation SNR (dB) of the flat optodes (x-axis) versus that of the brush-fiber optodes (y-axis). The blue circles (short hair subjects) and red circles (long hair subjects) are SNR data points, the red-dashed line indicates the line of equality between the two SNRs, and the red-solid line shows a linear fit through the data. ΔHbO averaged time-plots are shown for (b) a bald subject (0 hairs/mm^2) and (c) a subject with 2.8 hairs/mm^255

Figure 3-6 ΔHbO activation images (μMolar scale) for the same subject (black hair at a density of 2.2 hairs/mm^2) using (a) the flat optodes and (b) the brush optodes. The sources (grey filled circles) and detectors (grey filled Xs) are used to show the source and detector locations. (c) In regions where activation could be detected by both the flat and brush optodes, the latter resulted in significantly higher SNR (shown in dB). There were also locations where the flat optodes detected no significant activation where the brush optodes did (d).56

Figure 3-7 ΔHbO activation images, with color scales in μMolar , for four individual subjects with similar hair densities ($\sim 2.8 \text{ hairs/mm}^2$) and hair lengths (20 – 23 mm), but different hair colors. Source positions are identified by the grey filled circles and the detector positions by the grey filled Xs.57

Figure 3-8 Scatter plots comparing the ΔHbO trend in (a) SNR, (b) CBR, and (c) dAoA for all short hair subjects ($n = 13$) for both the flat optodes (Δ) and brush optodes (X). Similar

plots were made for long hair subjects (n = 4) (d)-(f). The single ($p < 0.05$), double ($p < 0.005$), and triple ($p < 0.0005$) asterisks identify the significance in activation metric mean difference between the flat and brush optode measurements..... 59

Figure 3-9 ΔHbO activation images (color scales in μMolar) for four individual subjects with similar hair color (black), but different hair densities for both flat and brush optode sets. Source positions are identified by the grey filled circles and the detector positions by the grey filled Xs..... 61

Figure 3-10 Scatter plot comparing the ΔHbO trend in (a) SNR, (b) CBR, and (c) dAoA for short hair subjects of all hair colors (n = 13) for both the flat optodes (Δ) and brush optodes (X). The single ($p < 0.05$), double ($p < 0.005$), and triple ($p < 0.0005$) asterisks identify the significance in activation metric mean difference between the flat and brush optode measurements. 61

Figure 3-11 The percent power loss with respect to bald subjects when using either the flat or the brush optodes. Comparison of the experimental (Exp), MC simulated (MC), and analytical formula (AF) results is performed across hair densities for each hair color. 65

Figure 4-1 (a) This image shows the fNIRS sources (dark blue filled circles), detectors (light blue filled X's), and the tDCS electrodes overlaid (dashed squares) on a model brain. The ellipses identify different sensorimotor cortical regions on both the ipsilateral or left (L) and contralateral or right (R) hemispheres over which fNIRS and tDCS take place, such as the supplementary motor area (SMA), premotor cortex (PMC), primary motor cortex (M1), primary sensory cortex (S1), and posterior parietal cortex (PPC). To confirm the approximate locations of these cortical areas without performing fMRI, fNIRS image group analysis was performed for the eight subjects undergoing sensory stimulation of the left hand (b), and performing left hand finger tapping (c), and left hand sequential

tapping (d). Here and throughout the paper, right hemisphere is displayed on the right, left hemisphere on the left as if looking down at the head..... 75

Figure 4-2 This figure is a cartoon representation of the overall instrumentation setup. The protocol display showed the presentation the subjects were to follow, and recorded the torque measurements from the hand device. A trigger (T) was sent from the hand device to the sEMG box which identified the beginning of the task stimulus separately in both data sets. There are 8 sEMG measurements detecting the muscle activity of both arms (dashed lines from arms to sEMG box). Additionally, the box over the person's head represents the placement of optical fiber bundles and tDCS electrodes described in Section 4.2.2. Like the force and sEMG measurements, the 32 x 32 channel fNIRS data was recorded on a separate laptop..... 77

Figure 4-3 The protocol timeline: green boxes indicate rest periods, red boxes indicate wrist-flexion task periods, and the black boxes indicate the time periods before, during, and after tDCS. 79

Figure 4-4 (a) The reaction time, indicated by an arrow, is calculated by the time difference between the stimulus presentation (green lines) and the intercept of the linear regression (red line) of the RMS signal (black line) and the mean rest condition RMS signal (blue line) from the left WF muscle. (b) This figure presents the torque data for a single block during a 50% of the maximum torque. The cursor displacement as torque was applied during the task is represented by the yellow line as it was aimed into the target which was centered at 50% of the maximum torque (dashed white line) with a width of 2.5 % of the maximum torque (two top solid white lines). The data used for the analysis in this study was above a baseline cut-off represented by the bottom, solid white line. Additionally, the peaks and dips are shown by red circles and green diamonds respectively, as these were used to calculate the error variance metric. Moreover, the

initial speed (S_i) was calculated between the baseline cut-off and the first peak (P_1) as indicated by the two white dashes. 86

Figure 4-5 (a) This figure presents HbO concentration changes during the rest condition before, during, and after tDCS for a single subject (Subject 5) at M1 under the anode. After each resting-state condition, measurements were taken during the isometric wrist flexion task (active) task. The times at which these measurements were taken compared to the onset of tDCS are indicated above their respective resting-state measurements. (b) Additionally, the group average change in the baseline Δ HbO at M1 under the anode, inclusive of both hemispheres, is presented as a bar graph. The asterisk represents a significant ($p < 0.05$) change when compared to before tDCS. 87

Figure 4-6 Group analysis of the eight subjects for both the resting-state connectivity and activation images before, during, and after the application of tDCS. The top six (a)-(f) and bottom six (g)-(l) panels are separated by current polarity. The solid red lines connect the cortical areas which were functionally connected, the red dashed squares represent the location of the anode, the black dashed squares represent the cathode, and the semi-transparent black ellipses identify the sensorimotor cortical regions previously defined in Fig. 4-1(a)..... 89

Figure 4-7 The analysis of muscle activity measured by sEMG before, during, and after tDCS for both current polarities. The average time series linear envelope of the sEMG from the left (a) WE and (b) WF for the eight subjects, the statistical analysis of AUC for the left (c) WE and (d) WF, the statistical analysis of the reaction time from the left WF (e) is presented when the anode (red dashed square) was located over the right hemisphere and the cathode (black dashed square) over the left hemisphere. The same is also presented when the electrode positions were switched for the (f) WE and (g) WF average

time-series envelope, AUC statistical analysis for the left (h) WE and (i) WF, and the reaction time for the left (j) WF. The asterisk identifies statistical significance ($p < 0.05$).92

Figure 4-8 Scatter plots for a representative subject's (Subject 3) initial speed in reaching the first peak before (black dots), during (red dots), after (blue dots) tDCS, with correspondingly color coded standard deviations from nine trials, versus the integrated muscle activity (AUC) for the left WE and WF. The polarity of tDCS during these measurements is shown at the top of each figure column. The effect of placing the anode (red dashed square) over the non-dominant (right) hemisphere on initial speed is compared to the AUC of the left (a) WE and (b) WF. The same is represented for the left (c) WE and (d) WF when the tDCS electrode placement is switched. Color coded arrows show the direction of statistically significant changes from before-to-during tDCS (black to red) and from during-to-after tDCS (red to blue). Horizontal arrows show the direction of changes in muscle activity and vertical arrows show the direction of changes in task performance speed. 94

Figure 5-1 TDCS and fNIRS setup. (A) Displays the cortical regions contained within the fNIRS field of view. (B) Displays the tDCS electrode placement (black dashed square), fNIRS source placement (red circles), and fNIRS detector placement (blue Xs) used during the ptDCS protocol..... 102

Figure 5-2 Twenty different tDCS montages used in this study. Locations of each electrode correspond with the diagram at the top of the figure which are the supra-orbital bone (SO), premotor cortex (PMC), primary motor cortex (M1). Red squares represent an anode and black squares represent a cathode..... 105

Figure 5-3 PtDCS protocol. (A) Twenty measurements for each tDCS montage was applied on each subject including a measurement without tDCS, resulting in a two hour

measurement session. (B) Each measurement included 1 minute of rest, 40 s of tDCS during the wrist flexion, and 3 minutes of rest. 106

Figure 5-4 TDCS effects on scalp hemodynamics. (A) Presents cortical response to tDCS (black) versus that of the scalp (blue) when subjects were at rest. (B) Presents cortical response to tDCS (red) versus that of the scalp (blue) when subjects were performing the isometric wrist flexion task. 110

Figure 5-5 Performance analysis between the no tDCS condition (blue), A-tDCS (red), dual tDCS (green), and bi-hemispheric PMC montage (purple). Significance is represented by a color matched asterisk, where (A) presents the Error X RT product, (B) RT, and (C) Error. 117

Figure 5-6 Muscle activity analysis between the no tDCS condition (blue), A-tDCS (red), dual tDCS (green), and bi-hemispheric PMC montage (purple). Significance is represented by a color matched asterisk. 118

Figure 5-7 Cortical connectivity where (A) presents the connectivity before tDCS, (B) presents the connectivity during uni-hemispheric A-tDCS of the contralateral hemisphere, (C) presents the connectivity during bi-hemispheric M1 stimulation, and (D) presents the connectivity during the application of the bi-hemispheric PMC montage. The green outlined boxes represent the area over which fNIRS imaged. The black and red squares indicate the location of the cathode and anode, respectively. 119

Figure 5-8 fNIRS activation metrics. (A) Area of activation (AoA) metrics over the entire fNIRS field of view, and (B) the calculated laterality index (LI). 119

Figure 5-9 Δ HbO activation images during a wrist flexion task with concurrent application of 2 mA for dtDCS and optimal tDCS montages with corresponding task RT, Error, and Error x RT product. Performance metrics which improved significantly are indicated with a bold, red arrow pointing down. 120

Figure 5-10 Resting state connectivity maps for a stroke patients (A) after 0.5 mA for dtDCS, (B) after 0.5 mA for optimal tDCS montage, and (C) a control without tDCS applied. The encircled connections are those connections between cortical areas that are common between the healthy control and stroke patient after optimal tDCS, but are missing from the stroke patient after dtDCS. 121

Figure 5-11 (A) Δ HbO in M1 with increase in tDCS current. (B) EMG AUC with increase in tDCS current. (C) The mapping of Δ HbO in M1 with EMG WF AUC and the NMT properly modeling this relationship. 122

Figure A-1 (a) The stand constructed to relieve the subjects from supporting the entire weight of the fibers. In addition, a soft yet sturdy holder was made to hold the fibers in place on top of the subject's head with good optical contact. (b) Bifurcated fiber bundle source-detector geometry where the 'X' symbols are detectors, and the 'O' symbols are sources, covering a 12 x 8.4 cm FOV. The encircled areas (black ovals) indicate the short distance source-detector pairs used to detect scalp hemodynamics. 137

Figure A-2 (a) A flowchart of the algorithm used to remove source-detector pairs with low SNR due to poor optical contact. (b) In time-averaged activation images produced with data from the remaining source-detector pairs [panel (1)], pixel-wise T-tests were performed with corresponding baseline values to identify regions of activation [panel (2)], which were subsequently clustered according to their similarity in temporal activation patterns [panel (3); S1/PPC orange, M1 blue, background black]. Some clusters were the result of the superposition of activation and background hemodynamics [black and blue striped area in panel (3)], or the superposition of two separate activation areas [blue an orange striped area in panel (3)]. Panel (4) shows cluster-averaged time-series data for activation in the M1 region (solid blue curve), the background region (solid black curve) and the region of overlap (dashed black and blue curve). Panel (5) shows the

corresponding color-coordinated time-series data for the M1 (solid blue curve), S1/PPC regions (solid orange curve) and their overlap (dashed orange and blue curve). 144

Figure A-3 Activation images, having color scales in μMolar , were time-averaged between 5 – 20 s for each task on both visits for all three subjects. The white dashed lines were used to approximately separate the PMC/SMA, M1, S1, and PPC cortical regions, as identified on the far right edge of the figure..... 149

Figure A-4 A time series of activation images, having color scales in μMolar , were time-averaged for every 5 s block over a 30 s period of 15 s stimulation – 15 s rest for a single subject performing all five protocols. The white, dashed lines were used to differentiate between the PMC/SMA, M1, S1, and PPC cortical regions, as identified on the far right edge of the figure. 152

Figure A-5 T-maps and clustered source-detector maps for HbO (left columns) and Hb (right columns) for Subject 1 performing the finger tapping, sensory stimulation, and palm squeezing protocols (rows). The white dashed lines indicate approximate boundaries for the PMC/SMA, M1, S1, and PPC regions. The connected circles in the cluster maps indicate the source-detector pairs that CCA grouped in the same cluster as they had similar time-series activation profiles [Tapping: M1/S1 – red, S1/PPC – blue; Sensory Stimulation: S1/PPC – blue; Palm Squeezing: M1/S1 – red; S1/PPC – blue]..... 154

Figure A-6 HbO T-maps and clustered source-detector maps for sequential finger tapping (left columns) and card flipping (right columns) for each Subject (rows). The white dashed lines indicate approximate boundaries for the PMC/SMA, M1, S1, and PPC regions. The connected circles in the cluster maps indicate the source-detector pairs that CCA grouped in the same cluster as they had similar time-series activation profiles [Sequential Tapping: M1 – red, S1/PPC and SMA/PMC – blue; Card Flipping: M1 and SMA/PMC – red, S1/PPC – blue]. 155

Figure A-7 Group analysis T-maps and the clustered fNIR signals for sequential tapping and card flipping. The white dashed lines were used to approximately separate the PMC/SMA, M1, S1, and PPC regions. The connected circles in the cluster maps indicate the source-detector pairs that CCA grouped in the same cluster as they had similar time-series activation profiles [Sequential Tapping: M1/S1 – red, S1/PPC and M1/PMC/SMA – blue; Card Flipping: M1/SMA/PMC – red, S1/PPC - blue..... 158

Figure C-1 TDCS and fNIRS setup used to determine tDCS effects on scalp hemodynamics and current increase effects on muscle activity..... 168

List of Tables

| | |
|---|-----|
| Table 1-1 Comparison of functional neuroimaging modalities..... | 6 |
| Table 3-1 The obstruction fraction (OF) of brush optodes, the volume fraction of the hair follicles in the scalp (VF_{HF}) and of the hair layers between the scalp and the detector fiber (VF_H), the linear hair density (H_{mm}) and number of hair layers (L), and the volume-averaged μ_a and μ'_s for the scalp and hair layers as a function of hair root density. | 50 |
| Table 4-1 A summary of the cortical activity, muscle activity, and task performance results of the active condition compared to the rest condition. The asterisks indicate those sEMG and torque performance metrics which were found to be significant over the entire group. Those metrics without an asterisk were found significant for at least four of the eight subjects, but were not significant in the group analysis. | 95 |
| Table 5-1 Participants' demographics: protocol, group category, group size, gender, handedness, and age..... | 102 |
| Table 5-2 Performance metrics due to each tDCS stimulation applied over only M1 ordered from most improved to least improved. | 112 |
| Table 5-3 Performance metrics due to each tDCS stimulation applied over only PMC ordered from most improved to least improved. | 113 |
| Table 5-4 Performance metrics due to each tDCS stimulation applied over different M1-PMC combinations ordered from most improved to least improved..... | 114 |
| Table A-1 A summary of the activated cortical regions and their TtPs for each protocol. | 150 |
| Table A-2 A summary of the activated cortical regions and their durations for each protocol. | 151 |

Chapter 1

Introduction

Brain injuries result in the long-term disability of over 600,000 Americans each year (1-4). Specifically, 500,000 are due to stroke (4). Among these patients are those with hemiplegic motor disabilities who attempt to recover motor control, strength, and sensation by means of physical therapy (5-21), pharmacological interventions (22-24), electrical stimulation (25-34), or a combination of these methods (35-44). For example, constraint induced motion therapy (CIMT), a form of physical therapy which constrains the unaffected arm forcing an individual to use their affected arm, has been shown to result in significant improvements in motor function in stroke patients (12, 45, 46). Additionally, botulinum toxin A has shown promise as an antispastic option (22). Recently, non-invasive cortical stimulation methods, such as repeated transcranial magnetic stimulation (rTMS) and transcranial direct current stimulation (tDCS), have shown to be effective in improving motor and task performance in stroke patients (27-29, 35, 47). Unfortunately, in some cases these therapy methods result in little or no improvement (34, 38), which is likely due to the unique underlying physiology of the brain injury in each patient. Therefore, since each patient has their own unique injury type, location and neuroplasticity history post-injury, it becomes difficult to determine a general form of therapy that best benefits an entire patient population. Thus, there is a need to tailor therapy on a patient-specific basis.

The only level of personalization available to date are non-invasive cortical stimulation based therapies which have the advantage of focusing the stimulation over the injured brain area. In prior and ongoing clinical studies the effectiveness of these non-invasive cortical stimulation approaches is examined by using them in conjunction with physical therapy. For example, rTMS combined with physical therapy has improved arm

reach-to-grasp performance (48), and reduced spasticity in stroke patients (35). RTMS is a non-invasive cortical stimulation method which delivers a magnetic pulse, with a spatial resolution of $\sim 1 \text{ cm}^2$, which induces muscle contraction when applied over the primary motor cortex (M1) (27, 44). Applying rTMS repeatedly at low frequencies (0.2 - 1 Hz) inhibits a cortical region; however, when applied at high frequencies ($> 2 \text{ Hz}$) the cortical region stays in an excited state. By using rTMS to either excite the injured hemisphere or suppress the non-injured hemisphere, stroke patients have shown improvement in both performance (48-51) and muscle activity (47). In contrast, tDCS is less topographically specific method than rTMS which uses sub-threshold direct current applied by a pair of electrodes (anode-cathode pair) placed on the scalp to either excite (anode) or suppress (cathode) cortical areas beneath each electrode. However, an advantage of using tDCS is the ability to stimulate during a motor task, as opposed to during the resting state only, and its effects can be different depending on the choice of current polarity. Studies have shown that tDCS during an activity modulates the neural circuitry specific to that task (52), which potentially gives tDCS the ability to have task-specific effects and thus direct cortical plasticity in the desired direction during physical therapy. Therapeutic tDCS is usually applied with current levels between 1 - 2 mA for a 10 - 20 minute period, for which the effects typically last a week (53). Also, tDCS has been used in combination with physical therapy to provide longer lasting improvements in motor performance for stroke patients (30, 31, 34, 37, 39). In particular, bi-hemispheric or dual-tDCS is a specific tDCS electrode montage such that the electrodes are centered over the primary motor cortex (M1) of each hemisphere (34, 37, 54-56). Bi-hemispheric tDCS has been applied on stroke patients in order to suppress the healthy hemisphere and excite the injured hemisphere, in order to improve task performance by normalizing cortical activation laterality (37). However, bi-hemispheric tDCS assumes a specific underlying physiology

and does not take into account the planning centers of the brain. In healthy adults, tDCS applied over the planning centers, such as the prefrontal cortex, has improved motor accuracy (57), whereas application over M1 has improved speed and strength (58).

For both rTMS and tDCS based interventions, the improvement due to therapy has been assessed from three different aspects: increase in contralesional brain activation, increase in muscle activity, and improvement in motor task performance. In particular for simple motor tasks (e.g. finger tapping), brain activation is primarily contralateral to the limb being used in healthy adults. In contrast, hemiparetic patients tend to have brain activity in both hemispheres in order to compensate for the functional loss in the injured hemisphere during a simple motor task. Previous studies have used functional neuroimaging techniques to show a normalization of laterality (32, 59), electromyography (EMG) to measure increases in motor evoked potentials (MEP) (60, 61), and clinical assessment or custom made devices to quantify task improvement due to therapy (62, 63). Unfortunately, most studies only look at one or two of these forms of improvement (37, 64) which may be done simultaneously or separately. However, no individual aspect of improvement gives the whole picture of how motor performance changes relate to changes in muscle and brain activity. Simultaneous, non-invasive measurements of brain activity, muscle activity, and task performance can thus improve the understanding of how stimulation based interventions lead to changes in motor performance. Unfortunately studies of this nature are lacking from the literature to date.

Though the chain of motor control starts with the brain and ends at the limbs, most prior studies only measure the task performance outcome by standard clinical assessment methods (e.g. Wolf Motor Test, Fugl-Meyer, etc.). Unlike clinical assessment methods that often provide higher level function metrics through subjective scores that could depend on the rater, a more recent trend is to perform real-time measurements of

lower level performance metrics such as reaction time, speed, accuracy, force, and torque which can be done with custom made devices in a quantitative and less subjective manner (62, 63). Additionally, surface EMG (sEMG) is a well-established non-invasive method for measuring muscle activity that can help interpret why changes in muscle activity alter motor performance.

As motor control and performance originate from the brain, neuroimaging would also be required to understand how changes in brain function result in changes of muscle activation and ultimately motor control. The current "gold standard" for functional neuroimaging is functional magnetic resonance imaging (fMRI) that has revolutionized the field of neuroscience research, and has brought significant insight into different clinical conditions. Other well established methods include positron emission tomography (PET) and electroencephalography (EEG). Despite the high spatial resolution of fMRI and PET (~ 3 mm) and the high temporal resolution of EEG, all these methods are highly susceptible to motion artifacts. Since the purpose is to evaluate improvements for larger, commonly used actions, an imaging method that is robust to large motions is needed. Additionally, the imaging system would need to be easily accessible for multiple measurements.

Functional near-infrared spectroscopy (fNIRS) is a relatively new, optical method for measuring brain activity which has been shown to be robust to large motions (Appendix A), portable, easily accessible, and safe to use for multiple sessions since it does not use ionized radiation like PET or expose a person to high amounts of electromagnetic radiation like fMRI. A comparison of fNIRS to other non-invasive neuroimaging modalities is presented in Table 1-1. Similar to blood oxygenation level dependent (BOLD) fMRI, fNIRS measures the secondary hemodynamic response to neuronal activity. Additionally, fNIRS has the ability to separate the changes in

oxygenated hemoglobin (ΔHbO), deoxygenated hemoglobin (ΔHb), and total hemoglobin (ΔHbT) unlike BOLD-fMRI. Furthermore, fNIRS has a much higher temporal resolution (up to 100 Hz) than fMRI and PET (1 - 3 Hz). Some of the disadvantages fNIRS has is its limited field of view (FOV) due to the number of available sources and detectors, moderate spatial resolution (~ 1 cm), and ability to only penetrate deep enough to measure cortical activity. The FOV of fNIRS could be resolved by up-scaling fNIRS systems to having more sources and detectors. This could also potentially improve the spatial resolution. However, one of the largest impediments for fNIRS research has been the obstruction of optical fiber bundle contact with the scalp due to hair. This obstacle causes low light detection and low signal-to-noise ratio (SNR) resulting in a low fNIRS measurement success rate. In this work, a solution for the optical contact problem is proposed, which can enable improved fNIRS measurements and facilitate the translation of fNIRS as a very useful neuroimaging tool for guiding therapy.

The need for personalizing physical therapy cannot be achieved by focusing on aspects of improvement in the brain network, muscle activity, and performance separately. Non-invasive cortical stimulation in conjunction with physical therapy has presented beneficial changes in all three previously mentioned aspects, yet has had variable effects due to the underlying physiology of each person. Since non-invasive cortical stimulation can be personalized by changing the location of stimulation, the main idea behind this work was to have simultaneous functional neuroimaging, muscle and performance measures help guide the personalization of non-invasive cortical stimulation locations. This combination of measurement can potentially help guide the personalization of non-invasive stimulation locations by providing a more complete understanding of how changes in the brain network due to the stimulation improve muscle activity and performance. In order to personalize therapy, it would be

advantageous to measure a patient's response to multiple therapy types over a short period of time. Non-invasive cortical stimulation has shown effects within minutes after application in cortical activity, muscle activity, and task performance (60, 65). However,

Table 1-1 Comparison of functional neuroimaging modalities

| | fMRI | PET | EEG | fNIRS |
|----------------------------|---|--|---|---|
| Physiology measured | Blood oxygen level dependent (BOLD) | Metabolism | Neuronal activity | ΔHbO , ΔHb , and ΔHbT |
| FOV | Whole brain | Whole brain | Cortex; Depends on the number of electrodes | Cortex; Depends on the arrangement of available number of sources and detectors |
| Spatial Resolution | ~3 mm | ~3 mm | ~1 cm | ~1 cm |
| Temporal Resolution | 0.5 - 2 Hz | 0.5 - 1.0 Hz | > 1 kHz | up to 100 Hz |
| Motion | Very susceptible | Very susceptible | Very susceptible | More robust than other three modalities |
| Safety | Exposure to high magnetic fields, confined in small space, and cannot have metal on or in the body. | Radioactive dye injected into the body | No radioactive dye or high electromagnetic fields | No radioactive dye or high electromagnetic fields |
| Portability | Not portable | Not portable | Portable | Portable |

reducing the time and current applied will greatly reduce the time that effects last, giving the potential of detecting improvements due to multiple tDCS electrode montages within a single measurement session.

The general need that this work tried to address was the personalization of physical therapy for patients with brain injury. Specifically, the objective for this work was

to use fNIRS and multi-modal motor measurements to guide the tDCS electrode placement on a patient-specific basis which bring about motor performance improvement. The hypothesis is that imaging over primary and secondary sensorimotor cortical areas with a brush-fiber enhanced fNIRS imaging system, and concurrently having sEMG and performance measures can guide the personalization of tDCS enhanced physical therapy, which in turn can bring about significant, patient-specific benefits in the physical recovery of stroke patients. This objective was accomplished with three specific aims.

The first specific aim was focused on increasing the measurement success rate of fNIRS by improving the optical contact between the fiber bundles and scalp for subjects of any hair color or hair root density. Due to the obstacle of hair obstruction many researchers have focused their measurements on subjects with little or no hair, or the prefrontal area (66-68). In this work, a novel brush-optode extension is introduced to overcome hair obstruction. With this new design, the brush-optode was able to thread through hair, thus increasing the chances of having good optical fiber contact with the scalp for a wide range of hair colors and hair root densities. The improvements in fNIRS signal SNR, detected area of activation (dAoA), setup time, and success rate are presented.

The second specific aim was to establish a methodology to relate tDCS induced cortical plasticity to task performance changes in healthy human subjects during and after tDCS using fNIRS, sEMG, and task performance measurements. Previous fMRI studies (53) and one fNIRS study (69) have shown a change in baseline hemodynamics after tDCS. However, due to the interference of electrical stimulation with magnetic fields only one fMRI study (70, 71), to our knowledge, has shown changes in hemodynamics during tDCS. Fortunately, fNIRS does not have this problem, thus this study shows that fNIRS has the sensitivity to detect baseline hemodynamic changes both during and after tDCS.

Additionally, changes in the resting-state connectivity were related to cortical activity, muscle activity, and task performance during an event-related task performed with the non-dominant hand for both possible bi-hemispheric tDCS montages. The ability to successfully combine these different measurements with tDCS brings about the potential to guide therapy.

Finally, the last specific aim was to develop a protocol for determining an optimal, patient-specific tDCS electrode placement that results in improved muscular excitability and task performance during tDCS. To fulfill this aim, fNIRS was used to identify cortical hemodynamic changes that occur during rest or when performing a manual task while brief low current (0.5 mA) tDCS is applied concurrently through electrodes placed over different pair-wise combinations of sensorimotor cortex activation centers. Concurrently, muscle activity and task performance were measured, as established by the previous aim. Within this aim it was first shown when tDCS applied with a lower current (0.5 mA) for a brief time period (40 s), the effects last for a few minutes giving the ability to test different tDCS electrode montages within a single measurement session. Thus, a short experimental protocol that can be completed within two hours was designed. Additionally, using the fNIRS and arm muscle measurements obtained during tDCS, a recursive neural network that predicts hemodynamic activity in sensorimotor cortical centers from the measured muscle activity and vice versa was developed. After processing these measurements with this neural network, patient-specific predictions of how arm muscle tone activity would change at higher tDCS currents that are used during therapy could be made.

In its entirety, this work shows that a novel brush-fiber extension increased the measurement success rate of fNIRS measurements, which in combination with multi-modal motor measurements can guide the use of tDCS for enhancing the effects of

physical therapy. This work sheds light on one way fNIRS can be used for guiding therapy in individuals with brain injuries such as stroke, cerebral palsy, and traumatic brain injury. The ability to guide therapy on an individualized basis potentially give patients a better chance of recovering their lost motor function, thus improving their chances of keeping their jobs, performing routine activities, and staying independent.

The remaining portions of this thesis are divided into five chapters. In Chapter 2 the brain's response to injury, fNIRS as a neuroimaging tool, and tDCS effects on physiology and its application toward motor rehabilitation are briefly reviewed. Chapter 3 then presents a novel solution to the fNIRS obstacle of hair obstruction. Chapter 4 establishes the concurrent use of fNIRS, sEMG, and performance measures as a way of relating cortical plasticity with changes in muscle activity and task performance. Afterwards, Chapter 5 presents a novel protocol for optimizing tDCS electrode montages over the sensorimotor areas of the cortex on a patient specific basis using the measurement setup established in Chapter 4. Finally, general conclusions and future work are presented in Chapter 6.

Chapter 2

Background

2.1 Brain Response to Injury and its Effects on Motor Function

Brain injury can be caused by either internal or external factors as seen in stroke or traumatic brain injury (TBI), respectively. There are five different types of brain injuries that can occur: (1) contusion (bleeding on brain), (2) diffuse axonal injury, (3) anoxic brain injury (no oxygen or not carrying enough oxygen), (4) hypoxic (ischemic - lack of blood flow), and (5) hemorrhagic (vessels rupture - bleed in brain). No matter the type of injury, the brain adapts by isolating the area of injury and then rewiring different brain regions in order to compensate for the loss of function in the injured area. However, this rewiring may be maladaptive and can reduce the functional recovery of limb movement. This section will briefly give an overview of the brain's response to injury and its effects on brain anatomy, and brain and motor function.

2.1.1 Brain Acute Response to Injury

A flowchart summarizing the steps the brain takes in its response to an injury is shown in Fig. 2-1. There are two types of primary injury, a break in the blood brain barrier and necrosis which is cell death. In both cases a toxic environment is created in the extracellular space of the brain near the injury site. In the case of a break in the blood-brain barrier, there can be an infiltration of macrophages, fibroblasts and other cell types, and inflammatory molecules into the site of injury. In the case of necrosis, there can be an increase in free radicals, inflammation, edema, and apoptosis causing altered cell signaling and gene expression. Unfortunately, these toxins can spread from the site of injury increasing the number of neurons injured, thus increasing the damage to the brain.

This study focuses on patients affected by an ischemic stroke. An ischemic injury causes a lack of blood flow to a certain part of the brain. This in turn results in a lack of oxygen and glucose available to the neurons in that brain region. Without oxygen and glucose neurons begin to depolarize, which results in a barrage of action potentials and the release of an excitatory neurotransmitter, glutamate. Due to the lack of oxygen and glucose, these presynaptic neurons are unable to reuptake the extra glutamate released in the synapse. The excessive glutamate then causes the postsynaptic neurons to also fire a barrage of action potentials, which results in an unwarranted amount of calcium and zinc to enter the cells. This large amount of calcium and zinc inside the neuron leads to apoptosis, or cell death by excitotoxicity. Fortunately, the body has a way of isolating these toxins from the rest of the uninjured neurons.

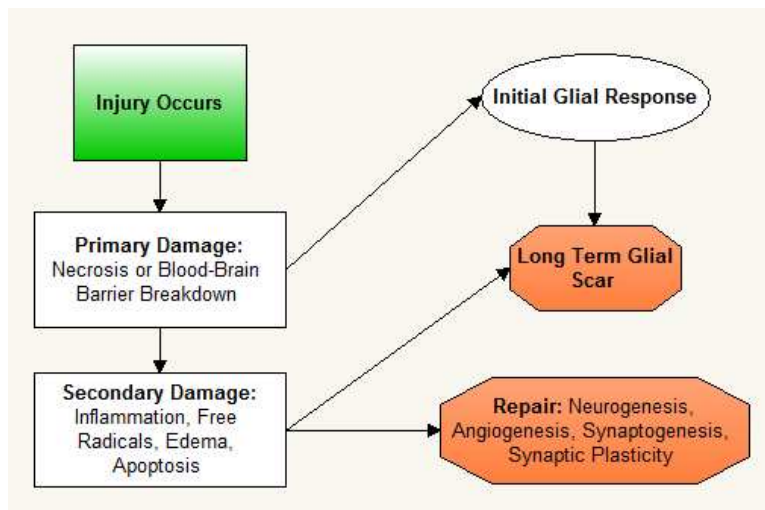


Figure 2-1 A flowchart describing the order of events that happen after brain injury.

As part of the acute injury response, activated glial cells (including astrocytes and microglia) migrate to the injury site in order to isolate toxins from the rest of the uninjured neurons. Glial cells form a tight network known as the reactive glial scar which is both

beneficial and hindering. Initially, the beneficial role of the glial scar helps isolate the site of injury, shields other neurons from excitotoxic and cytotoxic molecules, and repairs the blood-brain barrier. However, the glial scar persists at the injury site producing an inhibitory chemical environment which severely limits axonal regeneration near the injury site, causing the axonal growth cones to recede. Fortunately, the injured area's functional responsibility can be compensated by the rewiring of surviving areas of the brain, known as neuroplasticity.

2.1.2 Neuroplasticity Following Brain Injury

Neuroplasticity is thought to be the foundation of recovery from brain injury (72), and occurs both spontaneously and through training. Spontaneous functional recovery happens soon after injury and appears to involve the reactivation of existing neural pathways, activation of alternative existing pathways, formation of new connections by axonal sprouting or neurogenesis, and consolidation of new neural networks (73). Training-induced plasticity occurs soon after spontaneous plasticity and involves compensation, such that healthy areas that were not responsible for a particular function pre-injury now contribute to that function post-injury (74). The brain network changes according to how a person relearns certain functions. In the case of motor impairment, training may change the motor activation maps. Examples of this type of remapping of the motor cortex has been found in stroke (75, 76). However, neuroplasticity varies depending on the type and location of the injury. Different forms of neuroplasticity including changes in the synapse and angiogenesis are briefly explained next.

2.1.2.1 Changes in the Synapse

After injury, changes in the motor topographical mapping occur in order to have undamaged areas compensate for the damaged area. The basis for this change is synaptogenesis and synaptic plasticity. Synaptogenesis is when new synapses form through dendritic growth (77), increased dendrite arborization (78), and axonal sprouting (72, 77, 79). The increase in the number of synapses allows for re-innervation that can lead to adaptive changes (78). In contrast, synaptic plasticity is the strengthening of existing synapses through the process of long-term potentiation. Importantly, synaptogenesis and synaptic plasticity are key forms of plasticity during training since they are more likely to happen than neurogenesis. However, the recovery of neuronal function is not possible without the recovery of blood flow to the injured area.

2.1.2.2 Angiogenesis

Injury to the brain also causes damage to the surrounding vasculature. The area around the injury affected by compromised vasculature is known as the penumbra and may be a precursor of neuroplasticity (80). In cases where there is a loss of blood flow leading to neuronal death, such as in ischemic stroke, increasing the vasculature improves blood circulation to the injured area (81). The process by which new blood vessels form from pre-existing blood vessels is known as angiogenesis. By returning blood flow to damaged areas it assists in establishing metabolic support (82), in other words more blood flow leads to more available oxygen for the surviving neurons near the injured area. The resulting neuroplasticity post-injury causes changes in neuron excitability of entire cortical regions.

2.1.2.3 Changes in Neuron Excitation

Changes in the excitability of the injured and non-injured hemisphere can affect cortical function by decreasing excitability in the injured hemisphere. A model of inter-hemispheric rivalry has been suggested of analogous areas between hemispheres, where there is hyperpolarization in the injured hemisphere and depolarization in the non-injured hemisphere (83). This shift of activation away from the injured hemisphere indicates a distressed system. Studies have found in chronic stroke patients better recovery when involvement of the injured hemisphere was more predominant than the non-injured hemisphere over time. In other words, more functional involvement of the injured hemisphere related to better outcomes, whereas relying on the non-injured hemisphere for functional involvement related to poorer outcomes. These studies highlight that the brain relearns where synaptogenesis, synaptic plasticity, and axonal sprouting take place. Additionally, other adaptive processes take place, such as angiogenesis and network reorganization changes. As remarkable as neuroplasticity is as a nascent recovery method, it too can have maladaptive consequences.

2.1.2.4 Maladaptive Neuroplasticity

Unfortunately, neuroplasticity post-injury can have harmful effects as seen in seizure disorders post injury, phantom limb pain, and chronic pain. In the case of motor control in hemiparetic patients, the recruitment of the non-injured hemisphere and the decrease in cortical excitability of the injured hemisphere due to nonuse of the affected limb has been considered maladaptive. Most of the projections from the motor cortex control the opposing side of the body (pyramidal system); however, a few projections do control the same side of the body (extrapyramidal system). Post-injury, the fewer projections from the non-injured hemisphere may limit the use of the affected limb. Also,

mirror motions may occur when hemiparetic patients attempt to move their affected limb. Mirror motions are when a hemiparetic patient tries to use their affected limb, but the patient unintentionally performs the same motions with their unaffected limb. This likely happens because the non-injured hemisphere becomes the controller of the limbs on both sides of the body. A brief overview of the axonal tracts from the motor cortex to the limbs, and how injury to these systems lead to hemiparesis is briefly explained in the next section.

2.1.3 Motor System and Hemiparesis

The motor cortex is in the cerebral cortical region of the brain just anterior to the central sulcus (Fig. 2-2a). The lateral area of the primary motor cortex (M1) is divided up into regions for movement of different body parts (Fig. 2-2b). Disproportionately large regions in the maps of M1, known as the Homunculus, are devoted to the body parts involved in the most elaborate and complex movements. Thus, movements of specific body parts are devoted to a specific region in the motor cortex.

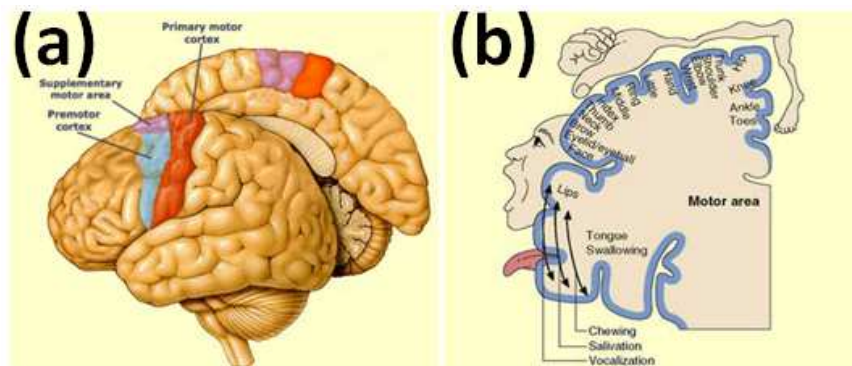


Figure 2-2 (a) Location of the primary motor cortex, premotor cortex, and supplementary motor area, and (b) motor area Homunculus.

The primary motor cortex (M1) is responsible for sending neuronal impulses controlling movement. It also sends impulses to the lower areas of the opposing side of the body via the spinal cord, and works along with the pre-motor cortex and supplementary area to plan the execution of actions. The pyramidal system, presented in the Fig. 2-3, consists of neuronal cell bodies and axons which pass from the cerebral cortex through the brainstem to the spinal cord. In the medulla the pyramidal tract from the right hemisphere crosses the midline to innervate the left spinal cord, and vice versa. Since the pyramidal tract crosses the midline in the medulla, the right hemisphere controls the left side of the body, while the left hemisphere controls the right side of the body.

Many of the axons of the pyramidal tract originate from the M1 region of the brain, thus the left hemisphere of the motor cortex controls the right hand, and the left hemisphere controls the right hand. However, in hemiparetic patients the pyramidal tract is disrupted and the brain adapts, thus weakening their ability to control one side of the body. Hemiparetic patients compensate by potentially using extrapyramidal tracts which connect the M1 to muscles on the same side of the body. Unfortunately, this form of neuroplasticity is maladaptive since there are fewer extrapyramidal tracts to the affected arm and it causes the uninjured M1 area to be responsible for both sides of the body which can result in mirror motions. Fortunately, non-invasive cortical stimulation methods can cause beneficial neuroplasticity and improve motor control by stimulating the injured area (59, 84).

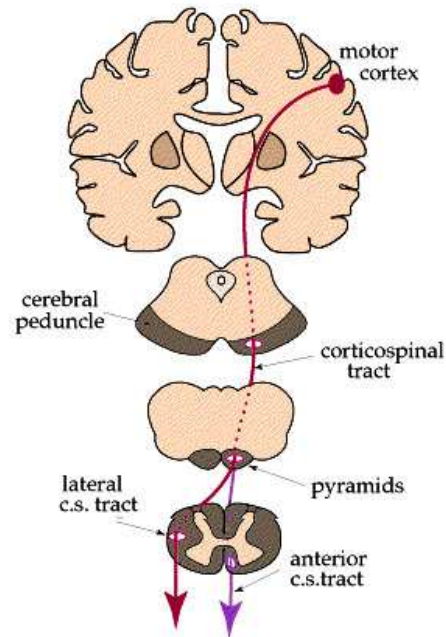


Figure 2-3 Pyramidal system.

2.2 Promoting Beneficial Neuroplasticity by Transcranial Direct Current Stimulation (tDCS)

Guiding neuroplasticity by means of non-invasive cortical stimulation has recently shown beneficial motor performance outcomes in patients with stroke (83). These methods provide the advantage of directly stimulating the injured brain regions, unlike physical therapy which indirectly effects neuroplasticity. Currently, there are two popular methods of non-invasive cortical stimulation, repeated transcranial magnetic stimulation (rTMS) and transcranial direct current stimulation (tDCS). Both methods have fundamental differences. RTMS uses repeated magnetic pulses to stimulate cortical neurons with ~1 mm resolution. Depending on the pulse rate, the neurons are either suppressed (0.2 - 1 Hz) or excited (> 2 Hz). Excitation by rTMS causes action potentials to be sent by the cortical neurons resulting in twitching in the muscles. In contrast, tDCS

uses a pair of electrodes placed on the scalp to inject sub-threshold direct current into the cortex to stimulate cortical neurons. Depending on the current direction, the cortical region is either suppressed (cathode) or excited (anode). However, the injected current is diffuse before reaching the cortex, thus the spatial specificity of the stimulation is in the centimeter range.

Unlike rTMS, tDCS depends on the placement of a pair of electrodes on a person's scalp. This gives the ability to simultaneously excite and suppress different cortical regions. Electrodes commonly used for tDCS are large (25 - 36 cm²), thus causing other regions of the brain to be stimulated which were not meant to be targeted. Currently, there are three popularly studied electrode montages used in conjunction with physical therapy to assist in regaining motor skills in patients with brain injury. One electrode montage, A-tDCS, focuses on exciting M1 in a single hemisphere by placing the anode over M1 and the cathode over the supraorbital bone of the opposing hemisphere. The second montage, C-tDCS, is similar except the cathode is over the M1. The third montage, known as either bi-hemispheric or dual tDCS, places electrodes over M1 of opposing hemispheres. In hemiparetic patients, the anode is placed over the injured M1 and the cathode over the intact M1. Other studies have used tDCS to improve cognitive skills, motor planning, and speech by placing the tDCS electrodes over their respective cortical regions. In the case of motor performance, tDCS has shown improvement for each mentioned montage, yet its effects on cortical plasticity are still unclear.

2.2.1 tDCS Effects on Neuroplasticity

Though the effects of tDCS on neuroplasticity are still under investigation, there has been evidence of tDCS affecting synaptic plasticity and the reorganization of cortical

networks. The current injected by tDCS into the cortex affects the voltage gated channels of the cells in the brain. For example, the blocking of voltage gated Na^+ channels reduced the effects of A-tDCS, since A-tDCS puts the neuron in a more depolarized state and the Na^+ channels are responsible for returning the neuron back to its resting state or re-polarizes the neuron (85). This suggests that tDCS has a long-lasting effect on resting membrane potential of the neurons.

Furthermore, tDCS affects the neurotransmitters and their receptors in the brain that affect synaptic plasticity. N-methyl-D-aspartate (NMDA) receptor, a glutamate receptor, is a key molecular device for controlling synaptic plasticity. The blocking of this receptor in the motor cortical area under the anode or cathode reduced the stimulation effects of both (86). This indicates that the NMDA receptor has a role in neuroplasticity during both anodal and cathodal stimulation. However, the details of its role for either stimulation are still unknown. Additionally, a neurotransmitter, GABA, which is primarily meant for inhibition in the central nervous system and also participates in motor cortical plasticity (87), was found to decrease with A-tDCS. This decrease in GABA during A-tDCS also correlated with a decrease in reaction time and an increase in fMRI BOLD response (87).

The change in fMRI BOLD due to tDCS may be explained by a new hypothesis. This hypothesis, explained through numerical calculations, claimed that tDCS effects on the brain activity do not stimulate neurons, but instead stimulate glial cells (88). Glial cells have many functions, particularly regulating the balance of neurotransmitters and neurovascular coupling. The change in transmembrane potential in glial cells, not neurons, may be the reason for synaptic plasticity and changes in hemodynamics in the cortex due to tDCS. However, this hypothesis has not been complimented with physiological data, and does not explain how current direction changes the glial cells

effects on neuroplasticity. Though tDCS effects on neuroplasticity are still under investigation, studies have shown beneficial reorganization of cortical networks.

In healthy adults and stroke patients alike, tDCS has had polarity dependent effects on cortical plasticity. A-tDCS presented an increase in intra-hemispheric motor cortical connectivity (89), whereas C-tDCS and bi-hemispheric tDCS increased inter-hemispheric connectivity (90, 91). Furthermore, bi-hemispheric tDCS presented a decrease in transcallosal inhibition of the injured hemisphere (90), resulting in increased M1 activity of the injured hemisphere. Interestingly, plasticity did not change with increasing current intensity. These findings show that plasticity can be directed depending on the current polarity and electrode placement. However, directing cortical plasticity can bring about adverse effects in performance (i.e. maladaptive), thus the plasticity must correspond with performance improvement.

2.2.2 tDCS Effects on Motor Function

Stimulation of M1 by tDCS has improved motor performance in both healthy adults and stroke patients. In the case of healthy adults, A-tDCS increased MEP amplitude (61), improved speed-accuracy trade-off (92) and function measured by the Jebsen-Taylor Test (JTT) of the non-dominant hand (30). Additionally, in stroke patients A-tDCS over the injured hemisphere improved reaction time and JTT score (61). In comparison, C-tDCS over the intact hemisphere in stroke patients also gave improvements in reaction time, range of motion, and JTT score (39, 61, 93). Bi-hemispheric tDCS has become a popular montage since one study has shown better improvement in speed-accuracy curve using bi-hemispheric tDCS than in A-tDCS (34). However, this same study presented no significant improvement with A-tDCS which conflicts with findings from other studies that have shown significant improvement with

A-tDCS. Additionally, a couple of studies demonstrated significant improvement in arm function and reaction in both bi-hemispheric and A-tDCS (93, 94). Yet, there were no significant differences between the two montages. These studies focused their discussions on end performance changes, however did not study cortical involvement which can be assessed with functional neuroimaging and may explain differences found between studies.

2.3 Principles of Functional Near-Infrared Spectroscopy

Functional near-infrared spectroscopy (fNIRS) is a relatively new functional neuroimaging method which has been used to monitor cortical activity under different cognitive, motor, and visual paradigms. Since near-infrared light is not highly absorbed by water or hemoglobin, it gives the ability to detect changes in hemoglobin (HbO) and deoxyhemoglobin (Hb) which are secondary effects of increased neuronal activity (95). The following subsections go over the principles of fNIRS, the physiological meaning behind fNIRS imaging, the use of fNIRS in monitoring cortical plasticity, and fNIRS current limitations.

2.3.1 Principles of Functional Near-Infrared Spectroscopy

fNIRS uses the interaction of light with biological tissues, primarily by absorption and elastic scattering. There are two parameters that describe the interaction between light and the biological tissue; the absorption coefficient, μ_a , and the scattering coefficient, μ_s' . The number of absorption events occurring per unit length is defined by μ_a , and the number scattering events occurring per unit length is defined by μ_s' . In tissue, μ_s' is considerably larger, thus the signals measured at a few millimeters or more are dominated by diffuse light.

Most biological tissues are relatively transparent to light in the near-infrared range between 700 to 900 nm which is usually called the “optical window”. In this window, light is able to propagate through tissue thickness of up to 15 cm for brain, breast, and limbs. At longer wavelengths the absorption of water increases steeply, while at lower wavelengths the absorption increase for both oxyhemoglobin (HbO) and deoxyhemoglobin (Hb) blocking all light transmission within a few millimeters as seen in Fig. 2-4.

Since the absorption spectra of HbO and Hb are significantly different from each other within the "optical window", spectroscopic separation of these compounds is possible using a few sample wavelengths. Thus, the changes of HbO, Hb, and total hemoglobin (HbT) can be measured simultaneously. Since a relatively predictable quantity of photons follows a banana-shaped path when light is emitted from the scalp, these photons can be measured at the scalp for functional neuroimaging with a photodetector as shown in Fig. 2-5 (95). Depending on the source-detector distance, the detected light will primarily reach a shallow depth with short source-detector separations and deeper sampling with larger source-detector separations.

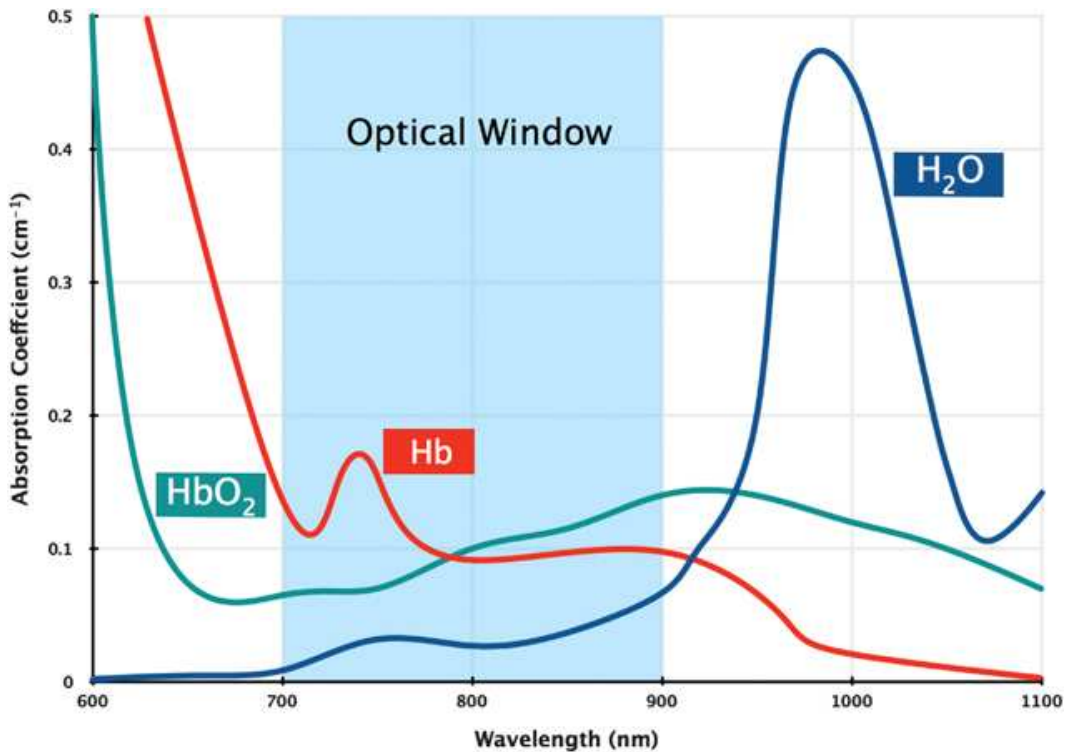


Figure 2-4 The absorption spectra for oxyhemoglobin (HbO₂), deoxyhemoglobin (Hb), and water (H₂O). The range of near-infrared wavelengths are highlighted in blue showing how HbO and Hb are highly absorbing before this optical window, and water is after.

In fNIRS these absorption changes are measured by a spatially distributed array of source-detector pairs with overlapping measurement volumes in order to produce spatially resolved images. By covering large areas of the brain; where spatial coverage is not limited to the activation area, but also including areas that are not involved with the stimulation, contrast between regions of activation and its surroundings can be improved (96-98). These images may display the specific absorption and scattering properties of the tissue, or physiological parameters such as blood volume and oxygenation, or HbO and Hb concentrations (96, 99, 100).

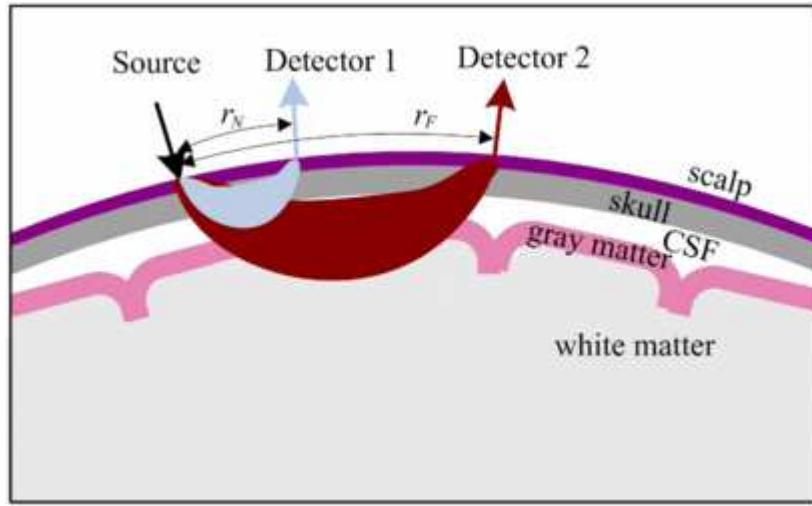


Figure 2-5 Banana-Shaped path of photons when introduced at the scalp. Short (r_N) source-detector pairs sample shallower depths, whereas longer (r_F) source-detector pairs sample deeper.

2.3.2 Modified Beer-Lambert Law

In fNIRS studies, optical absorption cause changes in optical density, which is assumed to be small, and can be modeled as a linear combination of changes in HbO and Hb as given by the modified Beer-Lambert law (MBLL). The MBLL is an empirical description of optical attenuation in a highly scattering medium. Whenever there is a change in the concentration of an absorbing species, the detected light intensity also changes (100, 101). According the MBLL this concentration change can be measured by the light intensity as shown in Eq. 2.1

$$OD = \log(I_0/I) = \epsilon cL = kc \quad (2.1)$$

where OD is the attenuation measured in optical densities, I_0 is the light intensity before the change of concentration, I is the light intensity after the change of concentration, c is the concentration of the absorbing species, ϵ is the extinction

coefficient of the absorbing species, and L is the path length through the tissue. The path length through the tissue can be decomposed into the source-detector separation (d) and the differential path length (DPF), where $L = d * DPF$. The differential path length is either measured for a time-domain or frequency-domain measurements, or estimated when using continuous-wave measurements. The source-detector separation can be measured from the probe geometry. The extinction coefficient of the absorbing species, which can be looked up in literature, and the path length the scattered light traveled through the tissue are two pieces that are contained in the proportionality constant, $k = \epsilon * L$.

In order to determine the contribution of multiple chromophores, such as HbO and Hb, one must take measurements at one or more wavelengths per chromophore to be resolved. For example, by measuring the change in light intensity at two wavelengths, and using the known extinction coefficients of HbO (ϵ_{HbO}) and Hb (ϵ_{Hb}) at wavelengths within the "optical window", one can then separately determine the concentration changes of HbO and Hb by solving the two equations with two unknowns for $\Delta[Hb]$ and $\Delta[HbO]$ as shown in Eqs. 2.2, 2.3, and 2.4, where OD_λ is the optical density at wavelength λ , $\epsilon_{HbO\lambda}$ is the extinction coefficient of HbO at wavelength λ , and $\epsilon_{Hb\lambda}$ is the extinction coefficient of Hb at wavelength λ (96).

$$\Delta[HbO] = (\epsilon_{Hb\lambda_2} * OD_{\lambda_1} - \epsilon_{Hb\lambda_1} * OD_{\lambda_2}) / (L * (\epsilon_{Hb\lambda_2} * \epsilon_{HbO\lambda_1} - \epsilon_{Hb\lambda_1} * \epsilon_{HbO\lambda_2})) \quad (2.2)$$

$$\Delta[Hb] = (\epsilon_{HbO\lambda_2} * OD_{\lambda_1} - \epsilon_{HbO\lambda_1} * OD_{\lambda_2}) / (L * (\epsilon_{Hb\lambda_1} * \epsilon_{HbO\lambda_2} - \epsilon_{Hb\lambda_2} * \epsilon_{HbO\lambda_1})) \quad (2.3)$$

$$\Delta[HbT] = \Delta[Hb] + \Delta[HbO] \quad (2.4)$$

2.3.3 Neurovascular Coupling

HbO and Hb are the main absorbers in tissue which are strongly linked to tissue oxygenation and metabolism (100, 102). Hemoglobin concentrations can act as an

indicator of changes in blood volume and oxygenation of tissues of interest. In the brain, large cerebral arteries, coming from the circle of Willis, branch out into smaller pial arteries and arterioles. The pial arteries travel along the subarachnoid space and branch out into arteries and arterioles which penetrate into the brain. These penetrating arteries and arterioles consist of an endothelial cell layer, a smooth muscle cell layer, and an outer layer consisting of collagen, fibroblasts, and perivascular nerves (103). Penetrating vessels are separated from the brain by the Virchow-Robin space which consists of cerebral spinal fluid. As the vessels penetrate deeper into the brain the Virchow-Robin space disappears and the vascular basement membrane comes into direct contact with astrocytic end feet. These capillaries consist of endothelial cells, pericytes, and the capillary basal lamina on which astrocytic feet are attached (103-105). The endothelial cells play an important role in the regularization of vascular tone by releasing potent vasoactive factors (103).

Neurovascular coupling is caused by the close interaction between neurons, astrocytes, and vascular cells. The mechanisms underlying neurovascular coupling include ions, metabolic by-products, vasoactive neurotransmitters, and vasoactive factors released in response to neurotransmitters (103-105). Under normal conditions or at resting state the brain relies almost exclusively on glucose oxidation (105-108). A physiological increase of neuronal activity caused by voluntary movement increases cerebral metabolic rates for oxygen and glucose, and increases cerebral blood flow (109-111). The brain has little energy reserves and depends on a continuous supply of glucose and oxygen through cerebral blood flow. As neurons depolarize, the dendrites release neurotransmitters such as glutamate and GABA. Glutamate is responsible for the majority of the synaptic transmission within the cerebral cortex. The uptake of glutamate from the synaptic cleft by astrocytes stimulates aerobic glycolysis in the astrocytes. For

the uptake of every three Na^+ and one glutamate molecule, one glucose molecule also enters the astrocyte. Neurons, unlike astrocytes, cannot uptake glucose, thus neurons depend on astrocytes for glucose uptake (108). The glycolytic processing of a glucose molecule in the astrocyte results in two lactate molecules which are taken in by a neuron and converted into ATP with the presence of oxygen (111). Vasoactive factors released in response to neurotransmitters can also cause vasodilation, such as the activation of glutamate receptors. In this case, intracellular Ca^{2+} of astrocytes, associated with glutamate receptor activation, causes Ca^{2+} -dependent enzymes to produce vasodilators, such as nitric oxide (NO) (103, 104). With increased neuronal activity there is an increase of glutamate release, thus causing an increase of cerebral blood flow, glucose uptake by astrocytes, and glucose availability for astrocyte uptake. Increased blood flow and volume can also be caused by ions, K^+ and H^+ , which are generated by the extracellular ionic currents caused by action potentials and synaptic transmissions, causing the smooth muscles in arterioles to hyperpolarize and relax. Increased blood flow can also be caused by neurotransmitters, such as acetylcholine released by active neurons, which cause the smooth muscles in arterioles to relax (103, 104). With the increase of cerebral blood flow there is also an increase of oxygen availability. With the increased uptake of glucose and availability of oxygen, neurons are able to produce more ATP giving them more energy during stimulation. Surrounding capillaries deliver HbO which releases its oxygen and takes away the CO_2 , thus converting it to Hb .

In summary (Fig. 2-6), brain activity is associated with a number of physiological events. Neuronal activity is fueled by glucose metabolism, thus increases in neuronal activity increase glucose and oxygen consumption. The reduction of glucose and oxygen in the capillary bed stimulates the brain to increase local arteriolar vasodilation. The

arteries dilating results in an increase of local cerebral blood flow and cerebral blood volume, which is a mechanism known as neurovascular coupling.

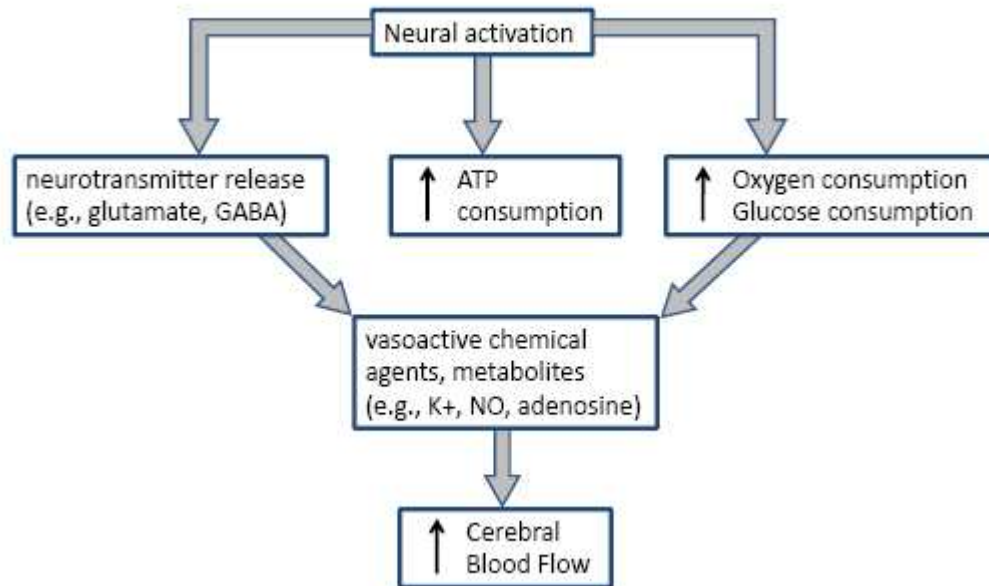


Figure 2-6 Flowchart giving an overview of neurovascular coupling.

2.3.4 Monitoring Cortical Plasticity Post-Injury with fNIRS

fNIRS is a relatively new technology, thus not many studies have used it to image sensorimotor cortical plasticity in patients with brain injury. However, most fNIRS studies involved with monitoring changes in cortical plasticity focus on stroke patients (112-116). These studies have found a positive shift in cortical activation from the contralesional hemisphere to the ipsilesional hemisphere.

However, the limited number of studies using fNIRS to measure neuroplasticity post-stroke may be due to a few limitations of current fNIRS systems. Due to its novelty, there isn't a large number of experts nor is there a standardized method for analyzing

fNIRS data. Thus, neuroscientists or neurologists shy away from using fNIRS without an automated method of analyzing the data. Additionally, there are a few drawbacks with fNIRS technology: 1) problems with hair obstruction, 2) low spatial resolution, 3) limited FOV, and 4) limited depth penetration. This work does not attempt to resolve all these issues, however it does focus on the issue of hair obstruction. This problem may be the most important since it drastically limits the number of subjects that can be successfully measured based on hair color and hair density.

Chapter 3

Improving Measurement Success Rate

3.1 Introduction

Non-invasive sensing and imaging technologies applied to the investigation of brain function in health and disease are of great utility to both clinicians and basic scientists alike. In current clinical settings, the most widely disseminated technologies are electroencephalography (EEG), functional magnetic resonance imaging (fMRI) and positron emission tomography (PET) (117-119). Each of these technologies comes with its own strengths and limitations. EEG detects the electrical activity from evoked potentials of cortical neurons at high temporal resolution (milliseconds) but cannot detect electrical signals from deep within the brain (117). Both PET and fMRI can image the entire head volume and provide information about brain function, but with a temporal resolution of 0.5 seconds or longer (119, 120). In addition, all these modalities require relative immobilization of the subject and are sensitive to motion artifacts. Recently functional near infrared spectroscopy (fNIRS) has been found to be a useful alternative technology for studying brain function in healthy subjects (100, 121-123) and ones affected by a wide range of different pathologies such as stroke, depression, cerebral palsy, and Alzheimer's (116, 124-127). Though this optical technology is limited to cortical imaging at a modest spatial resolution of about 1 cm (97), it can potentially offer high activation-related signal detection sensitivity at high temporal resolution, in the hundreds of milliseconds (128), and a relative robustness to motion artifacts (129).

fNIRS detects the changes in light absorption and scattering in tissue caused by changes in concentration of oxyhemoglobin (ΔHbO) and deoxyhemoglobin (ΔHb) secondary to neuronal activity, through a neurovascular coupling mechanism that is currently under investigation (130). Though fNIRS can measure the slow hemodynamic

response elicited by neuronal activity that correlates with corresponding fMRI measurements (100), it is often the case that the activation signal-to-noise ratio (SNR) in fNIRS is low due to poor optical contact between the optical fibers that deliver and collect near infrared (NIR) light to and from the scalp (131).

The main suspected contributor to poor optical contact is the subjects' hair, especially for dark hair colors and high hair root densities (131), though to our knowledge, no systematic studies have been performed to date to assess quantitatively the effect of these factors on the fNIRS SNR. In addition, during setup of the optical fibers onto a person's head, the hair needs to be parted in order for the optodes to have good optical contact with the scalp, which is time consuming and becomes more difficult for higher spatial resolution studies requiring denser probe geometries. Due to these limitations, many studies have been restricted to the prefrontal cortex or to measurements on subjects with low hair density (66-68).

In this work, we present a novel brush-fiber optode that was used as an attachment to the light collection end of the detector fiber bundles of a commercial fNIRS continuous wave (CW) imaging system to help overcome poor optical contact while also improving measurement setup times. The brush optode consisted of a bundle of optical fibers that were kept loose, like a hair brush, so that individual optical fibers could easily thread through a subject's hair and reach the scalp. In comparison to our previous work [22], in which the brush-fiber optode was tested on a tissue-simulating phantom and a single subject, measurements in this study were performed with the brush-fiber attachment in place, and without it, on subjects with a wide range of hair colors and hair root densities. Comparisons in measurement setup times, the activation SNR of detected fNIRS time-series signals and the contrast to background ratio (CBR) and detected area of activation (dAoA) of reconstructed images were performed between measurements

with and without the brush fiber attachments for each subject. Monte Carlo (MC) simulations were also performed for different hair colors and densities, for both brush and traditional solid fiber bundle optodes, to model the attenuation that NIR light experiences as it travels through layers of hair and hair roots embedded within a few millimeters (mm) into the scalp. Lastly, an analytical formula was derived to mathematically estimate light power losses due to hair obstruction. This formula takes into account the successive attenuation losses that NIR light experiences as it exits the scalp, travels through hair layers, and enters the light collecting optodes. This work presents, to our knowledge, the first attempt to quantify the effect of hair on NIR light signal attenuation and proposes a novel tool to help resolve this common problem in the fNIRS field.

3.2 Methods and Materials

3.2.1 *Experimental Methods*

3.2.1.1 Subjects

Seventeen subjects [4 long hair (female) and 13 short hair (male); 25.06 ± 6.16 years old; 1.73 ± 0.08 m; 63.31 ± 12.59 kg] were included in this study. Among these subjects, two were bald, four had blonde hair, four had brown hair, and seven had black hair. Both bald subjects originally had black hair. The subjects' hair densities were in the 0 – 2.96 hairs/mm² range, which spanned the known hair density range found in a previous large population study (132). For analysis purposes, the hair densities were binned into 0 hairs/mm² (bald subjects), 1.8 hairs/mm² (1.7 – 1.9 hairs/mm²), 2.2 hairs/mm² (2.1 – 2.3 hairs/mm²), and 2.8 hairs/mm² (2.7 – 2.96 hairs/mm²) categories. Among these subjects, three were binned with a hair density of 1.8 hairs/mm², four with 2.2 hairs/mm², and eight with 2.8 hairs/mm². Both of the bald subjects had hair root densities in the 1.8 hairs/mm² range. For the subjects measured, there was no obvious

correlation between hair density and hair color. The long hair subjects had hair lengths in the 220 – 420 mm range while the short hair subjects had lengths in the 0 – 30 mm range. All four long haired subjects had hair densities in the 2.8 hairs/mm² category. All subjects were right handed and had one repeated measurement within 2 – 3 weeks of their first visit. None of the subjects had dyed hair or had used any cosmetic hair products when fNIRS measurements were done. The studies were performed under the approval of the University of Texas at Arlington Institutional Review Board protocol (IRB No.: 2011-0193).

3.2.1.2 The fNIRS Experimental Setup

The brush optodes (Fig. 3-1) were used as extensions that were attached to the flat end tips of the flat-faced optodes of a commercially available fNIRS system (CW-6, Techen Inc., Milford, Massachusetts). The individual fibers in the brush optodes were made of a low-cost polymethyl methacrylate polymer (TheFiberOpticsStore.com, North Oaks, Minnesota), and had a numerical aperture (NA) of 0.41 in air. Each fiber was 0.25 mm in diameter, and 64 of them were included to form a 3 mm diameter optode [Fig. 3-1(a)], which could expand up to about 4 mm in diameter when threaded through hair [Fig. 3-1(b)]. Each bundle of brush fibers was placed into a cylindrical envelope of black cladding to prevent ambient light from overwhelming the detected signal, exposing only 3 mm from the fiber tips. The distal end of the attachment was polished flat and was encased in a holder [Fig. 3-1(c)] that enabled abutting the commercial system's flat-faced fiber bundles face-on against the brush optode extensions. In prior work, we have shown through MC simulations that the expansion of the brush optode diameter due to threading through hair did not significantly affect the spatial resolution in the resulting reconstructed images, while tissue simulating phantom experiments indicated a loss of -2.54 ± 1.53 dB

due to imperfect optical coupling between the brush fiber optode attachments and the flat-faced fiber bundles (133). These attachments were secured in place with a rubber band. The holder attachments were made from acrylonitrile butadiene styrene (ABS) at low cost using a 3D printer (Stratasys, Eden Prairie, Minnesota). In comparison to the brush optodes, the commercial system's flat-ended fiber bundle optodes consisted of glass fibers, had an NA of 0.44 in air, and were 3 mm in diameter.

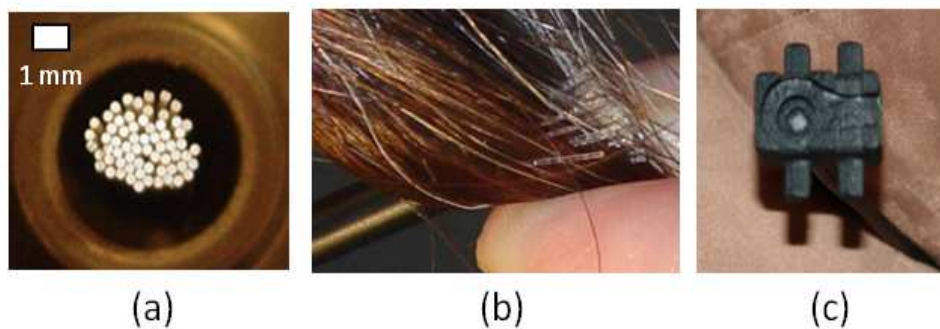


Figure 3-1 Pictures of the brush-fiber optode showing (a) the brush-fiber end to be placed on an individual's head, (b) how the brush optode fibers could thread through hair to attain improved optical contact, and (c) the distal end of the brush optode that was designed to attach onto the commercial system's flat-ended fiber bundles.

FNIRS measurements of the sensorimotor cortex during finger tapping were performed with and without use of the brush optode attachments so that comparisons could be made in the quality of the resulting fNIRS signals and images. In these measurements, 12 laser sources emitted light at 830 nm and 12 at 690 nm, such that each of the source optical fiber bundles carried both wavelengths of light at each source location simultaneously. In the CW-6 system, the source fiber bundles were of 0.25 mm diameter as they consisted of only two single-mode fibers, one for each of the two illumination wavelengths. These source fibers were thin enough to easily thread through

hair and be placed in contact with the scalp. The brush optode attachments were applied to the 3 mm diameter detector fiber bundles only. There were a total of 24 detectors arranged in parallel rows (Fig. 3-2) such that the first (1.5 cm), second (2.12 cm), and third (3.35 cm) nearest neighbor detectors were used to detect the reflected light from the respective neighboring sources. This layout resulted in a total of 112 total source-detector pairs. The source and detector fiber bundles were firmly attached onto a subject's head by Velcro straps. Since the weight of the flat optodes at the distal end of brush optode attachments pulled the brush optodes off the scalp, the brush optodes were placed in-between slits formed in a piece of airtex foam to keep the brush optodes upright so as to stabilize their placement on the scalp.

The fNIRS probe placement was such that the mid-right edge of the probe holder was 2 cm to the left of the C_z position of the EEG International 10/20 system (Fig. 3-2) (117). Since activation had been located between 2 cm and 7 cm to the left of the center of the head (125), this placement enabled monitoring of activation in the contralateral primary sensorimotor region of the cortex due to right hand finger tapping. Activation at different locations within the probes' field of view (FOV, 10.5 x 6 cm) was monitored simultaneously by all source-detector pairs, as the CW-6 system enabled all lasers to be on at the same time by multiplexing them with distinct modulation frequencies (6.4 – 12.6 kHz with an increment of 200 Hz). The detected back-reflected light was demodulated and sampled at a rate of 32.5 Hz. In addition to measuring the cortical hemodynamics by optical means, the finger tapping pattern was simultaneously measured by an in-house made, capacitance-based, tapping board that produced a bi-level voltage for each tap, and the respiration of each subject was monitored by a respiration belt (Sleepmate Technologies, Glen Burnie, Maryland). These measurements were fed into the CW-6, digitized by an analog-to-digital converter, also sampled at 32.5 Hz, which resulted in a

common time base for both optical and auxiliary data. The reference respiration signal was subsequently filtered out of the measured time-series activation data as described below.

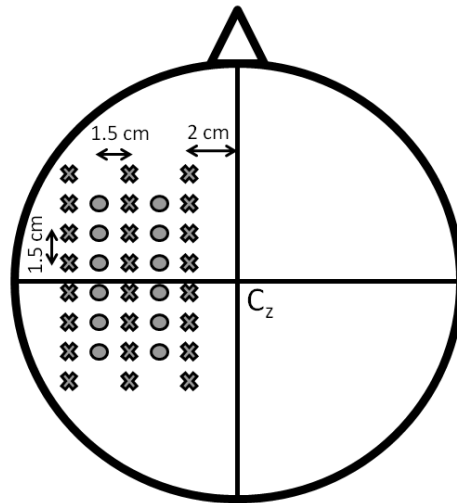


Figure 3-2 Probe configuration setup on a human subject. The C_z position according to the EEG International 10/20 system and its relation to the location of the probe configuration is shown. The filled 'X' symbols identify the locations of detectors, and the filled circles identify the locations of sources.

3.2.1.3 Subject Measurements

The subjects sat up straight with their heads resting back in a quiet, dimly lit room as a PowerPoint animation on a computer screen guided them through the finger tapping protocol. No set tapping frequency was required of the subjects. Thus, the tapping frequency was self-paced, which resulted in average finger tapping rates in the 1–2 Hz range. Tapping consisted of moving all fingers of the right hand, while keeping the left hand relaxed. The subjects touched the tapping board while tapping and rested their hand on the board during the no-tapping intervals. The data acquisition protocol

consisted of a 180 s baseline (no tapping), immediately followed by a series of eight consecutive epochs of 15 s of tapping and 25 s of rest, and ended with a 20 s baseline measurement, resulting in a total acquisition time of 520 s (8 min. 40 s). For each visit, a 520 s protocol was done for each one of the flat and brush optode sets. After the fNIRS measurements, the hair density and the number of hair layers blocking the optodes was estimated for each subject from hair clippings. The local hair density was measured by first cutting and then counting those hairs originating from the scalp within a 5 mm radius from five different locations within the measured FOV. The average value counted from all five sampling locations provided an estimate of the local hair density for each subject. Cumulative results for hair densities binned in 1.8 hairs/mm², 2.2 hairs/mm², and 2.8 hairs/mm² categories are reported in the Subjects section. Subsequently, the number of hair layers blocking a single optode was also measured. The measurement was performed by placing a single flat optode on the scalp after combing away as many hairs as possible. A plastic slide was placed under the hairs blocking the optode and the hairs were held down with tape and were cut. The hair sample was then carefully removed and the number of hair layers and hairs at each layer was counted with tweezers. This was repeated at 5 different locations within the measured FOV. These measurements provided an estimate of the number of hair layers blocking the optode from touching the scalp. For short haired subjects the measured number of hair layers and the linear density of hair on top of the scalp increased with hair root density as shown below (Table 3-1, Column 4).

Additionally, hair affected the number of brush fibers that could have proper optical contact with the scalp. Since the fibers of the brush optodes that were not blocked by hair left a short-lived indentation on each subject's scalp, the percentage of brush fibers blocked by hair was determined by counting the number of indentations caused by

each brush optode. The percentage of obstructed fibers counted as a function of hair density is reported below (Table 3-1, Column 2). Notably, all fiber indentations of the brush optodes (64 fibers) were accounted for on the bald subjects.

3.2.1.4 fNIRS Signal Filtering, Identification of Source-Detector Pairs with Significant Activation and Image Reconstruction

In addition to detecting evoked hemodynamic changes, fNIRS is sensitive to cerebral hemodynamic fluctuations of systemic origin. Such systemic fluctuations can be caused by cardiac pulsation, respiration, and Mayer waves (134, 135). For typical motor activation protocols, the cortical hemodynamic response can be found in the 0.01–0.4 Hz frequency range, while physiological artifacts, such as cardiac pulsation, can be found between 0.8–2.0 Hz, respiration in the 0.1–0.3 Hz range, and Mayer waves at ~0.1 Hz or lower (134, 135). Because there is a significant overlap between the frequency spectra of respiration and Mayer waves and of the hemodynamic response due to brain activity, band-pass filtering is not effective in removing such physiological artifacts. Recent studies have used time-domain systems (136), multi-distance probe geometries (137), component analysis (138), adaptive filtering (139), or some combination of these (125) to remove physiological artifacts.

This study used a combination of band-pass filtering, adaptive filtering, and component analysis to filter the fNIRS signals (125). The first step in the signal filtering was to band-pass filter fNIRS signals from all source-detector separations and the respiration belt measurements in the 0.01 and 0.4 Hz range as this frequency window was found to contain the power spectrum of activation signals as well as that of respiration and Mayer waves. Cardiac pulsation, which was in the 1 Hz range, was filtered out of this window. Subsequently, a combination of an adaptive least mean

square (LMS) filter and principal component analysis (PCA) was used to remove global fluctuations from the band-pass filtered fNIRS signals (125). The respiration belt measurement was then used as the adaptive filter noise reference for the removal of respiration noise artifacts from the fNIRS signals as previously reported [11].

Moreover, not all flat-faced and brush fiber bundles maintained good optical contact due to motion or obstruction by hair, thus propagating noise into the reconstructed images. Noisy source-detector pairs which had a signal-to-noise ratio below a determined threshold due to hair obstruction were removed from further analysis (140). The signal-to-noise ratio ($SNR_{s,d}$) values for all source-detector pairs were determined by Eq (3-1):

$$SNR_{s,d} = 10 \times \log(P_{s,d} / P_d) \quad (3-1)$$

where $SNR_{s,d}$ was the detected signal-to-noise ratio value for a specific source (subscript s) and detector (subscript d) pair, $P_{s,d}$ was the detected light power within the 0.01 Hz to 0.4 Hz frequency range for a specific source-detector pair after being filtered, and P_d was the detected power within the same frequency range for a dark measurement (no light source on) with the specific detector. The threshold was identified by first sorting the $SNR_{s,d}$ of source-detector pairs into groups by their corresponding source-detector distances. Each group was then split into an original set which consisted of all the $SNR_{s,d}$ values for that group, and a pruned set which initially consisted of the original set minus the smallest $SNR_{s,d}$ value for that group. If the mean or standard deviation of the pruned set and original set were not significantly different ($p < 0.05$), as determined by the T-test and F-test respectively, then the smallest $SNR_{s,d}$ value was removed from the data set being pruned, and the procedure was repeated until the pruned group's mean or standard deviation was significantly different ($p < 0.05$) from the original set. The last $SNR_{s,d}$ value removed was saved as a threshold candidate. The process was repeated

for each group of source-detector pair distances, and the minimum value among the saved $\text{SNR}_{s,d}$ threshold candidates was the applied threshold for the whole dataset. The source-detector pairs below the threshold that were removed for the flat optodes (4.57 ± 0.77 dB) and brush optodes (5.73 ± 0.85 dB) were shown to have significantly smaller $\text{SNR}_{s,d}$ values than those of the flat optode (28.31 ± 2.93 dB) and brush optode (34.78 ± 3.64 dB) source-detector pairs kept for analysis. Furthermore, head movements were noted as each subject performed the protocol. Those 40-s tapping-rest intervals which contained head movements were removed from further analysis.

Reconstruction and visualization of fNIRS activation images resulting from the acquired reflectance data that passed the $\text{SNR}_{s,d}$ selection criteria described above was performed by the open-source HomER software implemented in MATLAB (141). In this software activation images are reconstructed by use of the Tikhonov perturbation solution to the photon diffusion equation (142, 143), which employs a regularized Moore-Penrose inversion scheme (142, 143). The reconstructed, two-dimensional images (21 x 21 pixels) represented maps of ΔHb and ΔHbO on the cortical surface, within the detector's FOV (Fig. 3-2). Images were reconstructed for every 0.03 s time interval. After the fNIRS images were reconstructed, regions of activation were determined by a general linear model (GLM) and the T-test in an approach similarly used in fMRI image analysis (144). The GLM treats an entire time-series of a single pixel as a linear combination of model functions plus noise which are defined in a model matrix. In this case the model matrix contained a sum of gamma functions convolved with a box function to model the hemodynamic response due to finger tapping (145), and a DC component to represent the background hemodynamic fluctuations (144). From the estimated amplitudes and estimated error variance, a T-value and a p-value was calculated for each pixel. This process was repeated for the time-series data of each image pixel. With the application of

the Bonferroni corrections for multiple comparisons (146), a pixel with $p < 0.0001$ was considered to have significant cortical activity due to finger tapping. The ΔHbO and ΔHb activation images were then created from the calculated activation amplitudes for each pixel.

In addition to identifying regions of significant activation in the reconstructed images, similar analyses were performed at the detector level for both flat-faced and brush optode measurements. Using the GLM, the T-test, and the Bonferroni correction for multiple comparisons, source-detector pairs with significant activation ($p < 0.0001$) were identified in each measurement data set.

3.2.1.5 Detected Signal and Image Metrics

fNIRS signal and image metrics were used to quantify any improvements occurring when using the brush optodes versus the commercial flat-ended fiber bundles. An activation SNR metric for fNIRS signals at the detector level was computed for the source-detector pairs that had significant activation. The activation SNR was defined for a specified source-detector pair (Eq. 3-2) as the ratio of β to σ , i.e. the amplitude of the hemodynamic response as found from the GLM applied on the individual detector time-series data (144) divided by the standard deviation of the detected baseline hemodynamic fluctuation signal. It is important to note that the $\text{SNR}_{s,d}$ defined in Eq. 3-1 is different from the SNR defined in Eq. 3-2. SNR will refer to the activation SNR (Eq. 3-2) from this point onward. After creating the activation images and determining the regions of activation by use of the aforementioned GLM and T-test on each image pixel, the CBR of the activation images was found with Eq. 3. In that equation μ_A was the mean value of the activation regions, μ_B was the mean value of the background regions, and σ_B was the standard deviation of the background region values.

$$\text{SNR} = 10 \times \log(\beta / \sigma) \quad (3-2)$$

$$\text{CBR} = (\mu_A - \mu_B) / \sigma_B \quad (3-3)$$

Additionally the dAoA was determined by the summation of the pixel areas with activation.

3.2.1.6 Statistical Analysis

One-sampled T-tests or Wilcoxon Signed-Rank tests were performed, using SAS 9.1 (SAS Institute Inc., Cary, North Carolina) to see if there was a significant difference ($p < 0.05$) in SNR, CBR, and dAoA means between visits and between the use of the flat and brush optodes. Prior to testing the significant difference of the means between groups, the F-test was used to assess if the variances of both groups being tested were significantly different from one another. In cases where the variance of flat-faced versus brush optode measurements was found to be significantly different ($p < 0.05$), the Wilcoxon Signed-Rank test was used instead. Such instances occurred when comparing the CBR and dAoA for the overall comparison of the ΔHb and ΔHbO data in subjects with black hair and in subjects with the higher hair densities of 2.2 and 2.8 hairs/mm². All other cases used the T-test to compare between group means. The null hypothesis was defined as a zero change between visits or between uses of the two different optode sets.

3.2.2 Monte Carlo Simulation of Photon Transport through Hair and Scalp Tissue

The transport of NIR light through layers of hair and the scalp, which contained hair roots, was modeled for different hair colors and densities by MC simulation software (FRED, Photon Engineering LLC, Tucson, AZ). The purpose of these simulations was to

obtain estimates of the attenuation NIR light experienced from the point it entered the scalp to the point it was collected by an optode.

NIR photon transport, at an assumed wavelength of 830 nm, was simulated for hair laying on top of a block of scalp tissue [$10 \times 10 \times 4 \text{ mm}^3$ (length x width x height)] embedded with hair follicles (Fig. 3-3). Photons were injected from the bottom side of this tissue block by a virtual source at half angles of 0° to 90° , mimicking the fact that the angular distribution of photons arriving there after having traveled deeper in the brain would be isotropic. To emulate a detection fiber bundle, a virtual optode was placed on top of the hair and was simulated to collect light within a cone of 18° half-angle to match the NA of these fibers in air. For the case of flat-faced fiber optodes, a virtual detector [Fig. 3-3(a), blue circle] was placed on top of the highest hair layer and was simulated as a pure absorber of photons with a 3 mm diameter circular aperture to emulate the fiber bundles used for the human measurements. Similarly, a brush fiber optode was simulated to consist of 64 individual fibers of 0.25 mm circular aperture each, placed with an inter-fiber center to center spacing of 0.375 mm with all fibers being contained within a circle of 4 mm diameter. In the case of the brush optodes, only a certain percentage of the brush fibers was blocked by hair while the rest had good optical contact with the scalp. Examples of a single brush fiber that is blocked and of one that is not blocked by hair are shown in Fig. 3-3(b) as the short and the long blue cylinders, respectively. The percentage of obstructed fibers assumed in the brush optode simulations as a function of hair density were measured experimentally (see Subject Measurements section) and are reported below (Table 3-1, Column 2). MC simulations were performed for hair densities spanning the range of measured values (0, 1.8, 2.2, and 2.8 hairs/mm^2).

Several simplifying assumptions were made to make these MC simulations more tractable:

(1) To increase the photon scoring efficiency at the optodes, the source of light, mimicking the light exiting the skull, at the bottom of the 4 mm thick block of scalp tissue containing the hair roots, was shrunk from the entire bottom area (10 mm x 10 mm surface) to a 3 mm diameter source. This was done after simulating the detected photon fraction for successively smaller source diameters while verifying that the detected photon fraction remained statistically unchanged.

(2) Since this MC simulation did not track photons throughout the entire head volume, any contributions of photons coming from the sides of the modeled tissue volume were not taken into account. More specifically, the bottom and sides of the scalp tissue block were made completely absorbing, which precluded contributions to the scored photon count from photons exiting and reentering this tissue volume. However, the sides of the tissue block were several mean free paths away from both source and detector and the probability of a photon reentering the tissue volume and hitting the detector was small. This assumption was verified by running the same simulations with reflective boundaries, as opposed to completely absorbing ones, and the scored photon counts remained statistically unchanged.

(3) Since the subjects in this study had fair skin complexion, it was assumed that all of them had the same skin absorption and scattering properties. Thus, the optical properties used for the scalp tissue block for all simulations were assumed as $n = 1.53$, $\mu_a = 0.06 \text{ mm}^{-1}$, $\mu'_s = 1.0 \text{ mm}^{-1}$, and $g = 0.9$ (to fit a Henyey-Greenstein model of scattering) (147).

(4) The scalp tissue block included evenly spaced hair follicles which were modeled as 0.1 mm diameter rods vertically extending from the air-tissue interface to 4 mm deep into the scalp tissue (148). The number of hair follicles varied for each simulation depending on the hair density (hairs/mm²) being simulated.

(5) In the simulations the hairs were arranged parallel to each other for layers laying on top of the scalp and were perpendicular when inside the scalp. This distribution of hairs [Fig. 3-3(b), brown rods] was an approximation for the fact that hair sprouted vertically out of the scalp and then bended sideways so that hairs were running parallel to it. The hairs were modeled as 0.1 mm diameter rods (132) with lengths of 20 mm, representing the average hair length of a person with short hair.

(6) The average number of hair layers measured for subjects with short hair (Table 3-1, Column 4) were modeled in each simulation such that each layer was parallel to one another while staggered in the XY plane. Each layer was assigned 3 hairs/mm to 7 hairs/mm, depending on hair density (Table 3-1, Column 4), following the experimental estimates described in the Subject Measurements section. The model of a bald subject only included the hair roots within the scalp.

(7) Hair colors including blonde, brown, and black were modeled with similar scattering properties ($\mu'_s = 0.023 \text{ mm}^{-1}$), yet different absorption properties ($\mu_a = 0.01, 0.98, \text{ and } 5.82 \text{ mm}^{-1}$ respectively) based on values reported in the literature for both the hair follicles and hair layers (149). The bald subjects in this study originally had black hair and thus the MC simulations modeled bald subjects having hair follicles with the absorption properties of black hair.

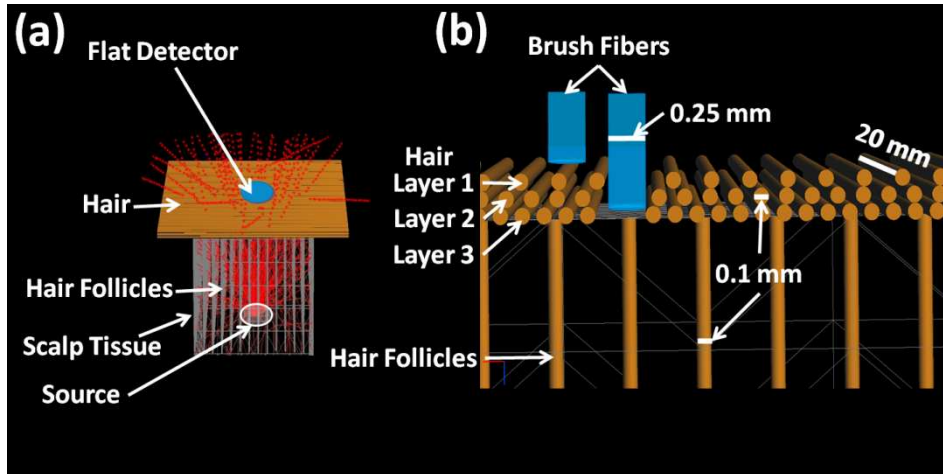


Figure 3-3 Schematics of (a) the overall MC simulation setup, and (b) a zoomed-in view of the hair layers, hair follicles, and the placement of a couple of brush fibers among the 64 brush fibers used in the simulations. In (a), the red solid lines are the simulated rays inside the scalp tissue ($10 \times 10 \times 4 \text{ mm}^3$), becoming red dashed lines once they left the scalp tissue. In (b), the short light blue cylinder indicates a brush fiber blocked by hair, and the long light blue cylinder a brush fiber that had good optical contact with the scalp.

3.2.3 Analytical Model of Photon Transport through Hair and Scalp Tissue

The attenuation that NIR light experienced due to scalp tissue and hair was also estimated analytically for subjects with short hair both for brush fiber and flat-faced optodes.

For the brush fiber optodes the analytical equation estimating the fraction of NIR light reaching a detector fiber after exiting the scalp (R_d , Eq. 3-4) considered the detected reflectance of NIR light for both obstructed and unobstructed fibers, the absorption of NIR light through the hair layers on top of the scalp, the fraction of brush fibers obstructed by hair, and the light collection efficiency of an obstructed fiber:

$$R_d = (1 - OF) \times R_{T,NObs} + OF \times D_{Eff} \times R_{T,Obs} \times \exp(-\mu_{a^*,H} \times z) \quad (3-4)$$

The first term on the right hand side of Eq. 3-4 estimated the detected reflectance from the fraction of fibers which had good optical contact with the scalp, whereas the second term estimated the detected reflectance for the fraction of fibers obstructed by hair. The summation of these two terms resulted in the fraction of light traveling through the scalp that reaches the detector, R_d . If the fraction of brush fibers obstructed by hair (OF) was equal to zero ($OF = 0$, e.g. a bald subject) then only the first term on the right hand side of the equation would remain. However, as $OF \rightarrow 1$, the second term became dominant. The OF was estimated from experimental measurements for each measured hair density (Subject Measurements section and Table 3-1). Additionally, in Eq. 3-4 $R_{T,NObs}$ is the reflectance of light at the scalp-air interface when an individual fiber had good optical contact with the scalp, $R_{T,Obs}$ is the detected reflectance when an individual fiber was obstructed by hair, $\mu_{a^*,H}$ is the volume-averaged absorption coefficient of the hair layers, z is the distance from the surface of the scalp to the obstructed fiber, and D_{Eff} is the reduction in geometric collection efficiency of the obstructed fiber in comparison to an unobstructed fiber.

Several simplifying assumptions were made when calculating R_d :

(1) The light reflecting at the scalp-air interface was treated as a plane wave and the potential gradient of the reflectance profile across the face of the detector optode was ignored to simplify the calculations. In comparison to how the MC simulations were performed (Fig. 3-3), the diffuse plane wave reaching a depth of one mean free path away from the scalp-air interface was considered as the source term. This source term was propagated through the scalp-air interface using the reflectance model given by Eq. 3-5, where R_T is the diffuse plane wave reflectance at this tissue-air interface, A is a proportionality constant (Eq. 3-6), $\mu_{tr} = (\mu_a + \mu'_s)$ is the transport coefficient, $a' = \mu'_s / \mu_{tr}$ is

the reduced albedo, and $\mu_{eff} = \sqrt{(3\mu_a\mu_{tr})}$ (150). As in this diffusion model the source term is non-directional, the original incoming direction of the plane wave, whether from the top of the scalp or from below the scalp, did not change the reflectance model used in Eq. 3-5:

$$R_T = \frac{3Aa'}{[(\frac{\mu_{eff}}{\mu_{tr}} + 1)(\frac{\mu_{eff}}{\mu_{tr}} + 3A)]} \quad (3-5)$$

$$A = \frac{1 - R_{eff}}{2(1 + R_{eff})} \quad (3-6)$$

(2) As shown in Eq. 3-6, the proportionality constant is dependent on the effective reflectance coefficient (R_{eff}). Therefore, the value of A differs between fibers with good optical contact with the scalp and those obstructed by hair. Given that light travelling through the scalp propagates mostly in the forward direction, as seen in Fig. 3-3(a), the simplifying assumption is made to ignore the spatial variability in refractive index matching conditions between scalp regions touched by a fiber and ones that are not. Instead, it assumed that the matched boundary condition applies for the diffuse planar wave solution shown in Eq. 3-5 when a fiber touches the scalp, whereas a scalp-air boundary condition applies for fibers obstructed by hair. A mismatch in the index of refraction (n) between the scalp tissue and air causes a change in R_{eff} (151). Typically, the index of refraction for tissue is $n = 1.4$ and R_{eff} for a tissue-air interface is 0.493 [39]. However, since this study is concerned with the attenuation due to scalp tissue, the index of refraction for the scalp ($n = 1.53$) [35] is used instead and the R_{eff} is recalculated to be 0.614 when a fiber is obstructed by hair (151). When an optical fiber has good contact with the scalp, there is no index of refraction mismatch due to the tissue-air interface and thus $R_{eff} = 0$ (151).

(3) Since the μ_a of hair follicles changed for different hair colors and the μ'_s of hair follicles was different from that of scalp tissue, it was necessary to calculate volume-averaged μ_a and μ'_s values for a 'homogenized' scalp tissue so that Eq. 3-5 could be evaluated. These effective μ_a and μ'_s values of the scalp tissue were calculated by Eq. 3-7 where $\mu_{\bullet, HF}$

$$\mu_{\bullet, HF} = VF_{HF} \times \mu_{\bullet, HF} + (1 - VF_{HF}) \times \mu_{\bullet, T} \quad (3-7)$$

represented the μ_a or μ'_s values (the dot subscript indicates either one) weighted by the volume fraction (VF_{HF}) of hair follicles (subscript HF) in the scalp (Table 3-1, Columns 5-8). Furthermore the volume fraction of hair follicles within scalp tissue was calculated by Eq. 3-8, where HD was the hair density, A_T the cross-sectional area of the scalp tissue, V_T the volume of the scalp tissue, and V_{HF} the volume of an individual hair follicle:

$$VF_{HF} = \frac{HD \times A_T \times V_{HF}}{V_T} = HD \times A_{HF} \quad (3-8)$$

Since the thickness of scalp tissue and the length of a hair follicle are assumed to be the same, this equation can be simplified so that VF_{HF} is found by the hair density and cross-sectional area of a hair follicle (A_{HF}). Moreover, μ_{eff} , μ_{tr} , and a' must be recalculated with $\mu_{a, HF}$ and $\mu'_{s, HF}$ before calculating $R_{T, NObs}$ and $R_{T, Obs}$.

(4) Similarly, the volume averaged μ_a and μ'_s of the hair layers surrounded by air would change due to hair color and hair density. In Eq. 3-9, $\mu_{\bullet, H}$ is the volume-averaged μ_a or μ'_s of the hair layers (Table 3-1, Columns 5-8), VF_H is the volume fraction of the hair layers between the scalp and the optode (Table 3-1, Column 3), and $\mu_{\bullet, H}$ is the μ_a or μ'_s of the hair.

$$\mu_{\bullet, H} = VF_H \times \mu_{\bullet, H} \quad (3-9)$$

$$VF_H = \frac{H_{mm} \times L \times A_H \times D_d}{L \times D_H \times D_d} = \frac{H_{mm} \times A_H}{D_H} \quad (3-10)$$

Furthermore, the volume fraction was calculated by Eq. 3-10 where H_{mm} is the number of hairs per millimeter in each layer (Table 3-1, Column 4), A_H is the cross-sectional area of a hair, and D_d is the diameter of a detector fiber. The cross-sectional area of a hair was found by $A_H = \pi(D_H/2)^2$ where $D_H = 0.1$ mm.

Table 3-1 The obstruction fraction (OF) of brush optodes, the volume fraction of the hair follicles in the scalp (VF_{HF}) and of the hair layers between the scalp and the detector fiber (VF_H), the linear hair density (H_{mm}) and number of hair layers (L), and the volume-averaged μ_a and μ'_s for the scalp and hair layers as a function of hair root density.

| | | | | Blond e | Brown | Black | |
|---|-----------------|---|--|---|---|---|---|
| Hair Root Density (hairs/m ²) | Brush OF | VF_{HF} / VF_H (no units) | H_{mm}/L (hairs/mm)/ (no units) | $\mu_{a,HF}/\mu_{a,H}$ (mm ⁻¹) | $\mu_{a,HF}/\mu_{a,H}$ (mm ⁻¹) | $\mu_{a,HF}/\mu_{a,H}$ (mm ⁻¹) | $\mu'_{s,HF}/\mu'_{s,H}$ (mm ⁻¹) |
| 0 (Bald) | 0 | 0.01 / 0.00 | 0/0 layers | 0.06 / --- | 0.07 / --- | 0.14 / --- | 0.986 / --- |
| 1.8 | 0.20 | 0.01 / 0.24 | 3/3 | 0.06 / 0.002 | 0.07 / 0.23 | 0.14 / 1.37 | 0.986 / 0.05 |
| 2.2 | 0.60 | 0.02 / 0.39 | 5/3 | 0.06 / 0.003 | 0.08 / 0.38 | 0.16 / 2.29 | 0.983 / 0.09 |
| 2.8 | 0.90 | 0.02 / 0.55 | 7/3 | 0.06 / 0.005 | 0.08 / 0.53 | 0.19 / 3.20 | 0.979 / 0.13 |

(5) Since $\mu'_{s,H}$ was small and little refraction of light was caused by the hair layers on top of the scalp, as was confirmed by MC simulations, the attenuation of light due to the hair layers was primarily due to light absorption. The light attenuation due to the hair layers was therefore expressed by the exponential term in Eq. 3-4, which follows the Beer-Lambert law. The z term in Eq. 3-4 can be expressed as $z = L \times D_H$, where the

number of hair layers, L , is seen in Table 3-1, Column 4, as a function of a subject's hair root density.

(6) The last simplification was that the geometric light collection efficiency of a brush optode was found by treating it as a group of 64 individual fibers cemented together acting as a single optode to collect the sum total of the detected intensity. Differences in the relative geometric light collection efficiency (D_{Eff}), when the optode was lifted upwards from the scalp surface by hair, were compared to the collection efficiency achieved when the optode touched the scalp surface ($OF = 0$) (152). The collection efficiency comparison for an optode was given by Eq. 3-11 where r was the radius of the optode, and z the distance of this optode from the surface of the scalp.

$$D_{Eff} = 1 - \frac{z}{\sqrt{z^2 + r^2}} \quad (3-11)$$

Given that the radius of a brush optode expanded to 2.0 mm when threaded through hair, D_{Eff} was equal to 0.950, 0.901, 0.852 for $z = 0.1, 0.2,$ and 0.3 mm, i.e. for $L = 1, 2$ and 3 hair layers respectively. As for a flat-faced optode with a radius of 1.5 mm, D_{Eff} was equal to 0.934, 0.868, 0.804 for $z = 0.1, 0.2,$ and 0.3 mm, respectively. On the other hand when the optode was not obstructed $D_{Eff} = 1$ ($z = 0$ mm).

Eq. 3-4 and all the considerations following it, as described above, were also used to calculate the percent power loss for the case of the flat-faced optodes. However, in contrast to the case of brush optodes where OF was measured experimentally (Table 3-1, Column 2), it was not easy to measure OF for the flat-faced optodes and an analytical estimation model was used instead:

The variation of OF for a flat-faced optode with hair density was determined by first finding the number of hairs remaining under the flat-faced optode after combing away as much hair as possible. The remaining number of hairs per millimeter after combing

(HR) had an approximate linear relationship with the hair root density (HRD): $HR = 10 \cdot HRD - 7$, with $HR = 0$ for $HRD < 0.7$ hairs/mm². Given that the maximum linear density per hair layer that could occur in adult subjects was $H_{max} = 7$ hairs/mm [23], the number of layers was estimated by rounding down to the nearest integer $L = \text{int}(HR / H_{max})$ and then the number of hairs per millimeter per layer remaining under the optode (HR_{mm}) was found by $HR_{mm} = HR / L$. Finally, the following three cases occurred for OF depending on the deduced number of hair layers:

(i) $L=0$: The flat-faced optode was not obstructed by hair and $OF = 0$.

(ii) $L=1$: The flat-faced optode was partially obstructed by a fraction equal to the hair-covered area divided by the total area of this fiber bundle optode of 3 mm diameter (D_d):

$$OF = \frac{HR_{mm} \times D_H}{\sqrt{\pi} (D_d / 2)} \quad (3-12)$$

(iii) $L > 1$: The flat-faced optode was completely obstructed by hair and $OF = 1$.

When substituting the calculated OF back in Eq. 3-4 the obstructed fraction was assigned an air-tissue boundary condition ($R_{eff} = 0.614$) and the non-obstructed fraction a matched boundary condition ($R_{eff} = 0$), as appropriate for cases (i)-(iii).

The calculated brush fiber and flat-faced optode R_d values (Eq. 3-4) for different hair colors and hair densities were compared against corresponding results from MC simulations and experimental measurements as described below.

3.3 Results and Discussion

3.3.1 Experimental Measurements

During placement of the flat optodes on the subjects' heads a large amount of time (35 – 45 min) was used in attempting to part hair so that each optode would have

proper optical contact with the scalp. Parting of the hair was difficult since there was limited space due to the dense probe geometry used in this work. However, the setup time was greatly reduced (10 – 15 min) when using the brush optode attachments, due to the brush optodes' ability to thread through hair. The threading through hair by the brush optodes also improved the optical contact with the scalp which resulted in increased SNR, CBR and dAoA for both ΔHbO and ΔHb (Fig. 3-4). Since the results of the ΔHbO and ΔHb signals and images were similar, further analysis is presented only for ΔHbO data. Different levels of statistical significance in Fig. 3-4 are represented by single ($p < 0.05$), double ($p < 0.005$), and triple ($p < 0.0005$) asterisks, respectively.

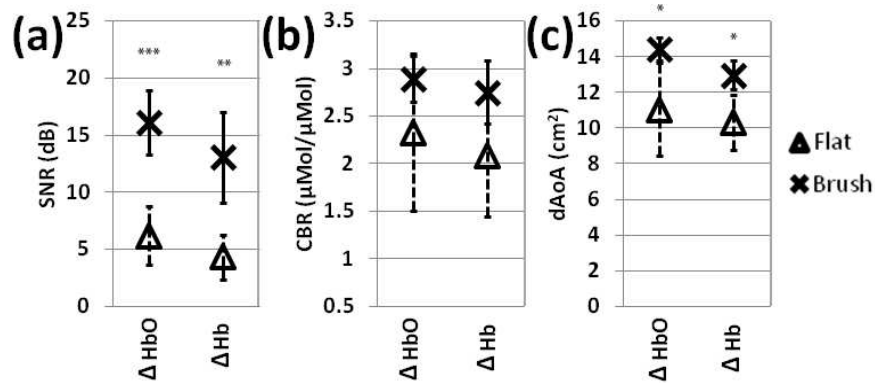


Figure 3-4 A comparison of ΔHbO and ΔHb (a) SNR, (b) CBR, and (c) dAoA between flat and brush optode sets. The single ($p < 0.05$), double ($p < 0.005$), and triple ($p < 0.0005$) asterisks identify the significance in activation metric mean difference between the flat and brush optode measurements.

With a detector-to-detector comparison [Fig. 3-5(a)], a clearer depiction of the improved activation SNR by the brush-fiber optode was seen. In Fig. 3-5(a) the vast majority of the brush-fiber optodes were shown to provide a larger activation SNR than the flat optodes. Moreover, the activation SNR improvement attained when using the

brush-fiber optodes was visible in the time-averaged ΔHbO plots of subjects spanning the entire range of hair densities – examples are shown for the lowest hair density (bald) [Fig. 3-5(b)] and highest hair density (2.8 hairs/mm^2) categories [Fig. 3-5(c)].

Comparing the ΔHbO activation images [Fig. 3-6(a)-(b)], there was a noticeable increase in the dAoA when using the brush optodes. The pixel values in the activation images were the values of the hemodynamic response amplitude determined by the GLM described in the Methods section. To be clear, an increase in dAoA does not mean that the physical activation area grew. Rather, the existence of more source-detector pairs with low activation SNR for the higher sensitivity brush optode measurements resulted in a larger apparent area of activation in reconstructed images due to the low spatial resolution of fNIRS. Additionally, the brush optodes had significantly ($p < 0.0005$) higher SNR when comparing areas in which both optode sets had detected activation [Fig. 3-6(c)]. It was also validated that the activation SNR improvement ($10.12 \pm 3.17 \text{ dB}$) was much larger than the activation SNR variability ($0.59 \pm 2.63 \text{ dB}$) between the two visits for each subject (difference signal = $-8.72 \pm 7.15 \text{ dB}$, $p = 0.0073$). Furthermore, low amplitude activation regions were detected with the brush optodes that were not detected with the flat optodes, due to poor optical contact [Fig. 3-6(d)]. Also, the success rate of effectively measuring a subject on both visits with the flat optodes amongst short haired subjects was 84.62% (11/13) and 25% (1/4) amongst long haired subjects whereas the brush optodes had a success rate of 100% (13/13) and 75% (3/4), respectively.

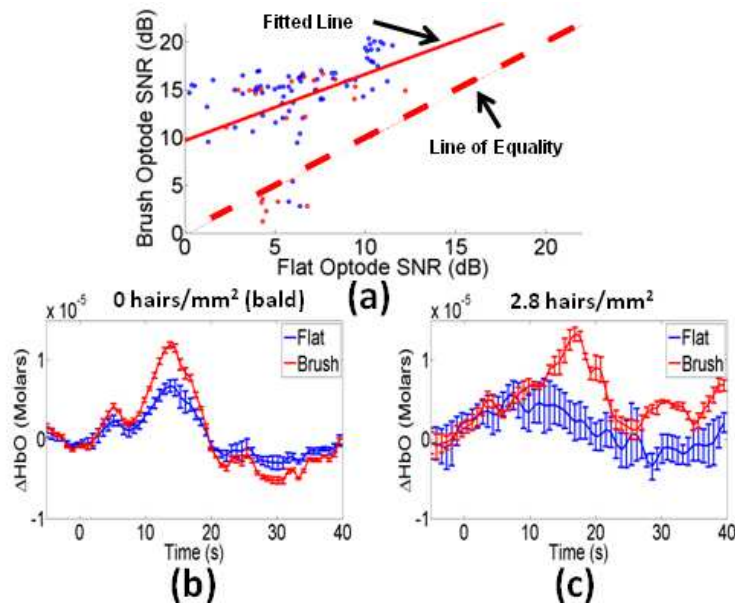


Figure 3-5 (a) A scatter plot comparing the activation SNR (dB) of the flat optodes (x-axis) versus that of the brush-fiber optodes (y-axis). The blue circles (short hair subjects) and red circles (long hair subjects) are SNR data points, the red-dashed line indicates the line of equality between the two SNRs, and the red-solid line shows a linear fit through the data. ΔHbO averaged time-plots are shown for (b) a bald subject (0 hairs/mm^2) and (c) a subject with 2.8 hairs/mm^2 .

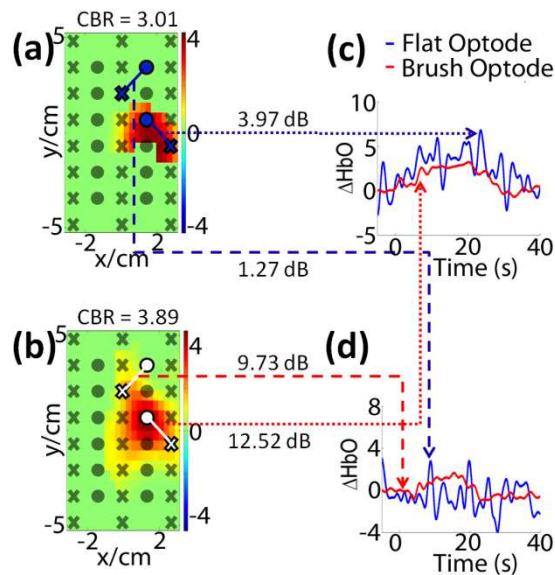


Figure 3-6 ΔHbO activation images (μMolar scale) for the same subject (black hair at a density of 2.2 hairs/mm^2) using (a) the flat optodes and (b) the brush optodes. The sources (grey filled circles) and detectors (grey filled Xs) are used to show the source and detector locations. (c) In regions where activation could be detected by both the flat and brush optodes, the latter resulted in significantly higher SNR (shown in dB). There were also locations where the flat optodes detected no significant activation where the brush optodes did (d).

Since darker hair absorbs more NIR light (149), it was hypothesized that the SNR would decrease with darker hair colors, due to the reduced number of photons reaching the detectors. Looking at individual subjects measured with similar hair lengths (20 – 23 mm, except for the bald subject) and hair densities ($\sim 2.8 \text{ hairs/mm}^2$) but different hair colors, the dAoA was smaller for subjects with darker hair colors for the flat optodes (Fig. 3-7) due to the decreased SNR [Fig. 3-8(a)]. Additionally, the brush optodes successfully detected activation from the subject with black hair whereas the flat optodes failed (Fig.

3-7). Head curvature also had an effect on the optical contact as demonstrated by the difference in dAoA (Fig. 3-7) and SNR [Fig. 3-8(a)] between the two optode sets for the bald subject. Due to the dense geometry used, the probe set had difficulty bending along the curvature of the head when using the flat optodes causing the flat optodes at the edges of the FOV to face at an angle to the scalp. Since the brush optode fibers bended and expanded at the brush end, they were able to keep good contact with the scalp along the curvature of the head.

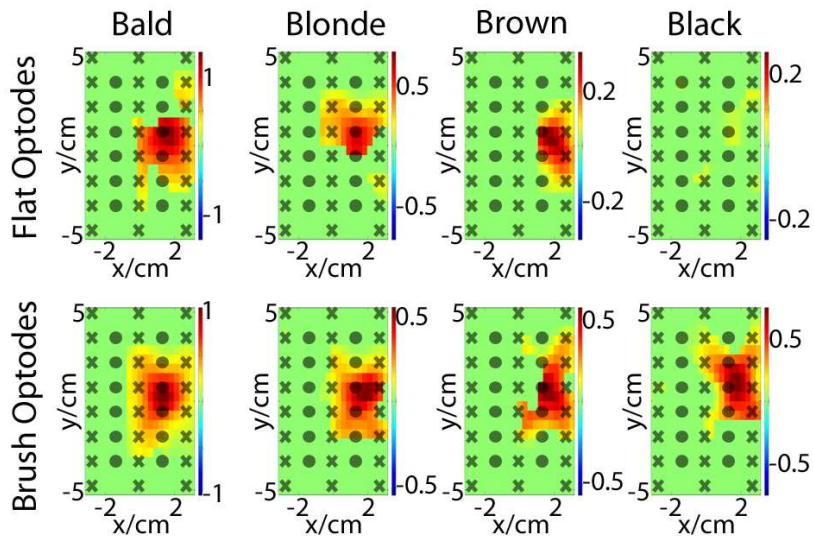


Figure 3-7 ΔHbO activation images, with color scales in μMolar , for four individual subjects with similar hair densities (~ 2.8 hairs/ mm^2) and hair lengths (20 – 23 mm), but different hair colors. Source positions are identified by the grey filled circles and the detector positions by the grey filled Xs.

An overall comparison of the SNR, CBR, and dAoA over different hair colors is presented in Fig. 3-8 separately for short haired [Fig. 3-8(a)-(c)] and long haired [Fig. 3-8(d)-(f)] subjects. Similar to Fig. 3-4, the statistical significance in Fig. 8 is presented by asterisks. As indicated in Fig. 3-8(a) there was a statistically significant ($p < 0.05$)

improvement in the SNR when using the brush optodes for all hair colors. Hair color did have an effect though, which was seen by the downward trend in SNR for darker hair for both sets of optodes. Despite the gains in SNR, the CBR only had small improvements ($p < 0.05$, statistical power $(1 - \beta) = 0.82$) for blonde and brown hair colored subjects [Fig. 3-8(b)]. The small changes in CBR can be explained by Eq. 3-3 which presents the CBR dependence on the mean activation amplitude and the standard deviation of the background pixel values in the activation images. In the case where many source-detector pairs had good SNR weak activation areas were detected. Inclusion of lower amplitudes in the numerator of Eq. 3-3 combined with no significant changes in the denominator resulted in lowering the overall CBR. On the other hand, in the case where more source-detector pairs had lower SNR, activation regions appeared more localized because lower activation amplitude pixels were lost in the hemodynamic background fluctuations. Therefore, the mean activation amplitude was higher in the numerator of Eq. 3-3, but the standard deviation of the background pixels was also higher, due to increased noise, in the denominator. In the end, due to this interplay between signal amplitude and background noise the CBR in images obtained from the brush or the flat-faced optodes was similar. Finally, the brush optodes had a greater dAoA than the flat-faced optodes for all short haired subjects [Fig. 3-8(c)], as was also discussed for a sample case in Fig. 3-6 above.

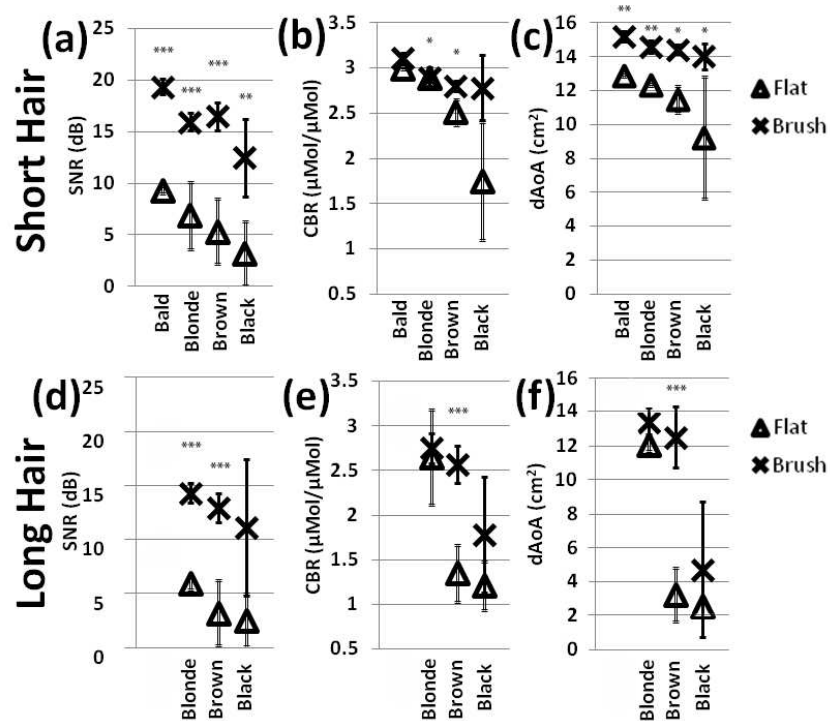


Figure 3-8 Scatter plots comparing the ΔHbO trend in (a) SNR, (b) CBR, and (c) dAoA for all short hair subjects ($n = 13$) for both the flat optodes (Δ) and brush optodes (X). Similar plots were made for long hair subjects ($n = 4$) (d)-(f). The single ($p < 0.05$), double ($p < 0.005$), and triple ($p < 0.0005$) asterisks identify the significance in activation metric mean difference between the flat and brush optode measurements.

As for the long haired subjects [Figs. 3-8(d)-(f)], the SNR at the detector level was found to be greatly improved for all hair colors [Fig. 3-8(d)]. However, the trends in CBR [Fig. 3-8(e)] and dAoA [Fig. 3-8(f)] were not as consistent for the long haired subjects, indicating greater improvements for the brown hair subjects at least. Nevertheless, this was only a result of a current shortcoming of the brush optodes used in this work and is not a fundamental limitation: It was observed that in the long haired subjects, the brush fibers could not reach the scalp because their length was too short to

thread through all the hair layers. In that detection geometry, the black hair would be more absorbing and therefore contribute to significantly higher signal attenuation, as was observed in the measurements. This problem could be alleviated in future work by constructing and using longer brush fiber optodes for the longer hair subjects so that the scalp can be reached more easily.

After examining the effect of hair color on fNIRS images, the effect of hair density on these images was also analyzed (Fig. 3-9). Images obtained using the brush and flat optodes were compared for individual subjects with black hair and similar hair lengths (20 – 23 mm, except for the bald subject), but different hair densities. As can be seen in Fig. 3-9, subjects with denser hair had less dAoA, which was explained by the statistically significant ($p < 0.05$) lower SNR [Fig. 3-10(a)] at higher hair densities. Typical images from individual subjects in each hair density category are presented in Fig. 3-9, whereas group average results are presented in Fig. 3-10. Long hair subjects were not compared across hair densities, since all these subjects had a similar hair density of ~ 2.8 hairs/mm². As was also observed when comparing results for different hair colors in Fig. 3-8 above, when plotting results as a function of hair density, one can see gains in SNR [Fig. 3-10(a)] and dAoA [Fig. 3-10(c)], but no significant gains in CBR [Fig. 3-10(b)]. Furthermore, when using the brush optodes, the dAoA values across all hair densities were similar to the values found for bald subjects [Fig. 3-10(c)].

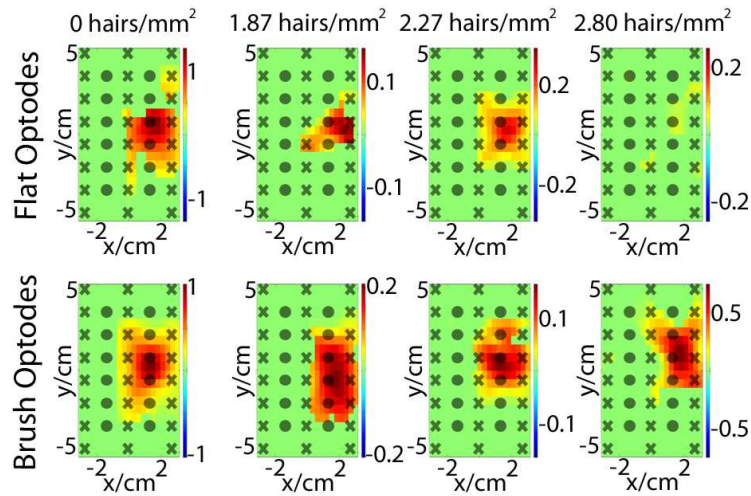


Figure 3-9 ΔHbO activation images (color scales in μMolar) for four individual subjects with similar hair color (black), but different hair densities for both flat and brush optode sets. Source positions are identified by the grey filled circles and the detector positions by the grey filled Xs.

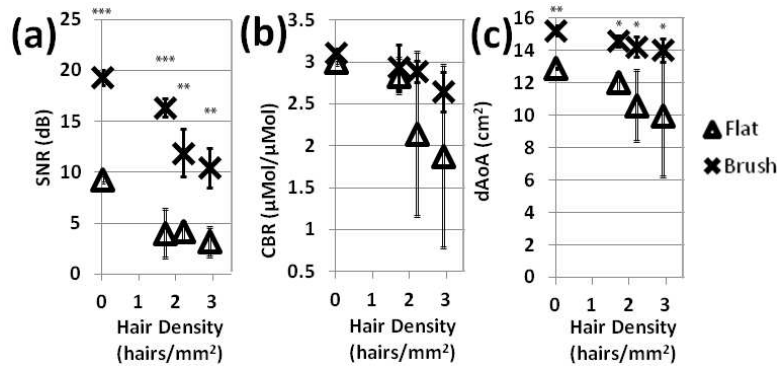


Figure 3-10 Scatter plot comparing the ΔHbO trend in (a) SNR, (b) CBR, and (c) $d\text{AoA}$ for short hair subjects of all hair colors ($n = 13$) for both the flat optodes (Δ) and brush optodes (X). The single ($p < 0.05$), double ($p < 0.005$), and triple ($p < 0.0005$) asterisks identify the significance in activation metric mean difference between the flat and brush optode measurements.

3.3.2 Comparison of fNIRS Signal Attenuation Measurements with Corresponding Monte Carlo Simulations and Analytic Model Estimates

MC simulations using the FRED software and an analytical formula (Eq. 3-4) were used to estimate the magnitude of fractional light power attenuation for different hair densities and hair colors for comparison against the human subject measurements. Not only did the MC results approximate the experimentally measured power losses well but, fascinatingly, the derived analytical model predictions were found to be within a few percent of both the MC simulation and experimental results, as shown in Fig. 3-11 below, despite many simplifying assumptions. In addition, the diffusion theory based calculation of NIR light transport through the scalp (Eq. 3-5) was compared against Kubelka-Munk theory (153, 154) and results were found to be very similar for all hair colors and densities (data not shown). This comparison indicated that the diffusion approximation was not violated even for subjects with dense dark hair, which was most likely due to the volume averaging of the high μ_a values of hair with the lower μ_a of the surrounding scalp in this 'homogenized' scalp tissue model. In this work a large number of long haired subjects were not recruited and thus a detailed comparison with the MC simulations and analytical formula was not performed for these subjects.

In Fig. 3-11 the experimental results for the percent power loss in a short haired subject with respect to a bald subject were compared to corresponding MC simulations and analytical model calculations for different hair colors. Since hair densities varied within each group of hair colors, the results displayed in Fig. 3-11 plot the percent power loss across the different hair densities encountered in this work (0 – 2.8 hairs/mm²) separately for each hair color. Though for the subject pool recruited in this work no non-bald subjects existed with low hair densities, an additional hair density of 1.0 hairs/mm²

was included into Fig. 3-11 for the MC data to estimate the trend between hair densities of 0 and 1.8 hairs/mm² for completeness. Also, additional hair densities were included between 0 – 2.8 hairs/mm² in the evaluation of the analytical model so as to produce smooth continuous curves. In these calculations the *OF* of the brush optodes for hair densities in-between the values listed in Table 1 were linearly interpolated from the experimental measurements for each hair density. Examining Fig. 3-11 across each row, it is apparent that darker hair colors caused an increase in the percent power loss. The percent power loss for the flat optodes had shallow slopes with increasing hair density that reflected the linear dependence of volume-averaged light absorption on the volume fraction of hair roots and hair (Eqs. 3-8 and 3-10). These power loss slopes as a function of hair density were steeper for the darker hair colors. On the other hand, in Fig. 3-11 it is apparent that the percent power loss was reduced when using the brush optodes for all hair colors though less so at the higher hair densities.

The slope of power loss in each graph comprising Fig. 3-11 had three stages as a function of hair density. In the first low hair density stage (approx. 0 – 1 hairs/mm²) the percent power loss slope was close to zero as both flat-faced and brush optodes had good optical contact with the scalp. Nevertheless, some power loss started becoming noticeable for the flat-faced optodes above 0.7 hairs/mm², as the optodes were partly lifted off the scalp by the hair below them. In contrast, the brush optodes kept good optical contact with the scalp because they could fit between the hairs. In the second stage of the graphs in Fig. 3-11 (approx. 1 – 2 hairs/mm²) there was a larger power loss slope. The brush optodes had a shallower slope than the flat-faced optodes, because some of the brush fibers always attained matched boundary conditions with the scalp. In contrast, the large jump in power percent loss seen in the second stage for the flat-faced optodes occurred because these were now almost completely lifted off the scalp by the

hair underneath them that could not be removed and R_{eff} changed from matched ($R_{\text{eff}} = 0$) to air-tissue boundary conditions ($R_{\text{eff}} = 0.614$). In the third stage (approx. 2 – 3 hairs/mm²) the slope of the graphs changed again. In this stage, the flat-faced fibers were completely lifted off the scalp and increasing the hair density only increased the Beer-Lambert attenuation (Eq. 3-4, second term). In contrast, the brush fibers had a larger percent power loss slope in this third stage. This occurred because the space between brush fibers was now getting filled by hair and a bigger fraction of brush fibers was being lifted off the scalp by the hair accumulating underneath them as the hair root density increased. If the brush fibers used in this work were longer in length, more hair could stack in-between them, rather than below them, and therefore the transition from stage two to stage three could be pushed to even higher hair densities.

By re-plotting Fig. 3-11 so that the comparisons of the percent power loss were made for different hair density categories as a function of hair color (graphs not shown), an increase in percent power loss with increasing hair density was found for all hair colors. However, in contrast to Fig. 3-11 where power losses had shallow slopes with linearly increasing hair density, the power loss increased sharply with darker hair color for both the flat-faced optodes and the brush fibers. These sharper slopes were primarily due to the exponential Beer-Lambert law of attenuation experienced by light traveling through the hair layers (Eq. 3-4). It should also be noted that although the recruited bald subjects only had a low hair root density and black hair roots, they were used as the reference for all plots in Fig. 3-11 and all other analyses. This was because finding bald subjects with different hair root colors and densities or no hair roots at all, to thus provide ideal comparison standards, was not practical.

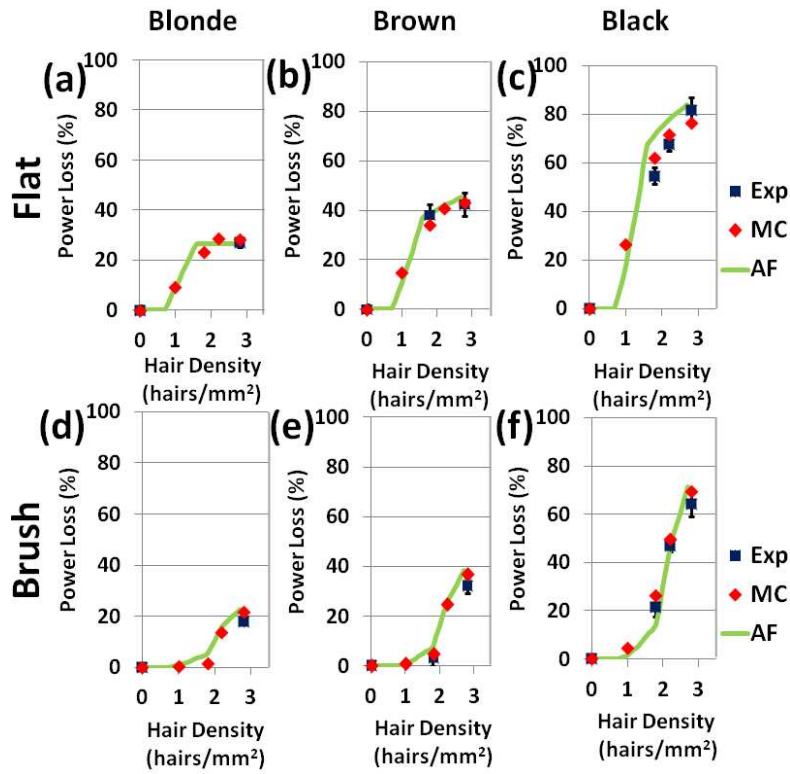


Figure 3-11 The percent power loss with respect to bald subjects when using either the flat or the brush optodes. Comparison of the experimental (Exp), MC simulated (MC), and analytical formula (AF) results is performed across hair densities for each hair color.

Although significant signal gains were attained by using the brush optodes in most cases, Fig. 3-11 also indicates that subjects with the highest hair density only had slightly lower percent power losses compared to the corresponding flat optode measurements. By consulting the optode obstruction fraction as a function of hair density (Table 3-1, Column 2) one can see that obstruction of brush fibers is 90% at the highest hair density. Therefore in that case most fibers were lifted up from the scalp by hair and the collection geometry was similar to that of the flat optode. Interestingly, even though percent power losses were similar between brush optodes and flat optodes for the

highest hair density category, Fig. 3-10(a) indicates that there were nevertheless significant gains in SNR for that category. The observation that even bald subjects had an SNR gain [Fig. 3-10(a)] because the brush optodes adapted better to the head curvature, and evaluation of Eq. 3-4, provided the insight that these gains originated from the matched boundary condition attained by the brush fibers that maintained good optical contact with the scalp. The improved optical contact enhanced the sensitivity to detect light coming from the cortical regions. Taken together, the above findings suggest that brush optodes could create useful images at hair densities where the flat optodes could not (Fig. 3-9) because even if only 10% of the fibers in a brush optode could attain good optical contact with the scalp, these fibers could still glean enough signal to help form fNIRS images.

3.4 Conclusions

A novel brush fiber attachment to the flat-faced detector optodes of a commercially available fNIRS system was developed to improve optical contact with the scalp. The performance of this optode during fNIRS measurements was tested on 17 subjects with varying hair colors and hair densities performing a finger tapping protocol with and without the brush optode attachments. The most salient finding of this work was that, in comparison to the flat optodes, the brush optode attachments improved the SNR by up to a factor of ten [Figs. 3-8(a), 3-8(c), and 3-10(a)] making it possible for subjects with dark hair and high hair densities to be consistently measured successfully with fNIRS, which was not possible before. The increase in activation SNR by the brush optodes also led to a significant increase in dAoA ($p < 0.05$) for both ΔHbO and ΔHb data [Figs. 3-4 and 3-10(c)].

The source-detector arrangement was dense making it difficult to part hair, thus increasing the setup time when using the standard flat optodes (35-45 min.). This setup time was reduced by at least a factor of three (10 – 15 min.) when using the brush optodes due to their ability to readily thread through hair. In addition to the significant gains in setup time the improved optical contact with the scalp that the brush fibers enabled resulted in increasing the fNIRS study success rate to 100% (13/13) for the short hair subjects and to 3/4 from 1/4 for the long hair subjects. Also, the individual fibers of the brush-fiber optodes proved sturdy enough to undergo the pressure applied to achieve good optical contact for 34 sets of measurements and are still being used in current studies.

The improvement in fNIRS measurements was validated by MC simulations of the light intensity attenuation for subjects with different hair densities and hair colors. The comparison against the simulations showed very good agreement with the experimental data. Furthermore, an analytical model was derived from first principles to estimate the light power attenuation by the scalp and hair. Despite several simplifying assumptions, excellent agreement was attained between the analytical formula predictions and corresponding fNIRS measurements and MC simulations (Fig. 3-11). The derived analytical formula can therefore be a very useful tool, enabling researchers to estimate readily the power attenuation loss factor due to scalp and hair for a given subject and optode type.

It is noteworthy that the single long-haired subject that could not be measured with the brush optodes could have possibly been measured too if the brushes were longer. For future studies, it is therefore advisable that a longer brush fiber set is also constructed to make it possible to thread through the thicker hair layers found in long hair subjects. Also, the SNR of human subject measurements could be further improved if the

~2.5 dB loss due to imperfect optical contact between the brush-fiber attachments and the commercial fNIRS system's fiber bundles [23] could be reduced by an improved optical coupling design. Despite current limitations the brush optodes present a technological leap towards improved NIR light collection.

Importantly, the brush fiber optode attachments can be molded to fit the diameter of any flat fiber bundle in current commercial fNIRS systems and can thus be very useful for enhancing the success rates and reproducibility of fNIRS studies.

Chapter 4

FNIRS Maps Cortical Plasticity Underlying Altered Motor Performance Induced by tDCS

4.1 Introduction

Augmentation of rehabilitation with concurrent cortical stimulation is a valuable approach for facilitating plasticity in the injured human brain to improve physical performance. This method may be especially beneficial to patients following stroke, as persistent deficits in the affected limb lessen the quality of life (155). Stimulation of the cortex with transcranial magnetic stimulation (TMS), transcranial direct current stimulation (tDCS), and epidural cortical stimulation (ECS), results in beneficial neuroplasticity by modulating the excitability of the underlying neural circuitry. Contingent on the cortical location, stimulation can lead to improvements in speech (89), motor control (31, 64, 156-160), pain (161), depression (162), neglect (163), and the reduction of sensory deficit^(164, 165) in patients with various brain disorders.

Recently, tDCS has attracted increased interest due to its sustained effects, which last up to a week (166) and have beneficial therapeutic outcomes for stroke patients (31, 50, 160-163). TDCS is a non-invasive cortical stimulation technique which modulates the cortical activity with intensities below the motor threshold (167). Depending on the current polarity, tDCS can either excite or suppress the underlying cortical regions (168, 169) similar to TMS, though with less topographical specificity than TMS. However, advantages of using tDCS over TMS include the ability to stimulate during a motor task even if it involves head or torso movements, low cost, and excellent tolerability. Previous studies (170, 171) show that tDCS stimulation during an activity modulates the neural circuitry specific to that task, which potentially gives tDCS the ability to have task-specific effects and thus direct neuroplasticity in the desired direction of a physical therapy regimen.

TDCS applied bi-hemispherically, such that one hemisphere is suppressed (cathode) and the other hemisphere is excited (anode) concurrently (71), can simultaneously suppress the unaffected (i.e. healthy) hemisphere and excite the affected (i.e. injured) hemisphere of stroke patients to improve motor performance by normalizing laterality of cortical activity (90). Furthermore, bi-hemispheric tDCS applied on healthy adults resulted in a larger increase in motor improvement compared to when the same hemisphere underwent only unilateral anodal tDCS (34). However, to our knowledge studies have only applied bi-hemispheric tDCS in one current direction, and have not yet compared the cortical or performance effects of bi-hemispheric tDCS when the anode is placed over the hemisphere ipsilateral to the affected limb.

In order to better understand the effects of tDCS on the plasticity of the human cortex, neuroimaging techniques have been recently combined with this stimulation method. Functional magnetic resonance imaging (fMRI) after tDCS showed neuroplastic resting-state connectivity changes in the sensorimotor cortical regions (162-165). Additionally, changes in resting-state cortical regional cerebral blood flow were measured after tDCS by positron emission tomography (PET) (165), but only a few studies have explored the effects of tDCS during cortical activation (166, 172, 173). One study used fMRI to detect changes in cortical activation hemodynamics in the supplementary motor area (SMA) during anodal tDCS while the subjects performed a finger tapping task (172), but electric current flow confounds concurrent fMRI eco-planar imaging during tDCS (174). Therefore, a technique that is independent of magnetic field measurements is desirable, particularly as continual non-invasive neuroimaging of tDCS-induced plasticity could yield great potential for improving the understanding of functional plasticity and for guiding therapeutic applications.

One such portable and low cost neuroimaging modality is functional near-infrared spectroscopy (fNIRS), previously used to study brain function in healthy subjects (99, 100, 102, 122, 134, 175) and individuals affected by a wide range of central nervous system pathologies such as stroke, depression, cerebral palsy, and Alzheimer's disease (124, 176). Though this optical technology is limited to cortical imaging at a modest spatial resolution, it can potentially offer high activation-related signal detection sensitivity, high temporal resolution, and relative robustness to motion artifacts (123, 129). fNIRS detects changes in light absorption and scattering in tissue caused by fluctuations in oxy-hemoglobin (HbO) and deoxyhemoglobin (Hb) concentrations secondary to neuronal activity, known as neurovascular coupling (130, 177). It has also been shown that fNIRS is able to detect event-related optical signals (EROS), which occur within hundreds of milliseconds and correlate with evoked potentials measured by simultaneous electroencephalography (EEG) (66, 128) are much faster than the seconds resolution of fMRI (117, 120). Recently, fNIRS detected changes in resting state HbO after anodal tDCS was applied to the prefrontal cortex (69), though no fNIRS studies to date have explored the effects of tDCS on functional activation patterns in the sensorimotor cortex, which is the focus of this work.

In this study, the hemodynamics in sensorimotor cortical regions were measured using fNIRS before, during, and after bi-hemispheric tDCS was applied to the sensorimotor cortex of eight healthy adults. The use of fNIRS enabled quantification of changes in both resting-state connectivity and functional activity of cortical regions activated during a wrist flexion task, during and after tDCS. The isometric wrist flexion task was performed while subjects held a lever outfitted with sensors to measure the torque, allowing quantification of the speed and accuracy of task performance in relation to cortical activity. Moreover, during this event-related protocol, changes in the activity of

the forearm and upper arm muscles, measured by surface electromyography (sEMG) concurrent with fNIRS, yielded complementary information on how the activation of specific muscles related to changes in cortical activation patterns elicited by wrist flexion. The results of this work indicate how the novel combined use of tDCS, fNIRS, sEMG and task performance measurements can offer insights into how cortical plasticity influences task performance during and after intervention with tDCS. These methods could be used in future studies to guide the patient-specific rehabilitation of hemiparetic patients during tDCS-enhanced physical therapy.

4.2 Materials and Methods

4.2.1 Subjects

Nine right handed subjects were included in this study. Subject handedness was determined by the Edinburgh Handedness Inventory (178). All subjects were healthy and did not have a history of neurological disorders other than headaches. A side effect that occurs during the ramp up and down of current for tDCS in a small percentage of human subjects is the visual perception of flashing lights (179). One subject did not return due to flashing lights seen in the first tDCS session during the ramp up of current and this subject's data was not included in the analysis. Data analysis was performed on the remaining eight subjects (2 female and 6 male; 33 ± 8 years old). The studies were performed under the approval of the University of Texas at Arlington Institutional Review Board protocol (IRB No.: 2012-0356).

4.2.2 Imaging with fNIRS and tDCS Setup

A continuous wave fNIRS brain imager (CW-6, Techen Inc., Milford, Massachusetts) was used to map the HbO changes induced by sensorimotor cortex

activity before, during, and after bi-hemispheric tDCS. The fNIRS source-detector geometry is shown in Fig. 4-1(a). Sixteen detectors [Fig. 4-1(a), light blue X's] were placed over each hemisphere to cover a relatively large area of the sensorimotor cortex. The rows of sources [Fig. 4-1(a), dark blue circles] and detectors were centered around the C_z position of the EEG International 10/20 system (180) and attached onto the subjects' heads by perforated Velcro straps. Sixteen laser sources emitted at 690 nm and sixteen at 830 nm, such that each optical fiber bundle delivered light of both wavelengths at each source location simultaneously. Each source bundle had up to six detectors within a 3 cm distance and each detector received signals from up to three source bundles. Additionally, 8 short (1.5 cm) source-detector separations measured the hemodynamic fluctuations in the scalp to adaptively filter the global background hemodynamics unrelated to the activation-related hemodynamic response (details in Section 4.2.5 below). As a result, there were 84 possible source-detector channel combinations for each wavelength. All source-detector pairs simultaneously monitored activation in cortical areas within the probes' field of view (11 cm × 20 cm), as the CW-6 system enables all laser sources to be on at the same time with distinct modulation frequencies (6.4 - 12.6 kHz, with an increment of 200 Hz). Back-reflected light was sampled at a rate of 25 Hz.

The approximate anterior-posterior functional-anatomical location of the premotor cortex (PMC), SMA, primary motor (M1), and primary sensory (S1) cortical regions in each subject were determined by comparing previously reported MRI and fMRI studies activation locations (181, 182) with fNIRS results from the eight subjects in this study obtained during left hand sensory stimulation, finger tapping, and sequential finger tapping protocols (Section 4.2.4). These protocols were the same as those used in Appendix A. These measurements were performed once on a separate fNIRS session.

Additionally, the EEG International 10/20 system (180) C_z, C₃, and C₄ anatomical measurements made at each fNIRS session were sufficient for locating the major sensorimotor cortex areas for each subject in subsequent tDCS sessions. The error in the probe and electrode placement was estimated by the variation of the measured C_z, C₃, and C₄ positions at the three fNIRS measurement sessions which did not exceed ~3 mm. In comparison to vibrotactile stimulation of individual fingers, which results in unilateral activation of the contralateral (right) hemisphere (181), sensory stimulation of multiple fingers resulted in bilateral S1 activity [Fig. 4-1(b)] as was found in a previous study (183). Also, in agreement with prior studies, finger tapping elicited activation in the contralateral (right) hemisphere PMC, M1 and S1 cortical regions [Fig. 4-1(c)] (100), and sequential finger tapping activated the contralateral hemisphere M1 and S1, and bilateral PMC cortical regions [Fig. 4-1(d)] (182).

After the placement of fNIRS optodes was completed, tDCS current was applied by a battery-driven electrical stimulator (Phoresor II, IOMED Inc., Salt Lake City, Utah) connected by a pair of saline-soaked gauze covered gel electrodes (5 x 5 cm; IOMED Inc., Salt Lake City, Utah) centered over the C₃ and C₄ positions according to the EEG International 10/20 system [dashed boxes in Fig. 4-1] that cover the bilateral M1 (184). In order to accommodate the placement of fNIRS sources and detectors within the area covered by the tDCS electrodes, two 0.5 cm diameter holes (standard hole punch size) were made on opposing sides of each electrode so that the optical fiber bundles could fit through them.

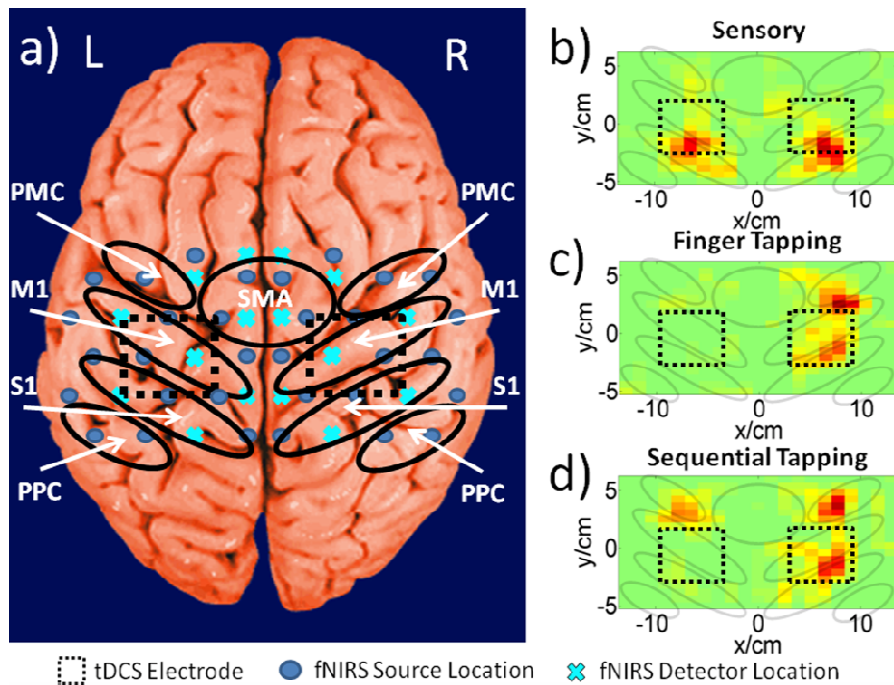


Figure 4-1 (a) This image shows the fNIRS sources (dark blue filled circles), detectors (light blue filled X's), and the tDCS electrodes overlaid (dashed squares) on a model brain. The ellipses identify different sensorimotor cortical regions on both the ipsilateral or left (L) and contralateral or right (R) hemispheres over which fNIRS and tDCS take place, such as the supplementary motor area (SMA), premotor cortex (PMC), primary motor cortex (M1), primary sensory cortex (S1), and posterior parietal cortex (PPC). To confirm the approximate locations of these cortical areas without performing fMRI, fNIRS image group analysis was performed for the eight subjects undergoing sensory stimulation of the left hand (b), and performing left hand finger tapping (c), and left hand sequential tapping (d). Here and throughout the paper, right hemisphere is displayed on the right, left hemisphere on the left as if looking down at the head.

4.2.3 sEMG and Torque Measurement Setup

Isometric contractions of the forearm and upper arm muscles were measured by sEMG (Brain Vision LLC, Morrisville, North Carolina). After abrading and cleaning the skin, a ground electrode was positioned on the left lateral epicondyle and bipolar surface electrodes with a center-to-center inter-electrode distance of 4 cm on both arms of the subjects over the wrist flexor (WF, flexor carpi radialis muscle), wrist extensor (WE, extensor carpi radialis muscle), biceps brachii, and triceps brachii muscles of both arms, measuring the muscle activity at a sampling rate of 500 Hz (Fig. 4-2).

A custom hand device (JR3 Inc., 35-E15A, Woodland, CA) measured the isometric moments exerted by test subjects on a static Delrin® handle (Fig. 2) (63). Forces and moments exerted during fNIRS were monitored in real-time, were continuous in nature, and scaled linearly with exertion level. The torque measurements were first low-pass filtered at 50 Hz before being sampled at 1000 Hz. Six padded adjustable bumpers stabilized the forearm during testing, adjusted to accommodate forearms, and guaranteed consistent positioning of the forearm. The hand device, connected to both the protocol display laptop and sEMG box, received the stimulus time points from the laptop, and sent a trigger (T in Fig. 4-2) to the sEMG box allowing the hand device and sEMG signals to be measured on a common time base.

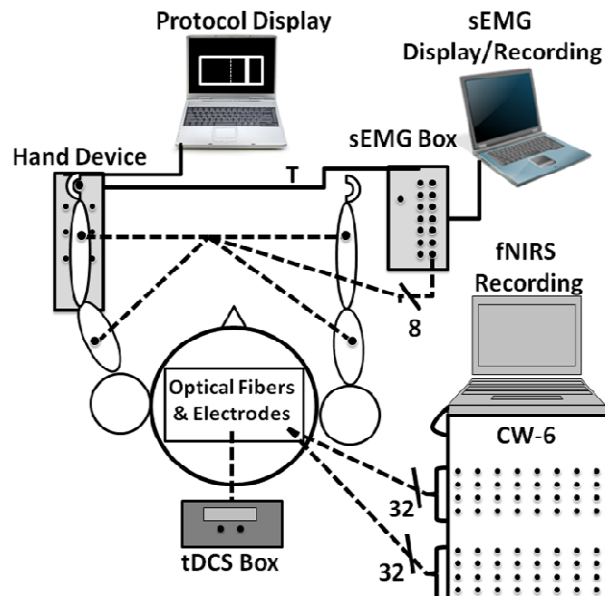


Figure 4-2 This figure is a cartoon representation of the overall instrumentation setup. The protocol display showed the presentation the subjects were to follow, and recorded the torque measurements from the hand device. A trigger (T) was sent from the hand device to the sEMG box which identified the beginning of the task stimulus separately in both data sets. There are 8 sEMG measurements detecting the muscle activity of both arms (dashed lines from arms to sEMG box). Additionally, the box over the person's head represents the placement of optical fiber bundles and tDCS electrodes described in Section 4.2.2. Like the force and sEMG measurements, the 32 x 32 channel fNIRS data was recorded on a separate laptop.

4.2.4 Protocol

Each subject was comfortably seated up-right after instrumentation setup. During the entire experimental session the room was quiet and subjects were asked to avoid extra movements. Before measurements, each subject performed isometric wrist flexion task with maximum effort using their non-dominant (left for all subjects) hand three times.

The non-dominant arm is used in this study since a prior tDCS study found no significant changes in hand performance in the dominant hand, but significant improvement in the non-dominant hand after anodal tDCS (185). The torque measurements were normalized to the subject's mean maximum isometric wrist flexion contraction force, and expressed as a percentage of maximum torque to standardize strength and function effort across subjects. The computer interface guiding subjects (Fig. 4-2) was user-friendly, consisting of a target that was centered at 50% of the subject's maximum torque, with a target width of 2.5% of the maximum torque, and a cursor which responded to isometric wrist torques. Previous use of this hand device found that the 2.5% target width produced detectable changes in subject performance during tDCS (63). The goal of the subject was to move the cursor into the target and hold it there for 1 s. The protocol presentation on the computer interface started with 10 s of rest, followed by nine sets of the isometric wrist flexion task, and ended with 10 s of rest. The nine sets of the isometric wrist flexion task were set at 50% of the maximum torque. The inter-stimulus interval varied randomly between 16 - 40 s, allowing enough rest time for cortical hemodynamics to return to baseline. In total, the protocol presentation for each condition lasted 5 minutes and 8 s.

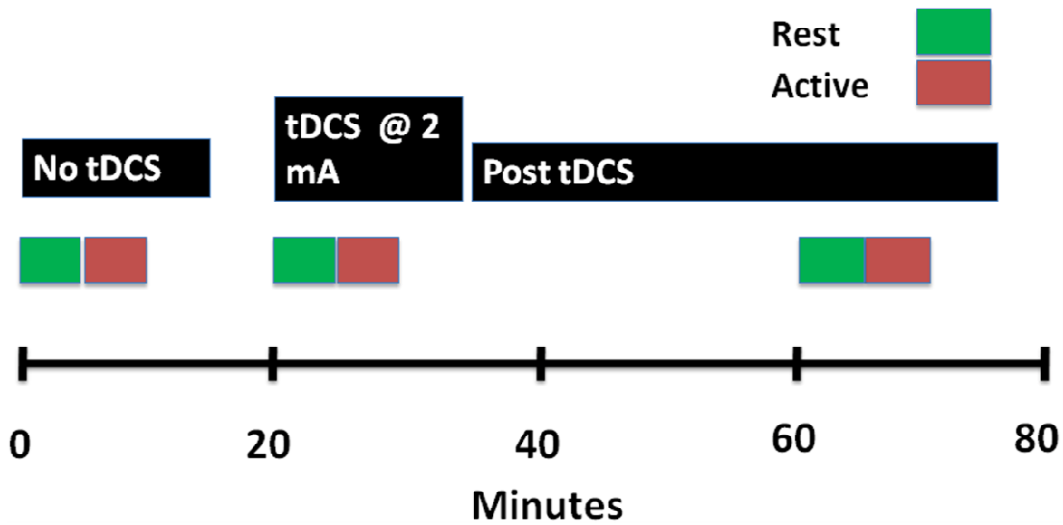


Figure 4-3 The protocol timeline: green boxes indicate rest periods, red boxes indicate wrist-flexion task periods, and the black boxes indicate the time periods before, during, and after tDCS.

For each visit, the measurements were split into three separate blocks: before, during, and after tDCS (black boxes in Fig. 4-3). Within each block there were two separate conditions. The first condition within each block was a rest condition (green boxes in Fig. 4-4), where each subject sat still throughout the presentation while tracking the visual target. The second condition of each block had the subject perform a set of isometric wrist flexion tasks (red boxes in Fig. 4-4). In the second block, tDCS (constant current of 2 mA, 15 minutes) current was ramped up and down gradually over 30 seconds to minimize sensory and visual effects at the beginning and end of stimulation. In the rest condition measurement during tDCS (second block, first measurement), current was not applied until after two minutes into the presentation. This permitted us to measure changes in the hemodynamics, in real time and to our knowledge for the first time, during the ramp-up phase of tDCS. In between the second and third blocks of

measurements, subjects rested for 25 minutes to avoid fatigue and study the aftereffects of tDCS on cortical hemodynamics. After every block of measurements, subjects were asked about their pain on a scale between 0-10, and about their fatigue, perceived task effort and perceived task complexity⁶⁶ on a Likert-type scale of 1-7 (186, 187) using visual analog scales. In between measurement blocks the scores in pain, fatigue, perceived effort and complexity did not significantly increase (≤ 2 points). Thus any cortical hemodynamic changes were mainly due to either the applied tDCS or the isometric wrist flexion task, and not due to pain, fatigue, or task difficulty. Subjects performed the sessions of anode to ipsilateral (left) M1 and cathode to contralateral (right) M1 (presumed inhibitory montage), and cathode to ipsilateral (left) M1 and anode to contralateral (right) M1 (presumed excitatory montage), at least one week apart in random order. The polarity of the stimulation was not known to the subjects, however the investigator was not blinded to the assignment. The minimum one-week interval permitted enough time between tDCS visits for the hemodynamics to return to their original baseline (53).

4.2.5 fNIRS Signal Filtering and Image Analysis

In addition to detecting evoked hemodynamic changes, fNIRS is sensitive to cerebral hemodynamic fluctuations of systemic origin caused by cardiac pulsation, respiration, and Mayer waves (96, 135). This study used a combination of band-pass filtering, adaptive filtering, and component analysis to filter the fNIRS signals as we have previously done (188). Because Hb dynamics are highly correlated with those of HbO (189) but with lower amplitudes and are susceptible to cross-talk from HbO (101) and interference from physiological artifacts, we have focused on the analysis of HbO dynamics only. After each resting measurement, the changes in HbO for the succeeding

activation measurements were determined in reference to a baseline value which was taken to be the average from the last minute of the preceding resting-state measurement. In the case of the activation measurements during tDCS, the last minute of the resting-state measurement was steady at a new baseline level. Thus, HbO changes due to isometric wrist flexion task during and after tDCS were in reference to the new baseline levels instead of the levels found before tDCS.

Reconstruction and visualization of fNIRS activation images resulting from the acquired reflectance data was performed by the open-source HomER software implemented in MATLAB (141) by use of the Tikhonov perturbation solution to the photon diffusion equation, which employs a regularized Moore-Penrose inversion scheme (142, 143). The reconstructed, two-dimensional images (21 x 21 pixels) for every 0.04 s time interval represented maps of changes in HbO on the cortical surface, within the detector's field of view (Fig. 4-1). Regions of activation were determined by a general linear model (GLM) and the T-test similar to previous fNIRS studies.(144-146) With the application of Bonferroni's correction for multiple comparisons (146), a pixel with $p < 0.0001$ was considered to have significant cortical activity relative to background fluctuations to create HbO activation images from the calculated activation amplitudes for each pixel.

Afterwards, pixel locations significantly active before, during, or after tDCS were used to compute a synchronization likelihood (*SL*) metric for the resting-state connectivity analysis (190), previously used in EEG and fMRI resting-state connectivity analysis (191), but to our knowledge not used for fNIRS. In order to show the connectivity between cortical areas, pixels were grouped into their respective cortical regions as identified by fNIRS functional mapping with the sensory, finger tapping, or sequential tapping tasks (Fig. 4-1). The group averaged time series for each cortical region determined connectivity between sensorimotor cortical areas. Having M number of cortical regions

where $k = 1 \dots M$, the SL metric was first computed by converting each cortical region's baseline time series into a matrix $X_{k,i}$ in which the columns were the time delayed time series obtained using time delay embedding (190), where N was the length of each time series, L the time lag, m the embedding dimension, and $x_{k,i}$ represented the starting sample point of the series where $i = 1, 2, \dots, N - (m-1)*L$ as reported in Eq. 4-1.

$$X_{k,i} = \left[x_{k,i}, x_{k,i+L}, x_{k,i+2L}, \dots, x_{k,i+(m-1)*L} \right] \quad (4-1)$$

SL is a symmetric measure of the strength of synchronization between the baseline time series of two cortical regions. Comparing two different cortical region's matrices X and Y , the SL is the conditional likelihood that the distance between Y_i and Y_j is smaller than a cut-off distance r_y , given that the distance between X_i and X_j is smaller than a cut-off distance r_x . In practice, the cut-off distances are chosen such that the likelihood of random vectors being close is fixed at P_{ref} , which is assumed to be invariable for Y_i and X_i . In this study, r_x , r_y , and P_{ref} were set at 0.05 as was done in previous studies (190, 191). In Eq. 4-2, the SL is calculated by averaging over all time points and time delayed vectors in each matrix where the $|\cdot|$ operator represents the Euclidean distance between the vectors, N is the number of vectors, ω is the Theiler correction for autocorrelation (190), and θ is the Heaviside function: $\theta(x) = 0$ if $x > 0$ and $\theta(x) = 1$ if $x < 0$. From Eq. 4-2, it can be seen that in the case of complete synchronization $SL=1$, for complete independence $SL=P_{ref}$, and for intermediate levels of synchronization $P_{ref} < SL < 1$. Cortical regions were considered functionally connected if $SL \geq 0.8$, as was done in previous studies (190, 191).

$$SL = \frac{2}{N(N-\omega)P_{ref}} \sum_{i=1}^N \sum_{j=1+\omega}^{N-\omega} \theta(r_x - |X_i - X_j|) \theta(r_y - |Y_i - Y_j|) \quad (4-2)$$

In comparison to the normalized cross-correlation connectivity analysis that requires multiple seeds to compare the connectivity of multiple cortical regions, the *SL* metric is able to calculate connectivity between multiple regions without the need of a seed. Importantly, normalized cross-correlations connectivity maps usually present the entire range of correlation values. However, the connectivity maps using the *SL* metric only include those connections with a correlation coefficient above 0.8. Therefore in maps of the *SL* metric weaker inter-hemispheric connections are not displayed, in contrast to what is shown in studies using the normalized cross-correlation metric.

4.2.6 sEMG Signal Analysis

The analysis in this study focused on the blocks when the subjects were performing the wrist-flexion task of the left arm (Fig. 4-3). Mirror movements were not observed in the right arm, and proximal muscle activation was minimal in the biceps and triceps muscles of the target left arm during the wrist flexion task. sEMG signals were band-pass filtered between 20 - 200 Hz, full-wave rectified and low-pass filtered at 6 Hz giving a linear envelope of the muscle activity. Using cross-correlation analysis, insignificant ($r < 0.30$) cross-talk (192) was found between sEMG signals at different muscle groups. The area under each curve (AUC) was used as a metric to compare the muscle activity before, during, and after tDCS. Additionally, the root mean square (RMS), using a 20 ms moving window of the full-wave rectified left WF sEMG signal, was used to calculate the reaction time. The reaction time was obtained by calculating the difference between the stimulus presentation time and the intersection of the time varying mean value of the resting RMS and the linear regression of the RMS signal indicated by an arrow in Fig. 4-4(a) (192). The time interval between the stimulus and the time of the first peak in the torque data (defined in Section 4.2.7.1) was used for the linear regression as

it was the first muscle contraction after the stimulus point before any relaxation. This method of calculating the reaction time is robust to changes in noise between conditions, as increased noise could make the reaction time look spuriously delayed (192).

4.2.7 Torque Task Performance Metrics

We identified task performance metrics (initial speed and accuracy, as defined below) from the torque data collected by the hand device before, during, and after tDCS. The mean (μ_B) and standard deviation (σ_B) of the baseline signal was calculated from the initial 10 s of rest at the beginning of the protocol. For the quantification of subject performance metrics, cursor displacement data were only included if the magnitudes of these displacements were 3 standard deviations above the mean value of baseline fluctuations. The baseline fluctuations occurred during the rest periods as identified by the torque and sEMG data.

4.2.7.1 Initial Speed

To show differences in the speed in which each subject moved the cursor when applying their initial torque on the hand device, the initial speed of the cursor motion was calculated for each task block as the average slope of cursor displacement [S_i in Fig. 4-4(b)] between the time the cursor was first above baseline fluctuations [bottom solid white line in Fig. 4-4(b)] and the first peak [P1 in Fig. 4-4(b)]. Peaks in the torque data were determined by the 'findpeaks' function available in the Signal Processing Toolbox of MATLAB R2012a. The initial speed was defined by Eq. 4-3 where S_i is the initial speed, P1 is the value of the first peak that was above baseline, $t_{0.10}$ is the time at which the torque reached 10% the displacement between the baseline threshold and P1 [bottom

white dash in Fig. 4-4(b)], and $t_{0.90}$ is the time at which the torque reached 90% of the displacement between the baseline threshold and P1 [top white dash in Fig. 4-4(b)].

$$S_i = \frac{0.80 \times P_1 - 0.80 \times (\mu_B + 3 \times \sigma_B)}{t_{0.90} - t_{0.10}} \quad (4-3)$$

4.2.7.2 Accuracy

In addition to initial speed, the stability needed to bring the cursor into the narrow target window and keep it there for 1 s was also measured by an error variance metric. The error variance was calculated as the standard deviation of all the peaks [red circles in Fig. 4-4(b)] and dips [green diamonds in Fig. 4-4(b)] above the baseline fluctuations [bottom solid white line in Fig. 4-4(b)], as indicated by the white double arrow in Fig. 4-4(b). An increase in accuracy was identified by a decrease in the error variance metric.

4.2.8 Statistical Analysis

A two-way repeated measures analysis of variance (ANOVA) test was performed followed by the Tukey post-hoc multiple comparison test, using Prism 6 (GraphPad Software Inc., La Jolla, California) to see if there was a significant difference ($p < 0.05$) in the mean AUC and reaction time of the sEMG data, and the torque performance metrics. This analysis was performed separately for each tDCS current polarity. The null hypothesis was defined as a zero change in muscle activity before, during, and after tDCS. The Brown-Forsythe and Bartlett's tests were also used to see when the variances between groups were found to be significantly different ($p < 0.05$). Statistical power ($1-\beta$) was also determined for each statistical test in order to show the subject pool size was adequate for the findings in this study.

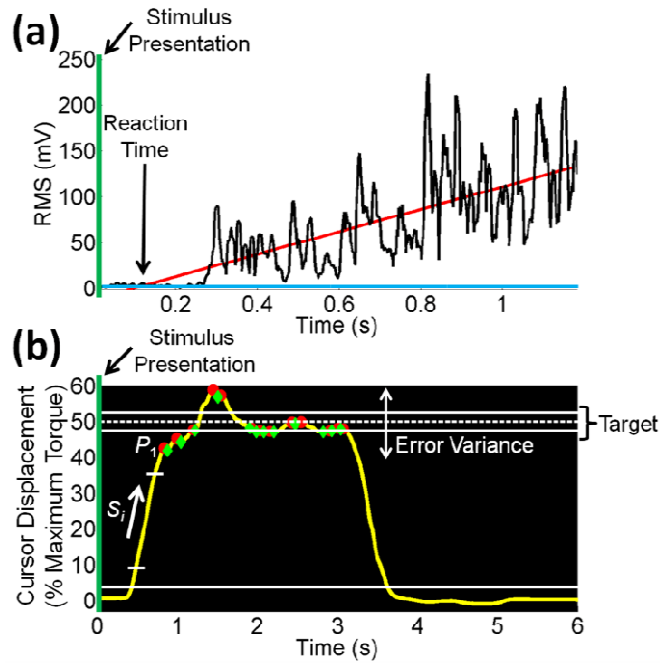


Figure 4-4 (a) The reaction time, indicated by an arrow, is calculated by the time difference between the stimulus presentation (green lines) and the intercept of the linear regression (red line) of the RMS signal (black line) and the mean rest condition RMS signal (blue line) from the left WF muscle. (b) This figure presents the torque data for a single block during a 50% of the maximum torque. The cursor displacement as torque was applied during the task is represented by the yellow line as it was aimed into the target which was centered at 50% of the maximum torque (dashed white line) with a width of 2.5 % of the maximum torque (two top solid white lines). The data used for the analysis in this study was above a baseline cut-off represented by the bottom, solid white line. Additionally, the peaks and dips are shown by red circles and green diamonds respectively, as these were used to calculate the error variance metric. Moreover, the initial speed (S_i) was calculated between the baseline cut-off and the first peak (P_1) as indicated by the two white dashes.

4.3 Results and Discussion

4.3.1 tDCS Effects on Changes in HbO in the Rest Condition

As the signal in fNIRS active condition is computed as an activation-related change relative to the preceding rest condition as baseline, it was important to first explore the changes in hemodynamics in the rest condition during and after tDCS. Fig. 4-5(a) presents time plots for a representative single subject (Subject 5) that demonstrate the initial rapid increase and subsequent new plateau in HbO change after the start of tDCS. The HbO concentration simultaneously increased to a new plateau within 153.48 ± 23.12 s of tDCS application in all cortical areas involved, and persisted 25 - 42 minutes after the end of tDCS. As indicated in Fig. 4-5(b), the new plateau was found to be

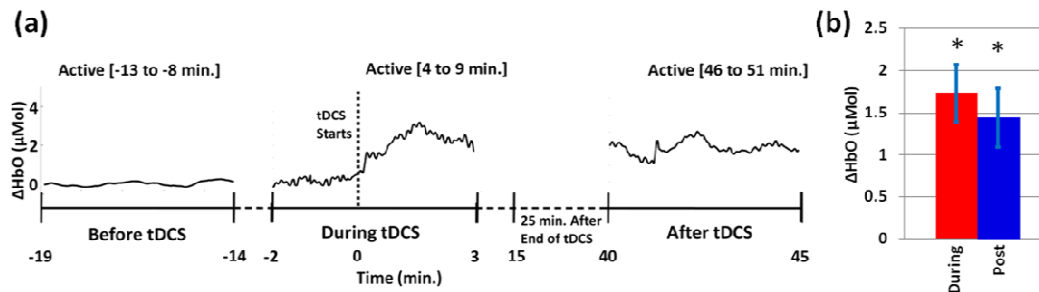


Figure 4-5 (a) This figure presents HbO concentration changes during the rest condition before, during, and after tDCS for a single subject (Subject 5) at M1 under the anode. After each resting-state condition, measurements were taken during the isometric wrist flexion task (active) task. The times at which these measurements were taken compared to the onset of tDCS are indicated above their respective resting-state measurements. (b) Additionally, the group average change in the baseline ΔHbO at M1 under the anode, inclusive of both hemispheres, is presented as a bar graph. The asterisk represents a significant ($p < 0.05$) change when compared to before tDCS.

significantly larger than the pre-tDCS baseline HbO change ($p < 0.0001$, $1-\beta = 1.0$) during and after tDCS across all subjects. Baseline HbO changes presented in Fig. 4-5(b) were independent of the hemisphere the anode was placed ($p = 0.4372$). For a similar tDCS protocol, a previous study found that the hemodynamics returned to their original level a week after tDCS application (53). To optimize our protocol, the active wrist flexion task did not begin until 3 minutes after the start of tDCS to minimize large hemodynamic changes induced by the ramp up of current from corrupting the activation-related hemodynamics.

4.3.2 tDCS Induced Changes in Cortical Activity during an Active Isometric Task

A group analysis of the resting-state connectivity and activation patterns during the active task for all eight subjects was performed and results from before, during and after tDCS were compared to one another (Fig. 4-6). Before tDCS, cortical regions were functionally connected intra-hemispherically, including the SMA which was associated with M1 and S1 during the resting state [Fig. 4-6(a)]. Wrist flexion induced bilateral activation in the SMA and the PMC [Fig. 4-6(d)], in addition to contralateral (right) M1/S1 activation. These pre-tDCS results were similar to ones previously reported in an fMRI study of subjects performing a similar task (193). During tDCS [Fig. 4-6(b) and Fig. 4-6(h)], bi-hemispheric stimulation unmasked a direct functional connection between the two hemispheres at the expense of intra-hemispheric connections, for both current polarities, that were not detected prior to stimulation [Fig. 4-6(a) and Fig. 4-6(g)]. The increase in direct bilateral connectivity was also reflected in the corresponding activation images as bilateral activation of M1 and S1 during the wrist flexion task [Fig. 4-6(e) and

Fig. 4-6(k)]. The increased resting-state variability during tDCS, which caused larger noise fluctuations in the reconstructed images, may have reduced the statistical significance of the group analysis but in all cases, there was considerably less hemodynamic activation in the vicinity of the cathode compared to the anode.

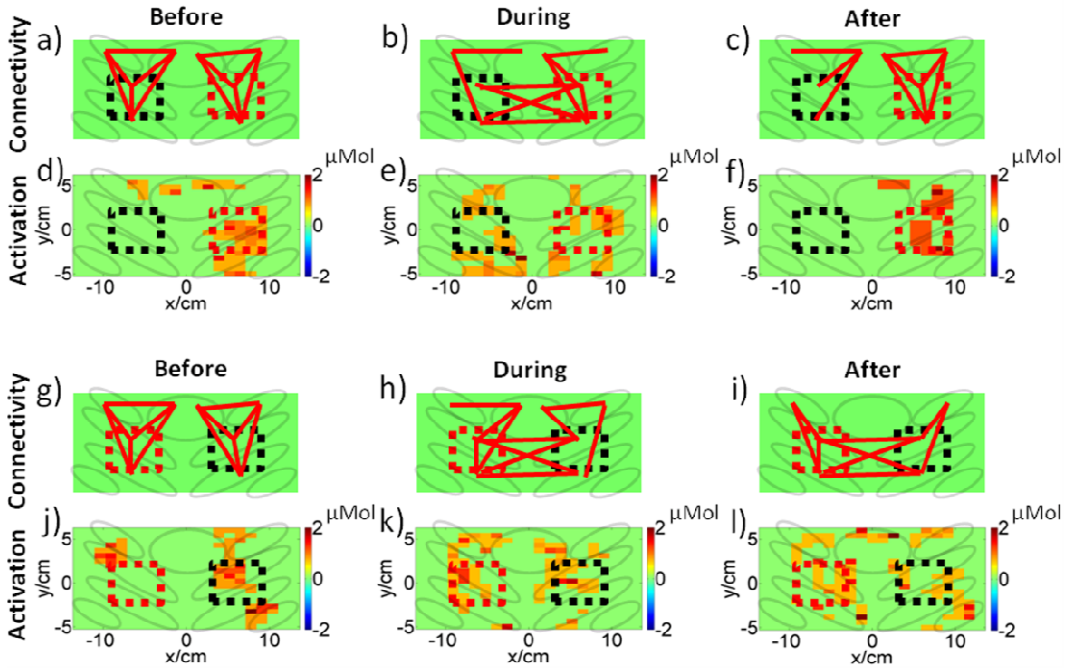


Figure 4-6 Group analysis of the eight subjects for both the resting-state connectivity and activation images before, during, and after the application of tDCS. The top six (a)-(f) and bottom six (g)-(l) panels are separated by current polarity. The solid red lines connect the cortical areas which were functionally connected, the red dashed squares represent the location of the anode, the black dashed squares represent the cathode, and the semi-transparent black ellipses identify the sensorimotor cortical regions previously defined in Fig. 4-1(a).

Interestingly, the resting-state connectivity and activation patterns once again changed after the rest period following tDCS. Remarkably, the modulated cortical

connections differed depending on the applied current polarity. After the cathode was on the hemisphere ipsilateral (left) to wrist flexion [Fig. 4-6(c)], the connections in that hemisphere decreased, leaving only connections to SMA, while the connections in the hemisphere contralateral (right) to wrist flexion returned to pre-tDCS baseline. The decreased connectivity on the ipsilateral (left) side was coupled with a loss of bilateral activation seen before tDCS. In contrast, the return to normal connectivity in the opposite hemisphere was accompanied with an increased hemispheric activation [Fig. 4-6(f)].

When the cathode was on the right hemisphere contralateral to wrist flexion, the inter-hemispheric connections persisted 30 minutes after tDCS [Fig. 4-6(i)], while bilaterally the SMA was notably disconnected. As expected, this inter-hemispheric connectivity correlated with bilateral M1 activity, with stronger activation intensity on the stimulated ipsilateral (left) side compared to pre-tDCS values [Fig. 4-6(l)]. Inter-hemispheric connections are possibly the reason why the ipsilateral (left) hemisphere was easily recruited to compensate for the suppressed contralateral (right) hemisphere. Therefore, these measurements show that tDCS can transiently affect the laterality of sensorimotor regions participating in the control of arm use, even in healthy subjects. The observed dependence of activation on stimulation polarity is in line with a previous bi-hemispheric tDCS study which demonstrated, using TMS, an increase in cortical excitability on the anodal stimulation side and a decrease in the cathodal stimulation side (71).

4.3.3 tDCS Effects on Muscle Activity and Reaction Time

The application of tDCS also affected muscle activity and reaction time during the wrist flexion task. Bi-hemispheric tDCS, with the anode over the contralateral (right) M1 (Fig. 4-7, left column) only increased the AUC significantly ($p < 0.05$, $1-\beta = 1.00$) in both

left WF [Fig. 4-7(a) and Fig. 4-7(c)] and WE [Fig. 4-7(b) and Fig. 4-7(d)] after the rest period following tDCS. The sensorimotor cortical regions responsible for the left WF and WE muscle groups were likely simultaneously stimulated by the large tDCS electrodes, resulting in increased muscle activity of both agonist/antagonist muscles. Four of the eight subjects presented a significant increase in the left WF activity during tDCS, however this did not show significance in the group analysis. The reaction time for the flexion task significantly ($p < 0.05$, $1-\beta = 0.82$) increased for the entire group during tDCS, but not after the rest period [Fig. 4-7(e)] during the time of greatest muscle recruitment.

In contrast, when placing the cathode over the right hemisphere contralateral to wrist flexion (Fig. 7, right column), only the left WF significantly ($p < 0.05$, $1-\beta = 1.00$) increased in activity after the post-tDCS rest period [Fig. 7(f) and Fig. 7(h)]. There was no effect on the WE, and reaction time did not significantly change during or after tDCS [Fig. 7(j)]. These results suggest that tDCS not only directs cortical plasticity, but can also affect which of the muscle groups being used have increased activation, in a manner dependent on current polarity. Importantly, the biceps were also active during the isometric wrist flexion task, yet tDCS only significantly affected the left WF and WE muscle groups (data not shown). Additionally, previous studies suggest that lasting improvements in reaction time may require applying tDCS to planning centers of the brain such as the prefrontal or PMC (57, 194).

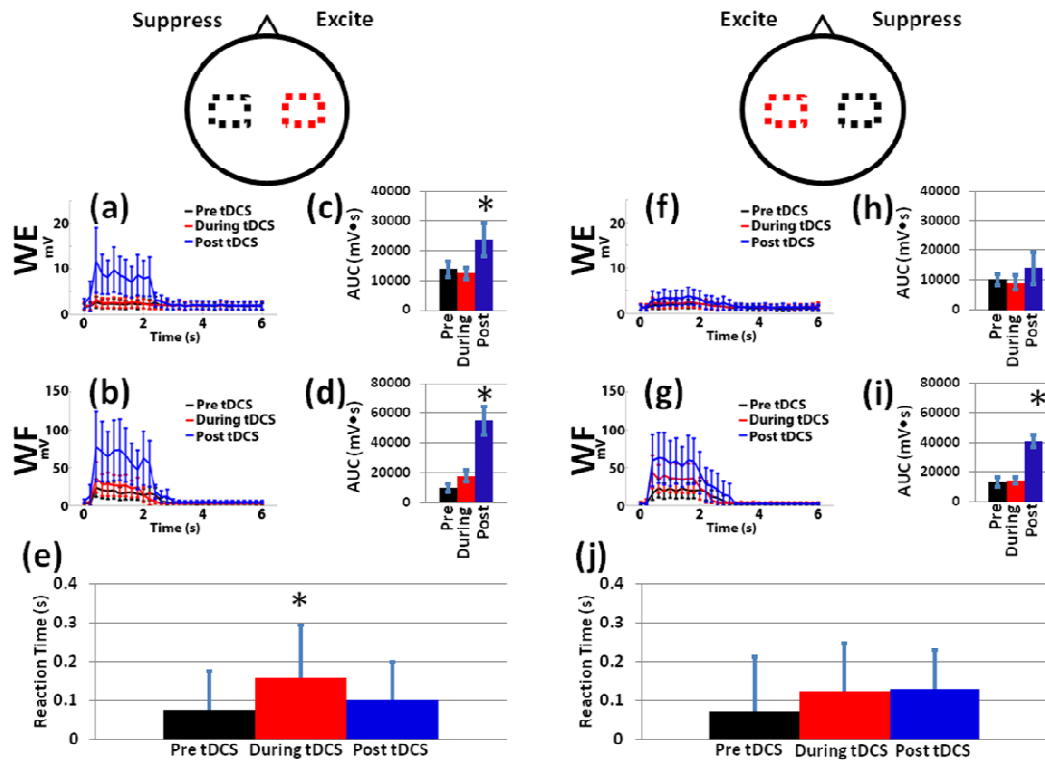


Figure 4-7 The analysis of muscle activity measured by sEMG before, during, and after tDCS for both current polarities. The average time series linear envelope of the sEMG from the left (a) WE and (b) WF for the eight subjects, the statistical analysis of AUC for the left (c) WE and (d) WF, the statistical analysis of the reaction time from the left WF (e) is presented when the anode (red dashed square) was located over the right hemisphere and the cathode (black dashed square) over the left hemisphere. The same is also presented when the electrode positions were switched for the (f) WE and (g) WF average time-series envelope, AUC statistical analysis for the left (h) WE and (i) WF, and the reaction time for the left (j) WF. The asterisk identifies statistical significance ($p < 0.05$).

4.3.4 tDCS Effects on Torque Task Performance

Changes in the speed of reaching the first peak during wrist flexion are shown as a function of WF and WE muscle activation for the two different bi-hemispheric tDCS current polarities in Fig. 4-8. Anodal placement over the right hemisphere that was contralateral to wrist flexion [Fig. 4-8(a)-(b)], increased WF activity during tDCS, increasing the initial speed to reach the first peak compared to pre-tDCS values. The increases in WF activation and speed during tDCS were not significant in the group analysis, but increased significantly in the same four subjects mentioned in Section 4.3.3. For the four subjects with increased WF activity, the speed with which the first peak was reached was higher by $25.33 \% \pm 5.67 \%$. The increase in WF and WE activity following tDCS [Fig. 4-7(c)-(d)] decreased the speed to first peak during wrist flexion with statistical significance ($p < 0.05$, $1-\beta = 0.82$). Four of the eight subjects presented a significant improvement in accuracy after tDCS. However, this did not show significance in the group analysis. This observed decrease from the initial speed pre-tDCS may result from the fact that WF and WE are antagonistic muscles, pulling against each other and therefore slowing each other, which ultimately may increase motor control leading to better accuracy at the price of decreased speed.

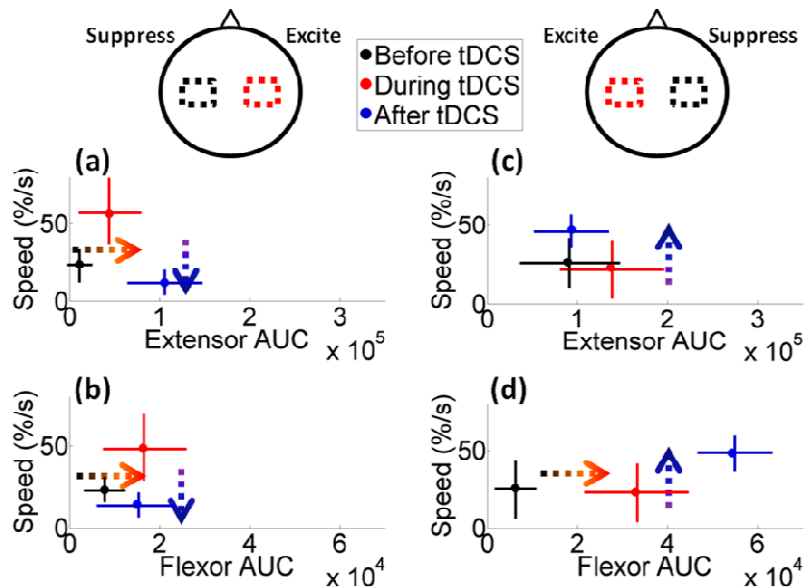


Figure 4-8 Scatter plots for a representative subject's (Subject 3) initial speed in reaching the first peak before (black dots), during (red dots), after (blue dots) tDCS, with correspondingly color coded standard deviations from nine trials, versus the integrated muscle activity (AUC) for the left WE and WF. The polarity of tDCS during these measurements is shown at the top of each figure column. The effect of placing the anode (red dashed square) over the non-dominant (right) hemisphere on initial speed is compared to the AUC of the left (a) WE and (b) WF. The same is represented for the left (c) WE and (d) WF when the tDCS electrode placement is switched. Color coded arrows show the direction of statistically significant changes from before-to-during tDCS (black to red) and from during-to-after tDCS (red to blue). Horizontal arrows show the direction of changes in muscle activity and vertical arrows show the direction of changes in task performance speed.

Table 4-1 A summary of the cortical activity, muscle activity, and task performance results of the active condition compared to the rest condition. The asterisks indicate those sEMG and torque performance metrics which were found to be significant over the entire group. Those metrics without an asterisk were found significant for at least four of the eight subjects, but were not significant in the group analysis.

| Cathode (left)/ | | <i>Muscle</i> | <i>Task</i> |
|------------------------|--------------------------|-----------------|--------------------|
| Anode (right) | <i>Cortical Activity</i> | <i>Activity</i> | <i>Performance</i> |
| <i>Before tDCS</i> | ↑ Contralateral (Right) | ----- | ----- |
| <i>During tDCS</i> | ↑ Contralateral (Right), | ↑ WF | ↑ Speed; |
| | ↑ Ipsilateral (Left) | | ↑ Reaction Time* |
| <i>After tDCS</i> | ↑ Contralateral (Right), | ↑ WF*; ↑ WE* | ↓ Speed*; |
| | ↓ Ipsilateral (Left) | | ↑ Accuracy |
| Anode (left)/ | | <i>Muscle</i> | <i>Task</i> |
| Cathode (right) | <i>Cortical Activity</i> | <i>Activity</i> | <i>Performance</i> |
| <i>Before tDCS</i> | ↑ Contralateral (Right) | ----- | ----- |
| <i>During tDCS</i> | ↑ Contralateral (Right), | ----- | ----- |
| | ↑ Ipsilateral (Left) | | |
| <i>After tDCS</i> | ↑ Contralateral (Right), | ↑ WF* | ↑ Speed* |
| | ↑ Ipsilateral (Left) | | |

The cathode over the hemisphere contralateral to wrist flexion that increased WF activity after tDCS [Fig. 4-7(h)] also significantly increased ($p < 0.05$, $1-\beta = 0.93$) the speed of wrist flexion [Fig. 4-8(c)-(d)], which was an effect not found during tDCS. Yet, in this case the WE did not increase in activity after the contralateral hemisphere was suppressed. The unchanged WE activity resulted in a reduced antagonist effect to the

excited WF, which in turn resulted in increased initial speed and no significant change in accuracy. Two previous studies also presented tDCS-induced changes in hand task performance in healthy controls (34, 185). In one study, the time it took to perform multiple tasks decreased after uni-hemispheric anodal stimulation (185), while the sequential finger tapping rate increased after uni-hemispheric and bi-hemispheric tDCS (34). In these studies, it was concluded that tDCS may have a stronger effect on speed than on accuracy, which is similar to what was found in this study.

Previous studies have found performance changes during tDCS, yet found these changes to be most significant 15 minutes after the start of stimulation in healthy adults (87, 195). However, continuous monitoring of muscle activity and performance with stimulation time was not performed in this study. Since this study monitored for these changes early into the stimulation period, it may have been too early into the stimulation to find significant changes in initial speed and muscle activity. The during and after tDCS differences in muscle activity and initial speed could be explained by motor learning long-term potentiation (LTP)-like changes within the inter-neurons of M1 (196-198). Since LTP-like plasticity has the potential to destabilize established cortical networks (199), metaplastic mechanisms have been proposed to maintain neural activity within a useful range (200, 201). Metaplastic mechanisms are usually network specific, such that tDCS will only modify the response to the wrist flexion task if these two stimuli involve the same groups of circuits and synapses (202). Metaplasticity has been demonstrated in humans, when the effects of a train of TMS pulses normally insufficient to induce excitability changes become inhibitory if applied after anodal tDCS, and become excitatory if applied after cathodal tDCS (203, 204).

An additional factor to take into consideration is the prevention of subject expectation effects by blinding subjects between no tDCS and tDCS conditions. In this

study subjects were blinded to the type of montage was being applied between the two visits, however they were not blinded between non-stimulation and stimulation conditions. Fortunately, blinding subjects of the polarity prevented expectations of polarity dependent performance changes. Yet, the ineffective blinding of non-stimulation and stimulation states may have lead to expectation effects as tDCS was applied. Sham tDCS is typically used as a control to prevent subjects from knowing non-stimulation from stimulation conditions. According to one study (168), subjects can feel a tingling or burning sensation on their scalp for current levels exceeding 0.4 mA and for durations up to 30 s. Thus studies have applied sham with different current levels and times within these parameters. For example, 1 mA for 30 s (205) or 1.5 mA for 30 s (206). However, in some studies it was found that patients could feel a difference between sham and tDCS (179, 206), and that these procedures have not always been effective in various tDCS protocols (207-210). Importantly, during stimulation using a high current density (0.0571 mA/cm^2), neither the practitioner nor participant was effectively blinded (211). Additionally, itching, tingling, or burning differences between active and sham stimulation make blinding participants who undergo multiple conditions difficult at any current density (209). Instead of sham, it could be suggested that using the opposite polarity of the one studied could be used as a control, which would be true in this study. However, this does not prevent expectation effects between no tDCS and tDCS conditions. Unfortunately there is no reliable control protocol for tDCS to date.

Importantly, unlike previous studies, this work demonstrates how the link between cortical activation and muscle activity can explain observed changes in task performance. Table 4-1 contains a summary of the cortical activity, muscle activity, and task performance changes as a function of tDCS current polarity.

4.4 Conclusions

This study compared altered hemodynamic patterns in the sensorimotor cortex in response to two possible bi-hemispheric tDCS polarities, and related these changes to concurrently observed muscle group activity and task performance during a wrist flexion task. fNIRS enabled mapping of the resting-state connectivity during tDCS, using an SL metric, which has not been previously studied with this imaging modality. Changes in resting-state connectivity were task- and polarization-specific, and persisted for over 40 minutes after the end of stimulation. These results showcase the effectiveness of bi-hemispheric tDCS to alter inter-hemispheric balance and the laterality of cortical activity, which in turn affects muscle activity, speed, and reaction time in a manner dependant on current polarity. The combination of tDCS, fNIRS, and sEMG with task performance measurements can become a much-needed multiparametric tool for exploring how cortical plasticity changes muscle control, particularly during rehabilitative physical therapy interventions. The presented methods could be used in future clinical studies to tailor the stimulation parameters for tDCS-enhanced physical therapy on an individual, per patient basis, which will be significantly beneficial for patients with complex neurological disorders such as stroke or traumatic brain injury.

Chapter 5

Perturbation Transcranial Direct Current Stimulation (ptDCS)

5.1 Introduction

Augmentation of rehabilitation with concurrent cortical stimulation is a valuable approach for facilitating plasticity in the injured human brain to improve physical performance. Cortical stimulation methods used in current clinical practice include repeated transcranial magnetic stimulation (rTMS) and transcranial direct current stimulation (tDCS). rTMS uses repeated magnetic pulses to either suppress (0.2 - 1 Hz) or excite (> 2 Hz) cortical neurons with a spatial resolution of ~ 1 mm. Pulses delivered by rTMS cause action potentials to be sent by the cortical neurons resulting in twitching in the muscles. In contrast, tDCS uses a pair of electrodes placed on the scalp to inject sub-threshold direct current into the cortex. tDCS can either suppress (cathode) or excite (anode) cortical region under the electrodes with a spatial resolution in the centimeter range. However, advantages of using tDCS over rTMS include the ability to stimulate during a motor task even if it involves head or torso movements, low cost, and excellent tolerability.

Typically tDCS is popularly used with three different electrode arrangements for motor performance recovery in stroke patients: 1) Anodal tDCS (A-tDCS) montage is when the anode electrode is placed over the ipsilesional primary motor cortex (M1), and the cathode is placed over the supra-orbital bone of the contralesional hemisphere. This montage is meant to help regain function by exciting the injured area. 2) Cathodal tDCS (C-tDCS) montage is meant to suppress the activity of the contralesional hemisphere by placing the cathode over the contralesional M1 and the anode over the supra-orbital bone of the ipsilesional hemisphere. 3) Bi-hemispheric tDCS or dual tDCS montage has the

anode placed over the ipsilesional M1 and the cathode over the contralesional M1. This montage incorporates the advantages of A-tDCS and C-tDCS in order to reduce the impedance of transcallosal inhibition of the contralesional hemisphere. All three montages have presented improvements in functional assessment scores and reaction time (RT) in stroke patients. Additionally, A-tDCS and dual tDCS have shown improvements in accuracy and overall skill (i.e. speed-accuracy tradeoff curve).

Nevertheless, the benefit of using tDCS differs between stroke patients. For example, A-tDCS had improved performance in stroke patients with sub-cortical lesions, but not those with cortical lesions (38). Such a study has not been done with dual tDCS, though this indicates that the underlying physiology has a high impact on the type of tDCS montage used. To our knowledge, there are no studies which compare motor performance improvement of multiple tDCS electrode montages which include motor planning and execution centers of the brain. Variable results have been found between the few studies have compared dual tDCS to A-tDCS. Some of which have shown a larger increase in performance when applying dual tDCS on stroke patients, and others that show no difference between the two montages. It may be that an optimal tDCS montage for motor recovery may differ between patients due to their unique underlying physiology. Thus a method is needed to determine which montage is optimal for each individual patient. Fortunately, unlike other therapy methods, noticeable effects due to tDCS happen within minutes, thus giving the potential to implement a protocol which can optimize the use of tDCS within a single session.

In this study a new method, which we name perturbation tDCS (ptDCS), is introduced as a way to optimize tDCS electrode placement. The protocol used a current and duration less than those used in therapy which reduced the tDCS effects on the brain motor network to a few minutes, allowing for multiple stimulation protocols to be

performed within a single session. Specifically in this study, tDCS electrode montages were focused over the motor execution and planning cortical areas. Additionally, concurrent monitoring of tDCS effects on brain activity, muscle activity, and task performance were used to identify optimal montages as an isometric wrist flexion task was performed during tDCS. Functional near-infrared spectroscopy (fNIRS) enabled the quantification of resting-state cortical connectivity and functional activity during the wrist flexion task. The isometric wrist flexion task was performed while subjects held a lever outfitted with sensors to measure the torque, allowing quantification of RT and accuracy of task performance in relation to cortical activity. Moreover, changes in the activity of the forearm and upper arm muscles, measured by surface electromyography (sEMG) concurrent with fNIRS, yielded complementary information on how the activation of specific muscles related to changes in cortical activation patterns elicited by wrist flexion. The results of this work indicate how the combined use of fNIRS, sEMG and task performance measurements can guide the personalized electrode placement for tDCS-enhanced physical therapy making stroke rehabilitation more patient-specific.

5.2 Methods and Materials

5.2.1 Subjects

A summary of the experimental groups can be found in Table 5-1. Ten healthy right handed subjects (3 female and 7 male; 31 ± 7 years old) and five hemiparetic ischemic stroke patients (5 male; 52 ± 10 years old) were included in this study. All healthy subjects did not have a history of neurological disorders other than headaches. The studies were performed under the approval of the University of Texas at Arlington Institutional Review Board protocol (IRB No.: 2012-0356).

Table 5-1 Participants' demographics: protocol, group category, group size, gender, handedness, and age.

| Protocol | Healthy/ Stroke | Number | Male/Female | Handedness | Age |
|--|--------------------|--------|-------------|------------------|---------|
| Optimal Electrode Placement | Healthy | 10 | 7/3 | 10 Right | 31 ± 7 |
| Current Titration/ Scalp Effects | Healthy | 6 | 5/1 | 6 Right | 27 ± 3 |
| Repeated tDCS Montage | Healthy | 6 | 5/1 | 6 Right | 28 ± 6 |
| Optimal Electrode Placement | Stroke | 5 | 5/0 | 3 Right / 2 Left | 52 ± 10 |

5.2.2 Instrumentation Setup

There were two separate tDCS and fNIRS setups used in this study. The first setup was primarily designed to validate that tDCS effects on scalp hemodynamics did not affect fNIRS cortical hemodynamic measurements during tDCS. This setup is explained in Appendix C. The second setup was used to determine the personalized tDCS electrode placements which is described here.

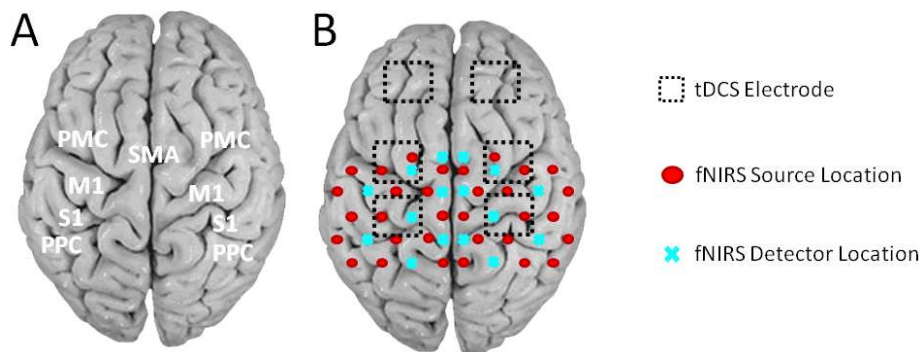


Figure 5-1 TDCS and fNIRS setup. (A) Displays the cortical regions contained within the fNIRS field of view. (B) Displays the tDCS electrode placement (black dashed square), fNIRS source placement (red circles), and fNIRS detector placement (blue Xs) used during the ptDCS protocol.

For determining the personalized tDCS electrode placement the tDCS electrode montage, fNIRS source-detector geometries, and the cortical regions they were placed over are shown in Fig. 5-1. TDCS current was applied by a battery-driven electrical stimulator (Phoresor II, IOMED Inc., Salt Lake City, Utah) connected by a pair of saline-soaked gauze covered gel electrodes [dashed boxes in Fig. 5-1B; 5 x 5 cm; IOMED Inc., Salt Lake City, Utah]. Six tDCS electrodes were placed on the scalp (Fig. 5-1B). Two electrodes were placed over the C₃ and C₄ positions of the EEG International 10/20 system (180), two were placed 3.5 cm anterior to those placed over the C₃ and C₄ positions over the pre-motor cortex (PMC), and two were placed over the supra-orbital bone (SO) of each hemisphere in which all 20 possible tDCS montages were applied in this study (Fig. 5-2). In order to accommodate the placement of fNIRS sources and detectors within the area covered by the tDCS electrodes, 0.5 cm diameter holes (standard hole punch size) were made so that the optical fiber bundles could fit through them. After the tDCS electrodes were placed, a continuous wave fNIRS brain imager (CW-6, Techen Inc., Milford, Massachusetts) source and detector fiber bundles was placed to map the changes in oxy-hemoglobin (ΔHbO) induced by sensorimotor cortex activity before and during tDCS. The CW-6 allows up to 32 detectors (Fig. 5-1B, light blue X's) and 32 sources, in which half emit at 690 nm and other half at 830 nm, such that each source optical fiber bundle delivered light of both wavelengths at each source location (Fig. 5-1B, red circles) simultaneously. The source-detector geometry was previously described in Chapter 4. All source-detector pairs simultaneously monitored activation in cortical areas within the probes' field of view, as the CW-6 system enables all laser sources to be on at the same time with distinct modulation frequencies (6.4 -

12.6 kHz, with an increment of 200 Hz). Back-reflected light was sampled at a rate of 25 Hz.

In addition to the tDCS and fNIRS setup, isometric contractions of the WF (flexor carpi radialis muscle), WE (extensor carpi radialis muscle), biceps brachii, and triceps brachii muscles of both arms were measured by sEMG (Brain Vision LLC, Morrisville, North Carolina). Also, a custom hand device (JR3 Inc., 35-E15A, Woodland, CA) measured the isometric moments exerted by each test subjects on a static Delrin[®] handle. A more detailed description of the sEMG and torque measurement setup was also explained in Chapter 4.

5.2.3 ptDCS Protocol

Each subject was comfortably seated up-right in a dim room, such that all subjects used their non-dominant (healthy subjects) or affected (stroke patients) arm in this study. The torque measurements were normalized to the subject's maximum isometric wrist flexion contraction force, and expressed as a percentage of maximum torque to standardize strength and function effort across subjects as previously explained

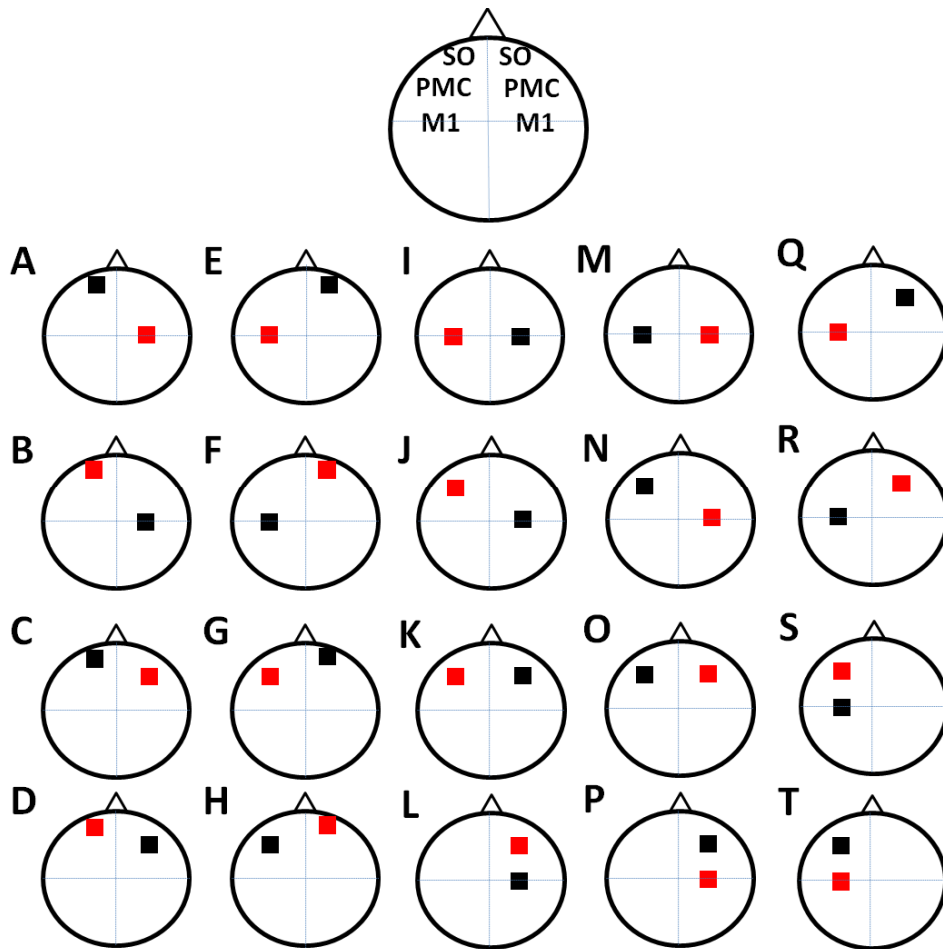


Figure 5-2 Twenty different tDCS montages used in this study. Locations of each electrode correspond with the diagram at the top of the figure which are the supra-orbital bone (SO), premotor cortex (PMC), primary motor cortex (M1). Red squares represent an anode and black squares represent a cathode.

in Chapter 4. In a single two hour sitting, each subject underwent 21 sets of measurements, one without tDCS and 20 with tDCS for the different pair-wise combinations of tDCS electrodes (Fig. 5-3A). The protocol for a single measurement consisted of 60 s of rest, followed by seven equally timed sets of the isometric wrist

flexion task for 40 s, and ended with 180 s of rest (Fig. 5-3B). The seven sets of the isometric wrist flexion task were set at 50% of the maximum torque for healthy subjects and 30% for stroke patients, with a target width of 2.5% of the maximum torque. Stroke patients tire more easily when using their affected arm, thus a lower percent torque was used for them. The goal was to move the cursor into the target and hold it there for 1 s. TDCS was applied during the 40 s of the wrist flexion task. Healthy subjects were measured again within two weeks of their first visit with a new randomized order of tDCS electrode montages. Additionally, in six healthy subjects the bi-hemispheric M1 montage was repeated to make sure effects were consistent from the beginning of the ptDCS protocol to the end.

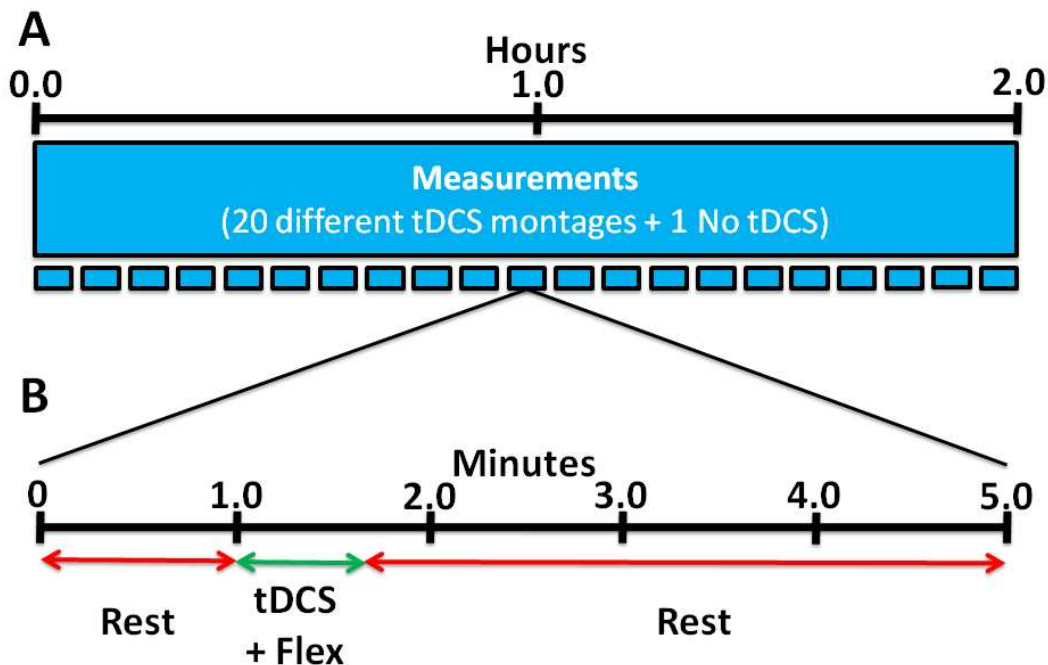


Figure 5-3 PtDCS protocol. (A) Twenty measurements for each tDCS montage was applied on each subject including a measurement without tDCS, resulting in a two hour measurement session. (B) Each measurement included 1 minute of rest, 40 s of tDCS during the wrist flexion, and 3 minutes of rest.

5.2.4 fNIRS Signal Filtering and Image Analysis

In addition to detecting evoked hemodynamic changes, fNIRS is sensitive to cerebral hemodynamic fluctuations of systemic origin caused by cardiac pulsation, respiration, and Mayer waves. This study used a combination of band-pass filtering, adaptive filtering, and component analysis to filter the fNIRS signals as we have previously done. Because ΔHb dynamics are highly correlated with those of ΔHbO but with lower amplitudes and are susceptible to cross-talk from ΔHbO and interference from physiological artifacts, we have focused on the analysis of ΔHbO dynamics only. After each resting measurement, the ΔHbO for the succeeding activation measurements were determined in reference to a baseline value which was taken to be the average from the first minute of resting-state measurement.

Reconstruction and visualization of fNIRS activation images resulting from the acquired reflectance data was performed by the open-source HomER software implemented in MATLAB by use of the Tikhonov perturbation solution to the photon diffusion equation, which employs a regularized Moore-Penrose inversion scheme. The reconstructed, two-dimensional images (21 x 21 pixels) for every 0.04 s time interval represented maps of ΔHbO on the cortical surface, within the detector's field of view (Fig. 5-1). Regions of activation were determined by a general linear model (GLM) and the T-test similar to previous fNIRS studies. With the application of Bonferroni's correction for multiple comparisons, a pixel with $p < 0.0001$ was considered to have significant cortical activity relative to background fluctuations to create ΔHbO activation images from the calculated activation amplitudes for each pixel. Afterwards, pixel locations significantly active before or during tDCS were used to compute a synchronization likelihood (SL) metric for the resting-state connectivity analysis, previously used in EEG and fMRI

resting-state connectivity analysis. A more detailed explanation of the SL metric was provided in Chapter 4.

5.2.5 Performance, EMG, and fNIRS Metrics

Three performance metrics were used in this study: reaction time (RT), Error, and a RT x Error product. RT was calculated from the WF sEMG time-series data as described in Chapter 4. Error was defined as percent difference between the first peak of each attempt in the flexion torque measurements and the center of the target. The Error X RT product was defined as the product of Error and RT. Additionally, changes in muscle activity were determined from the sEMG measurements by an area under the curve (AUC) metric previously defined in Chapter 4. Lastly, fNIRS metrics were the detected area of activation (dAoA), previously defined in Chapter 3, and laterality index (LI) which is a metric bounded between -1 and 1 (212). If the LI equals one it means all cortical activity was in the hemisphere contralateral to the arm used, and if it equals -1 then all cortical activity was in the hemisphere ipsilateral to the arm used.

5.2.6 Neuromuscular Prediction

Since application of tDCS at higher currents had longer time effects and would significantly increase the time needed to determine an optimal tDCS montage, a method was needed to confirm that the direction of cortical and muscular changes due to ptDCS still applied at higher currents. Two neural networks were designed using Matlab's Neural Network Toolbox to predict the ΔHbO time-series and WF linear envelope time-series from lower ptDCS currents (0.5 mA) to larger currents (2 mA) used in therapy.

The first neural network was a recursive neural network designed to predict WF linear envelope time-signal (output) from the ΔHbO time-signal (input) in M1. It consisted of three layers: an input layer, hidden layer, and output layer output was feedback into

the input layer. The second neural network was a feed-forward network which also had three layers in which the WF linear envelope time-signal was used to estimate the ΔHbO time-signal. Since the stimulation period was 40 s, the input layer of each network used a 40 s time-window of the input signal to predict the next time point of the output, where the output layer was a single value at a particular time point. The number of units in the hidden layer were adjusted to achieve maximum predictive accuracy for each subject. In addition to the number of hidden layers, each layer had a node transfer function and weight vector. The transfer function at the input and output was a linear transfer function achieved by using Matlab's `purelin` function. The transfer function used in the hidden layer was a hyperbolic tangent sigmoid function implemented by the Matlab function `tansig`. Network weights were determined by training the network.

Training both networks was achieved by fitting the network parameters to the desired output using back-propagation. The no tDCS condition and measurements which produced significant (P value < 0.05) increased WF AUC due to tDCS were used to train and test this neural network. Each network was customized for each subject to reduce the error in estimation.

5.2.7 Statistical Analysis

A two-way repeated measures analysis of variance (ANOVA) test was performed followed by the Tukey post-hoc multiple comparison test, using Prism 6 (GraphPad Software Inc., La Jolla, California) to see if there was a significant difference ($p < 0.05$) in the mean RT, Error, Error X RT product, and AUC between tDCS montages and the no tDCS condition. This analysis also applied for repeat visits and repeat tDCS montage results to make sure tDCS effects did not change between days or within a single session. Additionally, the repeated measures ANOVA was performed to compare the neural network estimation to measured results. Lastly, one-way ANOVA was used to

compare LI and dAoA results between montages. The Brown-Forsythe and Bartlett's tests were also used to see when the variances between groups were found to be significantly different ($p < 0.05$).

5.3 Results

5.3.1 Short-Lasting *ptDCS-Induced Cortical Effects in Healthy Adults*

Before sequentially applying different tDCS montages, it was important to validate that effects of the previous montage had decayed. The cortical effects of tDCS with current at 0.5 mA for a period of 40 s was found to decay back to pre-tDCS levels 64.3 ± 7.2 s after the end of the stimulation when the person was at rest [Fig. 5-4(A)], and 130.1 ± 10.7 s after the end of the stimulation when performing the wrist flexion task during stimulation (Fig. 5-4B). Thus, it was safe to apply the next tDCS montage three minutes after the end of the previous montage, as described in Section 5.2.3.

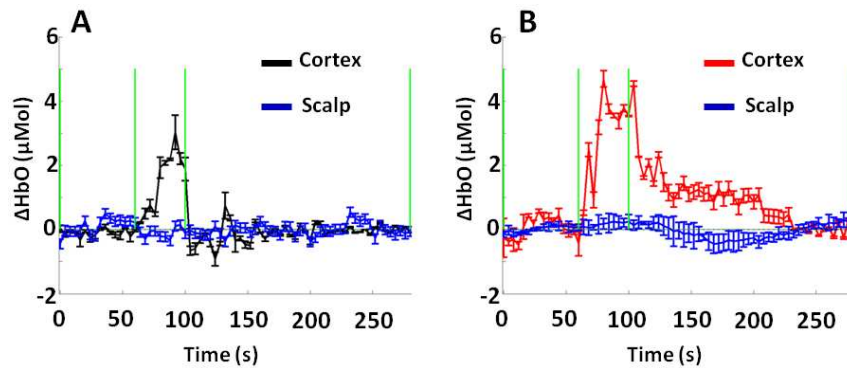


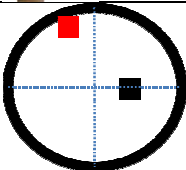
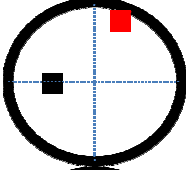
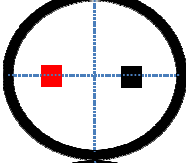
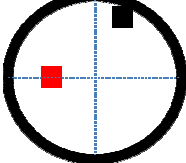
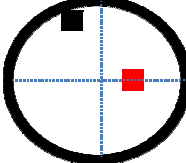
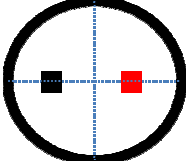
Figure 5-4 TDCS effects on scalp hemodynamics. (A) Presents cortical response to tDCS (black) versus that of the scalp (blue) when subjects were at rest. (B) Presents cortical response to tDCS (red) versus that of the scalp (blue) when subjects were performing the isometric wrist flexion task.

5.3.2 Overview of ptDCS Montage-Specific Effects on Performance in Healthy Adults

Following the ptDCS protocol presented in Fig. 5-3, performance results presented montage-specific differences between healthy subjects for the 20 different tDCS montages (Fig. 5-2) applied in this study. Since all healthy subjects used their left hand for this study, contralateral will refer to the right side and ipsilateral will refer to the left from this point forward. General trends were sought by separating the results by the cortical region being stimulated. Here the separation was made by stimulation of the M1 only, PMC only, and M1-PMC combinations.

The number of subjects which presented significant improvement or worsening by either uni-hemispheric or bi-hemispheric M1 tDCS is presented in Table 5-2 in order from greatest to least improvement of the Error x RT product. For example, the montage that brought about the best performance improvement was the uni-hemispheric suppression (cathode) of the contralateral M1 (Table 5-2, first row). However, three subjects had significantly worse Error due to this stimulation montage, signifying that this montage also had impeding effects for some subjects. Additionally, two montages recently used in literature for stroke patients (Vines 2008; Bolognini 2011; Lefebure 2012), the A-tDCS (Table 5-2, row five) and dual tDCS montage (Table 5-2, last row), presented the least improvement. The former improved the accuracy in one subject and worsened the Error in another, whereas the latter worsened the RT in six subjects and improved the Error in one. Both of these montages had no significant change on the Error x RT product.

Table 5-2 Performance metrics due to each tDCS stimulation applied over only M1 ordered from most improved to least improved.

| | | RT (Improve/Worsen) | Error (Improve/Worsen) | RT x Error (Improve/Worsen) |
|---|---|------------------------|---------------------------|--------------------------------|
| 1 |  | 4/0 | 5/3 | 6/0 |
| 2 |  | 5/0 | 0/0 | 4/0 |
| 3 |  | 3/0 | 4/2 | 3/0 |
| 4 |  | 0/0 | 0/0 | 0/0 |
| 5 |  | 0/0 | 1/1 | 0/0 |
| 6 |  | 0/6 | 1/0 | 0/0 |

Behavioral results due to different tDCS montages only including the PMC areas are also presented (Table 5-3). All the PMC only montages improved the Error x RT product for at least two subjects. Interestingly, bi-hemispheric PMC tDCS when the contralateral PMC was excited (Table 5-3, first row) brought upon significant

improvement in the Error x RT product for all subjects. However, the bi-hemispheric PMC montage with the contralateral hemisphere suppressed (Table 5-3, third row) and the uni-hemispheric excitation of the contralateral PMC (Table 5-3, last row) significantly worsened the Error x RT product in three subjects. Two of these three subjects also had significantly worse Error (Table 5-3, third row).

Table 5-3 Performance metrics due to each tDCS stimulation applied over only PMC ordered from most improved to least improved.


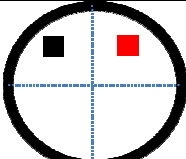
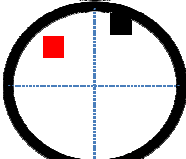
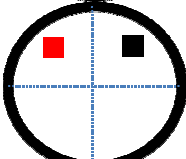
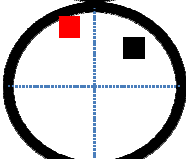
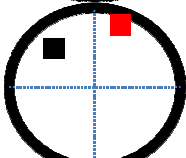
| |  | RT (Improve/Worsen) | Error (Improve/Worsen) | RT x Error (Improve/Worsen) |
|---|---|------------------------|---------------------------|--------------------------------|
| 1 |  | 3/0 | 7/0 | 10/0 |
| 2 |  | 7/0 | 5/5 | 5/0 |
| 3 |  | 0/0 | 8/2 | 5/3 |
| 4 |  | 0/0 | 0/0 | 4/0 |
| 5 |  | 0/0 | 4/0 | 2/0 |

Table 5-3—Continued

| | | | | |
|---|---|-----|-----|-----|
| 6 |  | 0/4 | 3/0 | 3/3 |
|---|---|-----|-----|-----|

Table 5-4 Performance metrics due to each tDCS stimulation applied over different M1-PMC combinations ordered from most improved to least improved.


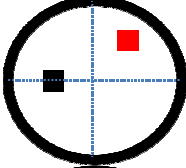
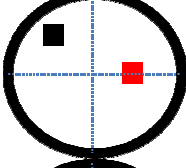
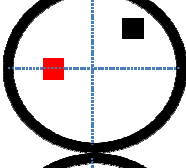
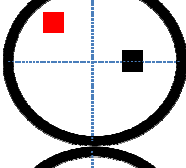
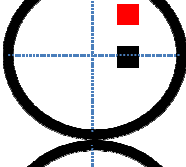
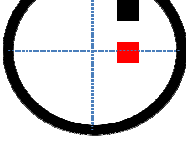
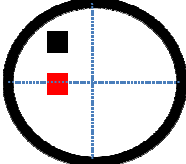
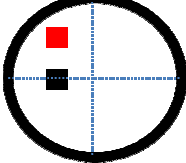
| |  | RT (Improve/Worsen) | Error (Improve/Worsen) | RT•Error (Improve/Worsen) |
|---|---|------------------------|---------------------------|------------------------------|
| 1 |  | 3/0 | 5/0 | 6/0 |
| 2 |  | 0/0 | 4/0 | 6/0 |
| 3 |  | 3/0 | 7/0 | 5/0 |
| 4 |  | 3/0 | 3/0 | 5/0 |
| 5 |  | 0/0 | 0/0 | 5/0 |
| 6 |  | 0/0 | 0/0 | 5/0 |

Table 5-4—Continued

| | | | | |
|---|---|-----|-----|-----|
| 7 |  | 0/0 | 0/0 | 4/0 |
| 8 |  | 0/0 | 0/0 | 3/0 |

Results of M1-PMC combination montages are also shown in Table 5-4.

Fascinatingly, M1-PMC combination montages did not present any significant worsening for any metric. Bi-hemispheric montages of this type (Table 5-4, first to fourth rows) presented the most improvement, specifically when the contralateral hemisphere was excited (Table 5-4, first and second rows). On the other hand, montages that brought upon the least improvement within this group, were the uni-hemispheric combinations placed over the ipsilateral hemisphere (Table 5-4, last two rows).

These findings were found repeatable with measurements taken within two weeks of each other (minimum P value = 0.2312). Additionally, dual tDCS (Fig. 5-2M) was repeated within the session for six healthy subjects. No significant differences were found between the first and second stimulation within the session for this montage (minimum P value = 0.1103). However, the variability in performance between healthy subjects was further investigated.

5.3.3 Comparison of Montage-Specific Effects on Performance Between Subjects

Further understanding of the variability between subjects was sought by comparing the no tDCS condition with the best and worst tDCS montages. The RT x Error product due to the stimulation of each of these montages in each subject can be seen in Fig. 5-5A. The best montage was considered to be the bi-hemispheric PMC

montage where the contralateral PMC was excited (Table 5-3, first row) since all subjects improved (maximum P value = 0.0392) in Error x RT metric. The worst montages were considered to be the A-tDCS and dual tDCS montages (Table 5-2, last two rows) since they presented no improvement in the Error x RT metric and significantly (maximum P value = 0.0417) worsened the RT or Error metric in one or more subjects as seen in Fig. 5-5B and C.

5.3.4 Comparison of Montage-Specific Effects on Muscle Activity Between Subjects

To relate the muscle activity with the change in performance, sEMG measurements were also taken on the wrist flexor (WF), wrist extensor (WE), biceps, and triceps of both arms. Significant changes were not seen in the WE (minimum P value = 0.1646), triceps (minimum P value = 0.5783), or biceps (minimum P value = 0.4034) between any of the montages and the no tDCS condition. However, a significant increase in WF AUC was seen in four subjects for A-tDCS and in six subjects for dual tDCS (Fig. 5-6). Interestingly, one of the subjects with increased WF AUC had an increase in Error (Fig. 5-5C) and the six subjects for dual tDCS all had a significant increase in RT (Fig. 5-5B).

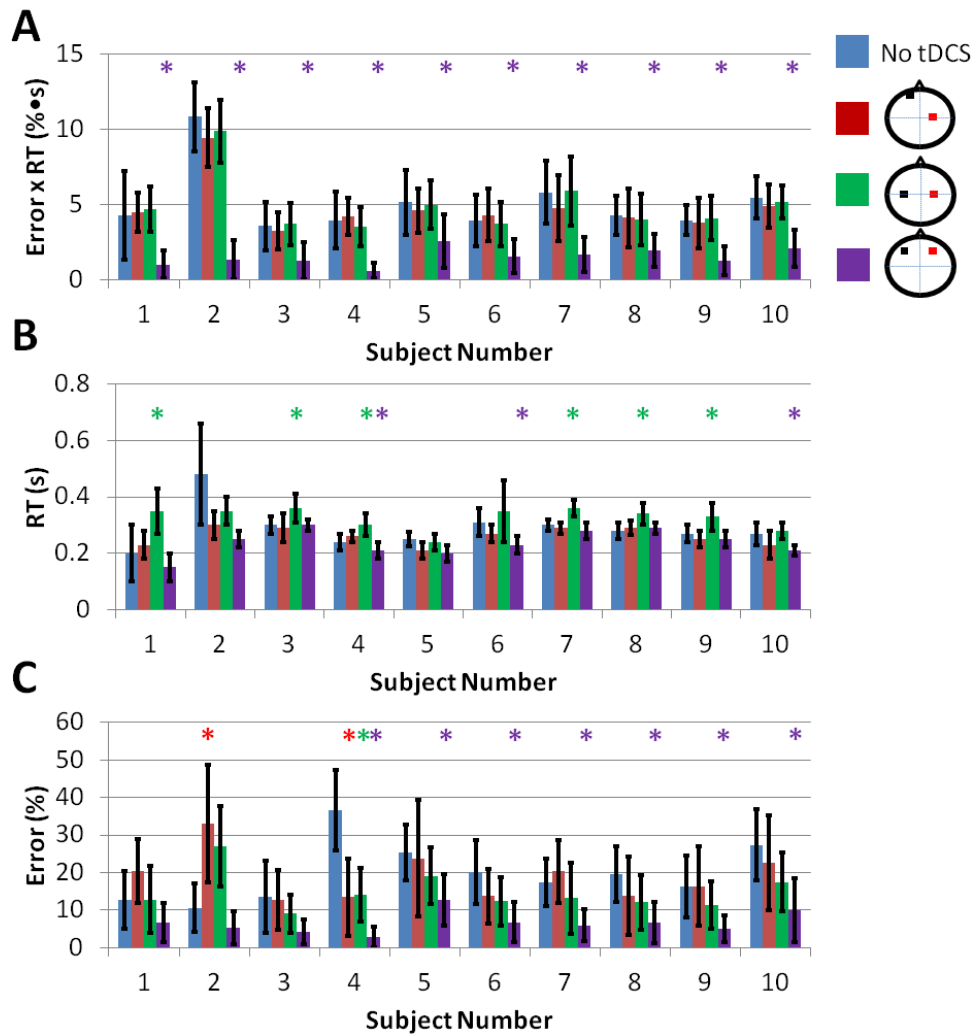


Figure 5-5 Performance analysis between the no tDCS condition (blue), A-tDCS (red), dual tDCS (green), and bi-hemispheric PMC montage (purple). Significance is represented by a color matched asterisk, where (A) presents the Error X RT product, (B) RT, and (C) Error.

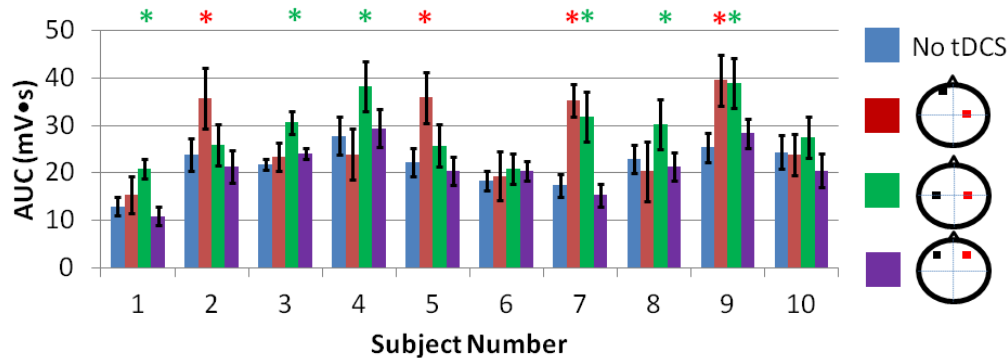


Figure 5-6 Muscle activity analysis between the no tDCS condition (blue), A-tDCS (red), dual tDCS (green), and bi-hemispheric PMC montage (purple). Significance is represented by a color matched asterisk.

5.3.5 Comparison of Montage-Specific Effects on Connectivity and Cortical Activation Between Subjects

FNIRS dAoA and LI metrics were used to measure changes in activation between conditions. At the group level, the no tDCS condition and A-tDCS had no significant differences in resting-state connectivity (Fig. 5-7A and B) or area of activation (Fig. 5-8A, P value = 0.6932). However, for the one subject with increased Error and WF AUC there was inter-hemispheric connectivity between M1 areas. Additionally, for dual tDCS there was significant inter-hemispheric connectivity at the group level with a reduction in intra-hemispheric connectivity in the ipsilateral hemisphere (Fig. 5-7C), and bilateral activity increasing the dAoA (Fig. 5-8, P value = 0.0027). Interestingly, the best montage for this group of subjects resulted in inter-hemispheric M1 and PMC connectivity (Fig. 5-7D), yet also had significant bilateral activity (Fig. 5-8B, P value = 0.0131). Importantly, other cases where there was improvement in the RT x Error product also presented bi-hemispheric connectivity between PMC areas.

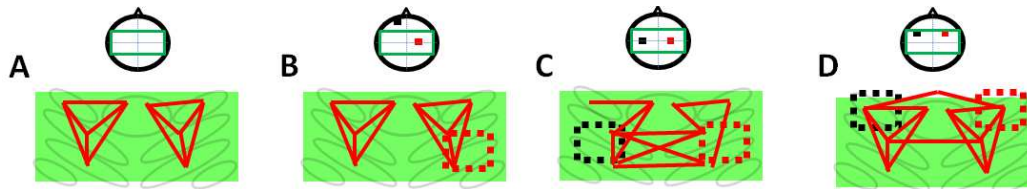


Figure 5-7 Cortical connectivity where (A) presents the connectivity before tDCS, (B) presents the connectivity during uni-hemispheric A-tDCS of the contralateral hemisphere, (C) presents the connectivity during bi-hemispheric M1 stimulation, and (D) presents the connectivity during the application of the bi-hemispheric PMC montage. The green outlined boxes represent the area over which fNIRS imaged. The black and red squares indicate the location of the cathode and anode, respectively.

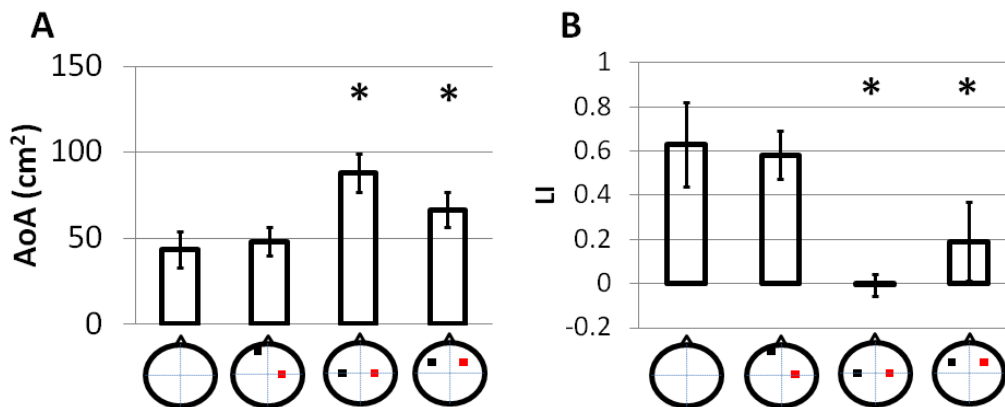


Figure 5-8 fNIRS activation metrics. (A) Area of activation (AoA) metrics over the entire fNIRS field of view, and (B) the calculated laterality index (LI).

5.3.6 Different Optimal tDCS Montages for Each Stroke Patient

Fig. 5-9 displays the ΔHbO activation maps and percent performance changes for dual tDCS and the optimal tDCS montage for each of the five stroke subjects. Each stroke subject had a different optimal montage that was not dual tDCS, except for Subject 2. Interestingly, the optimal montage brought upon a normalization in laterality of cortical activation which correlated with improvements in performance. Since RT and Error

should decrease for improved performance, those metrics with bold, red arrows pointing down indicate significant improvements. Additionally, connectivity between M1 and PMC were found for all five subjects which was not found for dual tDCS in four subjects. These stronger connections between PMC and M1 due to the optimal tDCS montage were also found in all control subjects. An example comparing connectivity in stroke Subject 1 for dual tDCS and optimal tDCS to healthy controls can be seen in Fig. 5-10.

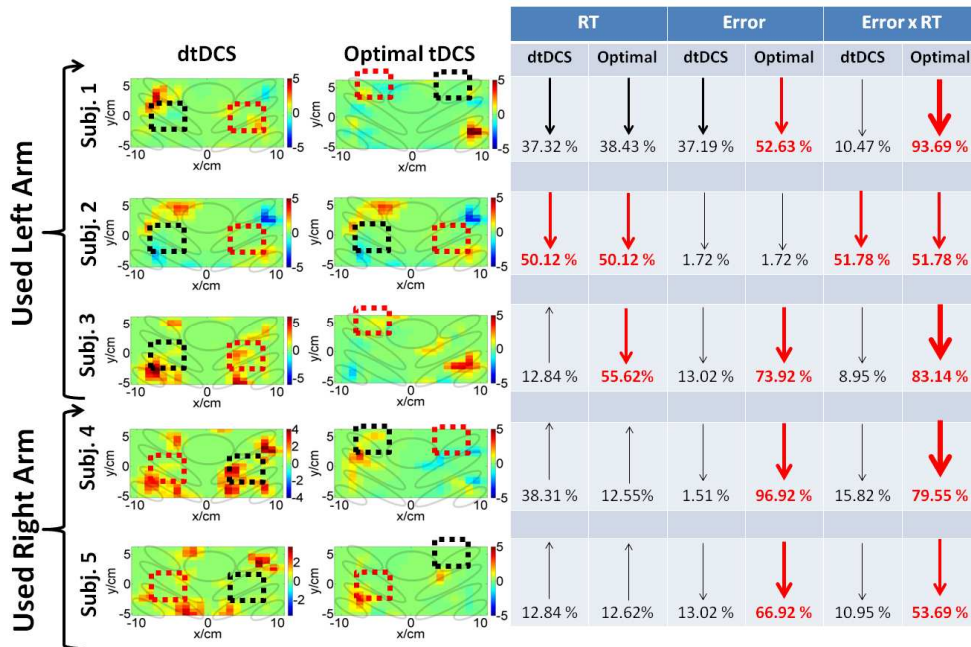


Figure 5-9 Δ HbO activation images during a wrist flexion task with concurrent application of 2 mA for dtDCS and optimal tDCS montages with corresponding task RT, Error, and Error x RT product. Performance metrics which improved significantly are indicated with a bold, red arrow pointing down.

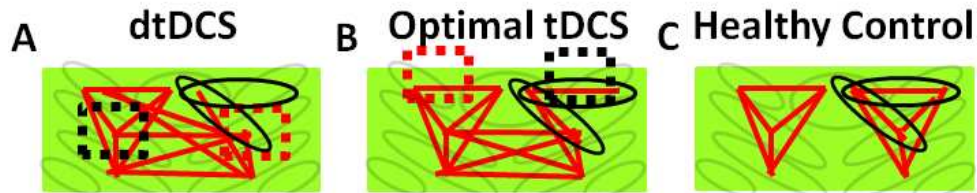


Figure 5-10 Resting state connectivity maps for a stroke patients (A) after 0.5 mA for dtDCS, (B) after 0.5 mA for optimal tDCS montage, and (C) a control without tDCS applied. The encircled connections are those connections between cortical areas that are common between the healthy control and stroke patient after optimal tDCS, but are missing from the stroke patient after dtDCS.

5.3.7 Neuromuscular Prediction

Fig. 5-11A and B show how ΔHbO (Fig. 5-11A) and WF AUC (Fig. 5-11B) increase with increased current. An important difference is the much larger increase in ΔHbO and WF AUC found due the optimal tDCS montage versus the dual tDCS montage in stroke patients for current levels including 0.5 mA, 1.0 mA, and 2.0 mA (maximum P value = 0.0409). Additionally, Fig. 5-11C presents the neural network estimation of cortical and muscular activity with measured data at 0 mA (no tDCS), 0.5 mA, 1 mA and 2 mA currents applied for 40 s for both healthy (blue lines) and stroke patients (red and black lines). As seen in Fig. 5-11C, the model closely matches the measured data with an insignificant underestimation at higher currents (minimum P value = 0.3146). Interestingly, higher changes in muscle activity are found in stroke subjects when the optimal tDCS montage is applied as opposed to dual tDCS, with the exception of one stroke subject whose optimal tDCS montage was dual tDCS. This one stroke patient was included into the optimal tDCS montage (red line), and not the dual tDCS for the neuromuscular prediction.

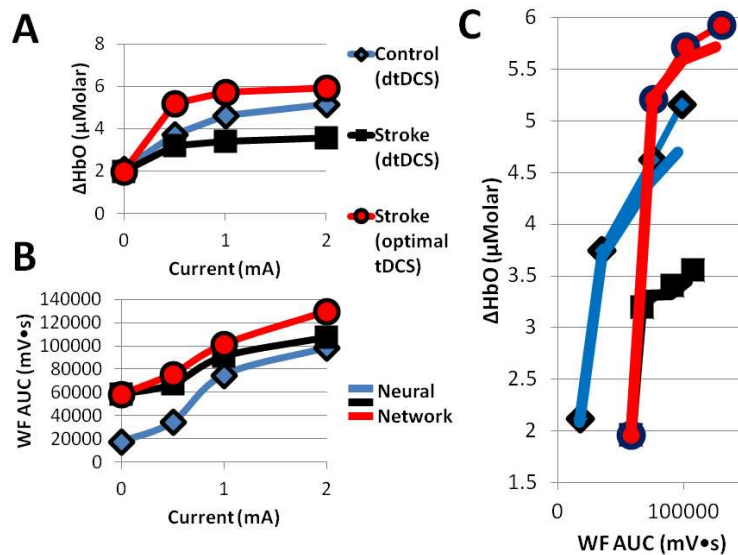


Figure 5-11 (A) ΔHbO in M1 with increase in tDCS current. (B) EMG AUC with increase in tDCS current. (C) The mapping of ΔHbO in M1 with EMG WF AUC and the NMT properly modeling this relationship.

5.4 Discussion

PtDCS was presented in this study as a novel method for quickly determining personalized tDCS electrode placement to bring about performance improvement. With this method it was possible to determine performance changes due to non-invasive cortical stimulation of 20 different tDCS montages placed over the sensorimotor cortex within a single two hour session. Interestingly, the montage that brought upon improved performance across all healthy subjects was a bi-hemispheric PMC montage (Fig. 5-2O). Additionally, the montages that gave the least improvement were the dual tDCS (Fig. 5-2M) and A-tDCS (Fig. 5-2A) montages. Further findings found that cortical connectivity had a key role in performance improvement in healthy controls (Fig. 5-7). In the end,

ptDCS excitingly found that each stroke patient had a different optimal tDCS montage for task improvement (Fig. 5-9).

5.4.1 tDCS Montage-Specific Performance Differences Between Healthy Subjects

Few studies have compared performance results between multiple montages in healthy adults (30, 34, 93, 94). However, there have been conflicting results between these studies. For example, one study presented performance improvement in dual tDCS and not A-tDCS exciting the contralateral hemisphere, while the other two presented performance improvement in both montages. Additionally, other studies which applied A-tDCS have presented improved performance in healthy adults (56, 92, 185). In contrast, this study did not show group level significant performance improvement for either montage. Similar to a previous study (56) M1 tDCS montages had better overall improvement when the ipsilateral M1 was excited. Unlike previous studies the uni-hemispheric suppression of the ipsilateral and contralateral M1 were also compared. Suppression of a cortical region is done by placing the cathode over the region of interest. However, a recent study found that application of the cathode at a current of 2 mA does not suppress, but rather excites the region under the electrode (185). This is the only study that has found these type of results. Though it is important to note, this work, as well as others, have found the cathode to still suppress at a current level equal to 2 mA. Fascinatingly, the suppression of either hemisphere was found to give the greatest performance improvement among montages that only stimulate M1. Differences between previous studies and this one may be due to the difference in tasks, since tDCS provides task-specific modulation of the cortical network. Previous studies have focused on motor learning, such as repeating a sequence of numbered keys (34) or having varying degrees of difficulty (92, 184), whereas this study had subjects place a cursor into

a single target with one degree of difficulty. Furthermore, the nature of the task in this study required larger muscle groups and more effort which may have not detected an increase of muscle activity that would have presented for a lower degree of difficulty. Many of these studies have also used similar performance metrics such as RT, Error (i.e. accuracy), or a metric that combines the two. These type of performance may improve by stimulating the motor planning centers, such as the PMC. However, no studies to date have compared stimulation of the M1 only to those that stimulate motor planning centers of the brain.

Most studies which have stimulated planning centers of the brain in healthy adults have focused on the prefrontal cortex (57). Instead, the PMC was stimulated in this study since it is a well know cortical region responsible for planning motor function. The findings of this study presented more cases of Error x RT improvement when stimulating the PMC (Table 5-3 and 5-4) than M1 (Table 5-2), demonstrating that stimulating the motor planning centers is important for bringing improvements in motor performance. Similarly, improvement in RT and accuracy were also found by applying bi-hemispheric tDCS over the prefrontal cortex (57).

Though most studies focus on the beneficial aspects of tDCS for performance improvement, it is just as important to make sure the applied stimulation does not make a person worse. A new finding in this study is the worsening of performance during tDCS. Interestingly, these cases only occur for stimulation montages which placed electrodes over only M1 or only PMC. One example is dual tDCS which increased RT for six subjects. However, montages which simultaneously stimulate the PMC and M1 presented no worsening in any subject for any performance metric. One previous study applied tDCS to both PMC and M1 simultaneously on stroke patients (186), but only reported changes in motor evoked potentials.

5.4.2 tDCS Effects on Muscle Activity in Healthy Subjects

Previous studies have looked at tDCS effects on muscle excitement separately from their effects on performance in healthy adults (60, 65). However, one study compared muscle activity during task performance, which had similar results to this study in that a significant increase in WF activity during tDCS caused a significant increase in RT, as seen in Chapter 4. Improvements due to bi-hemispheric PMC tDCS could not be explained by changes in muscle activity. This may be due to the PMC role in motor planning and not motor execution, as previous studies have not shown significant changes in muscle activity by stimulating the PMC (185).

5.4.3 tDCS Effects on Cortical Plasticity in Healthy Subjects

Explaining the effects of tDCS on task performance by functional neuroimaging has been done on many studies. Primary findings have shown increased cortical excitability due to the anode and decreased cortical excitability due to the cathode. Additionally, tDCS effects the connectivity between cortical regions. Similar to a previous study (91), this study showed that uni-hemispheric M1 A-tDCS (Fig. 5-2A) had no change in cortical connectivity (Fig. 5-7B) in this study which resulted in primarily contralateral activity (Fig. 5-8B). Like in Chapter 4 bi-hemispheric M1 tDCS (Fig. 5-2M) awoke inter-hemispheric connections (Fig. 5-7C) between the sensorimotor cortex which resulted in bilateral activity (Fig. 5-8B). The novel finding was the appearing of an inter-hemispheric connectivity between the two PMC during bi-hemispheric PMC tDCS (Fig. 5-7D), as well as other montages for a few subjects, that correlated with improved Error X RT product. This inter-hemispheric PMC connection suggests that the increased connectivity between the two PMC caused the improvement in task performance.

5.4.4 Personalizing tDCS in Stroke Patients

Studies have shown varying results in the application of tDCS in the stroke population. One recent study showed no improvement in stroke patient RT due to dual tDCS (61). However, other studies have shown improvement in stroke patient performance with the same montage (34, 54, 94). Additionally, one study made the distinction of tDCS effects based on injury location (38), which found that stroke patients with subcortical lesions improved with A-tDCS applied over the ipsilesional hemisphere, whereas stroke patients with cortical lesions did not. Together these studies indicate the need to personalize tDCS electrode placement in order to benefit stroke physical rehabilitation.

This study highlights the potential use of ptDCS for determining a personalized tDCS montage to promote performance improvement in stroke patients. Importantly, with ptDCS it was demonstrated that the best montage over the sensorimotor cortex differed for each stroke subject. Though dual tDCS and A-tDCS are common montages of choice for current rehabilitation paradigms, it was shown that this may be true in only a small percentage of the stroke population. Interestingly, for four of the five stroke patients the best motor performance improvement was found when the PMC was stimulated, further emphasizing the potential need to include motor planning centers when applying tDCS. This finding could suggest a reduction in the number of ptDCS montage combinations including only those with the PMC stimulated. However, stroke Subjects 2 and 5 did not show as large of an improvement (~ 50%) as the other three stroke patients (80% - 95%). Additionally, stroke Subject 2's best montage did not include the stimulation of the PMC. Previous studies have also shown that the application of tDCS over the prefrontal cortex has had significant improvements in RT and accuracy. This suggests that in order to find

a true optimal montage ptDCS should also be applied over different areas of the prefrontal cortex.

Finally, the predicted changes in muscle activity and cortical activity with the neural networks take into account effects that may happen at higher currents. However, these findings were found only during ptDCS and would need to be implemented along with a physical therapy regiment in the future.

5.4.5 Risks Versus Benefits of tDCS

It is also important to weigh the risks to the benefits of using tDCS for enhancing physical therapy in patients with brain injury. The potential known risks of tDCS are minor. During tDCS subjects may feel tingling (~75%), itching (~60%), slight burning sensation (~25%) (179, 206). Some subjects see flashing lights during stimulation which is normal since the electric field spread is large and can reach the occipital cortex (ref). Additionally, some side effects felt after stimulation have been fatigue (~35%), headache (~10%), nausea (~3%), and insomnia (~1%) which have been seen in a small percentage of subjects (179). Furthermore, therapeutic tDCS current densities (0.8 A/m^2) are significantly less than those which were found to cause brain damage in rats (142.9 A/m^2) (213). However, long-term exposure may lead to overheating of the brain tissue and tissue damage. Charge exposure of $85,000 \text{ C/m}^2$ resulted in brain damage in rats (213), however therapeutic tDCS in humans has a charge exposure of 960 C/m^2 which is significantly smaller and does not cause damage to human brain tissue or anatomical alterations to the blood-brain barrier (214). However, long-term effects of continuous use of tDCS have not been studied. Since the risks of tDCS are mainly temporary discomforts, the potential life changing motor performance benefits gained with combining tDCS with physical therapy easily outweigh the short-term risks.

5.4.6 tDCS Limitations

There are a few limitations in the ptDCS method. For example application of tDCS with large electrodes (25 cm^2) results in a large spread in the electric field and current density across the scalp and cortical surface which can result in unintended stimulation of non-targeted cortical areas. Previous studies have found that rectangular electrodes have the highest current density at the edges of the electrodes on the scalp surface (215). Importantly, ~40% of the current was found to be shunted by the scalp, skull and cerebral spinal fluid before reaching the cortex (216). When electrodes were placed on both hemispheres over the primary motor cortex the full-width half maximum of the current density and electric field spread covers $\sim 100 \text{ cm}^2$ of the cortical surface and reaches to the prefrontal and occipital cortical areas (216). Furthermore, the maximum electric field magnitude (0.3 - 0.4 V/m) and current density ($0.04 - 0.07 \text{ A/m}^2$) was not found underneath each electrode, but between the two electrodes (216-219).

Since no anatomical MRI images were taken to determine proper placement of the electrodes in this study, the large electric field spread using large electrodes in this study gave 1 cm placement error margin which has shown to only have a 4% effect on the electric field and current density (220). Without an MRI to guide tDCS electrode placement, smaller 1 cm^2 electrodes would have had a 20% decrease in the current density at the cortical region of interest if it was misplaced by 1 cm. Thus, it was better to use larger electrodes in order to confidently stimulate the region of interest. However, the drawback was that surrounding, non-targeted cortical areas may have also been affected by the stimulation.

In order to focus the electric field and current to the cortical area of interest, it has been shown to be advantageous to use smaller, ring shaped electrodes (217, 221). By decreasing the electrode size to 1 cm^2 the stimulated area can be focused to 10 cm^2

(216). Focusing the stimulation area can increase muscle output as was seen in a previous study that found larger MEP with smaller 12 cm² than with larger 24 cm² and 35 cm² electrodes (221). Unfortunately, using smaller electrodes with the same current density for a larger electrode results in a smaller current density in the target area (215). Thus, the current would need to be increased when using smaller electrodes. Additionally, the depth at which the electric field spreads is dependent on the inter-electrode distance (216, 217). Electrodes placed close to each other have a large amount of current shunt through the scalp. For example, electrodes placed within 8 cm of each other have 60 - 65 % of the current shunted by the scalp, skull, and cerebral spinal fluid, as opposed to ~40% when the electrodes are placed 15 cm apart. Recently, a 4 x 1 ring electrode montage has been studied over M1 which can reduce the cortical stimulation area of the motor cortex to ~10 cm² without large amounts of shunting from the surface tissue (219) (222). This montage bases the electrode placement on the EEG 10/10 system in which a 1 cm² anode electrode is placed over the C3 position and four 1 cm² cathode electrodes are placed around the anode, like a ring, at the FC5, FC1, CP5, and CP1 locations. However, this montage is focused on only stimulating one region of the cortex, and would need to be extended in order to excite and suppress multiple regions.

In the future, it will better to use MRI to guide the placement of tDCS electrodes with higher precision which will give the ability to use smaller 1 cm² ring electrodes. This will reduce any accidental stimulation of non-targeted cortical regions and focus the stimulation on the regions of interest, thereby increasing the effects of the stimulation on muscle output and performance.

Chapter 6

Conclusions and Future Work

The goal of this work was to improve fNIRS measurements and combine them with multi-motor recording and a non-invasive cortical stimulation method known as tDCS as a first step towards enabling the future personalization of tDCS-based treatment in persons with brain injury such as stroke patients. The outcome of this research was the development of a novel method that we call ptDCS, which was shown to improve task-specific performance during and immediately after stimulation in healthy adult controls and stroke patients. The resulting findings showcase the very significant future potential of ptDCS as a means of personalizing the treatment of brain injury. This steps performed to materialize the goal of this work are outlined in the paragraphs below.

The first part of this study presented an improvement in fNIRS measurement success by a novel brush optode which was developed to overcome the common problem of hair obstruction. The important contribution that brush optodes bring is the increased SNR for all hair colors and densities making it possible to measure individuals with dark and dense hair who were immeasurable with commercial flat optodes. The intention was to use these brush optodes in all subsequent human subject measurements, but that was not done because the issue of reduced comfort, due to an increased level of scalp poking by the individual brush fibers, was not resolved.

The second part of this study then established simultaneous fNIRS, muscle and performance measures as a method of relating cortical plasticity to changes in muscle activity and performance during and after the application of tDCS. Both possible bi-hemispheric M1 montages were used to test this method. For both montages inter-hemispheric connectivity resulted in increased bilateral cortical activity during tDCS. Interesting findings were the inter-hemispheric connectivity resulting in increased bilateral

activity and wrist flexion speed due to the post-suppression of the contralateral hemisphere with respect to the arm used. On the other hand, excitation of the contralateral hemisphere resulted in intra-hemispheric connectivity to appear and improved accuracy of the motions performed post-tDCS. Importantly, this part of the study displayed that the combination of fNIRS, sEMG, and performance measures could be used to guide tDCS therapy.

The last part of this study presented an exciting new method to personalize tDCS electrode placement with the use of the previously established concurrent measurements of fNIRS, sEMG, and task performance. The need for this type of paradigm was encouraged by a recent finding of tDCS differences between stroke patients due to injury location and conflicting tDCS-induced performance changes found between studies for stroke patients and healthy adults. This new method that we call ptDCS reduced the applied tDCS time and current (dose) to only transiently perturb the cortical network, muscle activity, and performance, yet return them back to their pre-tDCS induced state within a three minute period. This shortening of tDCS effects allowed for applying up to 20 different tDCS electrode montages over the sensorimotor cortex within a two hour session. Important results found by ptDCS include: 1) large between-subject variability for each tDCS electrode montage, 2) a bi-hemispheric PMC tDCS montage produced better performance improvements than dual tDCS or A-tDCS in healthy adults with the latter two being the standard electrode montages reported in current literature, 3) there were few cases in which dual tDCS and A-tDCS significantly worsened performance in healthy adults, and 4) optimal electrode placement was not found to be dual tDCS or A-tDCS for 4/5 stroke patients in this study.

In the future, ptDCS could be further optimized. For example, ptDCS could be expanded to include other planning centers of the brain such as the prefrontal cortex or

the supplementary motor area. Additionally, the electrode size and current density could be optimized before applying ptDCS by tDCS simulations on a subject's magnetic resonance image (MRI). Furthermore, electrode positions could be optimized to focus stimulation to specific cortical regions of interest. Also, ptDCS is a task-specific method which can be applied for the optimization of performance for different motor tasks, even sequentially for the same subject. Lastly, ptDCS can potentially be applied on other categories of brain injury patients such as cerebral palsy or traumatic brain injury. All in all the breakthrough of this work is that it proposes a method that may be generalized to a wide variety of therapy personalization paradigms. It is hoped that ptDCS will be adopted and tested in the future by other investigators so that its full potential for treatment guidance and human performance improvement can be explored.

Appendix A

Spatiotemporal Relations of Primary Sensorimotor and Secondary Motor Activation

Patterns Mapped by FNIR Imaging

A.1 Introduction

Functional near infrared (fNIR) spectroscopy detects changes in light absorption and scattering in tissue caused by changes in concentration of oxyhemoglobin (HbO) and deoxyhemoglobin (Hb) secondary to neuronal activity, occurring through neurovascular coupling mechanisms that are still under investigation (99). With the use of multiple source-detector pairs over a specified field of view (FOV), images can be reconstructed by mapping the detected signals to the Green's solution of the linearized perturbation diffusion model for tissue-light interactions (98, 223). This method is referred to as fNIR imaging. Though only being able to image hemodynamic activity in the cortex, its portability and lower cost compared to established radiological imaging modalities have motivated its use for the monitoring of a wide range of neurological conditions (115, 116, 125, 127, 224-226). Of increasing interest in recent years has been the use of fNIR imaging to monitor cortical plasticity in response to motor skill rehabilitation (125, 225) as an alternative technology to functional magnetic resonance imaging (fMRI) (227-230). Though fNIR imaging has lower spatial resolution compared to fMRI, it can detect hemodynamic change patterns with higher sensitivity and temporal resolution (100, 102), and enables researchers to perform longitudinal studies more easily. Additionally, fMRI requires subjects to be immobilized, since it is sensitive to motion artifacts (95, 123, 231), whereas fNIR imaging is relatively robust to motion artifacts allowing subjects to perform a larger range of motions (95, 231) and thus offers more ways to probe sensorimotor cortex function.

These promising features of fNIR spectroscopy technology are tempered by the limited number of source-detector pairs that current brain imaging systems can accommodate. This limitation constrains users to either measure sparse activation data over a large area over the cortex that result in no images (134), or in low resolution images (114, 232, 233), or perform high resolution imaging studies over a limited FOV size (122). More specifically, in a previous study a large FOV of 13 x 13 cm was used to image the primary motor cortex (M1), primary sensory cortex (S1), premotor cortex (PMC), and supplementary motor area (SMA) of both

hemispheres during the learning of a rotary arm movement (232). The minimum source-detector distance was 3 cm, and the spatial resolution of this study was limited due to the sparse source-detector geometry. Other studies with similar source-detector separations, but with smaller FOVs (6 x 6 cm, 3.75 x 2.5 cm, and 5.6 x 8.4 cm) focusing on M1 and S1, have been reported to image cortical activation due to finger tapping, forceful pinching, sequential tapping, and palm squeezing protocols (114, 175, 234). In an attempt to further improve spatial resolution, a study limiting its FOV to 3.75 x 3.00 cm used bifurcated fibers separated by 0.75 cm to image cortical activity of finger tapping and vibrotactile stimulation of individual fingers (122). Though in most activation studies only the function of the S1 and M1 cortices are probed by finger tapping (99, 100, 175, 234-236), palm squeezing (237), and vibrotactile stimulation (122), other surrounding cortical regions contributing to the planning and execution of motions are left outside of the chosen FOV.

In this work we used an array of bifurcated source-detector fiber bundles to image cortical activation over a FOV, spanning the PMC/SMA, M1, S1, and posterior parietal cortex (PPC) of a single brain hemisphere. Cortical activity was caused by finger tapping, tactile stimulation, squeezing of a stress ball (palm squeezing), sequential finger tapping, and card flipping (supination and pronation). This work presents, to our knowledge for the first time, fNIR images over an extended FOV (12 x 8.4 cm) in a single brain hemisphere for a number of different hand and arm motion activation protocols. The unique spatiotemporal relation of the PMC/SMA, M1, S1, and PPC activation patterns for each type of movement is demonstrated. We also demonstrate that all activation patterns can be measured without motion artifacts and reproducibly. In addition, application of a cluster component analysis (CCA) algorithm (238) to these fNIR signals shows that depending on the motor task different cortical regions share similar temporal activation patterns. Though these results are limited to one side of the brain due to the limited number of source-detector fibers available, they showcase the rich information that can be obtained from spatiotemporal activation patterns when a larger cortical

area is imaged. Importantly, these results provide a paradigm for exploring the function of the secondary motor, M1, S1, and PPC simultaneously, which may be a useful tool for future use in rehabilitation response monitoring and other clinical applications of fNIR imaging.

A.2 Methods and Materials

A.2.1 Subjects

Three right handed subjects were included in this study (one female and two male, 25 ± 3 years old). For each subject one repeat session was performed 3 to 4 weeks from the first visit to test the reproducibility of cortical activation in the same FOV. These studies were performed under the approval of The University of Texas at Arlington (UTA) Institutional Review Board protocol (IRB No.: 2011-0193).

A.2.2 Measurements

A continuous wave fNIR spectroscopy brain imager (DYNOT, NIRx Medical Technologies, LLC., Glen Head, New York) was used to map the HbO and Hb changes due to cortical activity induced by block design hand and arm motion protocols performed sequentially, as described below. In this brain imaging system, two wavelengths (760 nm and 830 nm) were simultaneously provided by two laser diodes, whose light was coupled sequentially into a maximum of 32 different fiber bundles that delivered the light to user-selected positions on the subject's scalp. Each fiber bundle was given an equal interval of illumination time, the duration of which was determined by the number of source-detector pairs that the system had to cycle through (time-multiplexing). Though only one source was on at any one time, the intensity from each source was sine-wave modulated at a frequency in the 4 – 11 kHz range as a means of tagging its identity. Each of the fiber bundles touching the scalp's surface was bifurcated, thus allowing each to act as both source and detector. Since the weight of the fibers, in the absence

of any external support, caused discomfort to the subjects a stand was constructed to support part of the weight of each fiber bundle. With this stand in place only the length needed to adjust

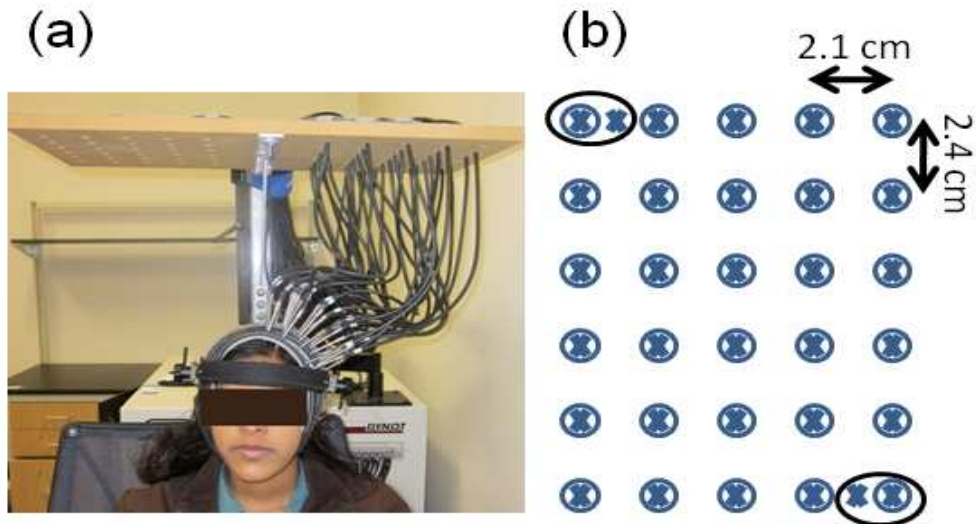


Figure A-0-1 (a) The stand constructed to relieve the subjects from supporting the entire weight of the fibers. In addition, a soft yet sturdy holder was made to hold the fibers in place on top of the subject's head with good optical contact. (b) Bifurcated fiber bundle source-detector geometry where the 'X' symbols are detectors, and the 'O' symbols are sources, covering a 12 x 8.4 cm FOV. The encircled areas (black ovals) indicate the short distance source-detector pairs used to detect scalp hemodynamics.

the position and angle of the fibers on the head surface was left to be supported by the subject's head [Fig. A-1(a)]. The probe stand consisted of two wooden planks, a fixed metal column, and an adjustable metal column. One of the wooden planks was placed at the base to support the balance of the entire stand assembly, and the other plank was placed at the top of the metal column to support the weight of the fiber bundles. The fixed metal column was a metal mailbox stand and the adjustable metal column was used to change the height of the wooden fiber bundle support plank as some subjects were taller than others. Additionally, a wearable probe

holder was made to maintain the fiber bundles in a fixed position onto the scalp during fNIR measurements. The probe holder was created in layers that were glued together. The outer layer was made of vinyl rubber, the middle was Buna rubber, and the lower layer was self-adhesive foam. The vinyl rubber was used for its rigidity and the Buna rubber for its flexibility so that their combination kept the probes pointing straight onto the scalp with the entire assembly following the head's curvature. The foam layer that was glued onto one side of the composite rubber layers was in contact with the head's surface so as to keep the subjects comfortable. Finally, a plastic adjustable headband, originally intended to hold a welder's mask, was used to keep the probe holder in place onto the subject's head. The geometrical positioning of the probes fit a 12 x 8.4 cm FOV, in which the probes were placed 2.1 cm apart laterally and 2.4 cm apart in the anterior-posterior direction [Fig. A-1(b)]. This geometry enabled measurements from source-detector distances of 2.1 cm, 2.4 cm, and 3.2 cm, totaling in 178 source-detector pairs. Since the sampling rate decreased with an increasing number of source-detector combinations due to the increased time multiplexing, the fNIR spectroscopy signals could be sampled at 1.81 Hz for the chosen source-detector arrangement. Two additional measurements were also taken at the corners of the FOV, with a source-detector separation of 1.1 cm [encircled in Fig. A-1(b)]. These additional measurements were used to measure the respiration and Mayer wave hemodynamics, in order to subsequently filter these out of the activation signals (138, 145, 239, 240).

A.2.3 Activation Protocols

The fNIR spectroscopy probe placement was done according to the measured coronal (ear-to-ear) and sagittal (nasion-to-inion) distances. The midpoint of the right edge of the probe set was placed at the intersection of the aforementioned measurements, while parallel to the sagittal line. This way the entire assembly would cover the PMC/SMA, M1, S1 and PPC areas of one hemisphere of the brain. Since all tasks were performed with the dominant hand (right

hand) the probe assembly was placed over the brain hemisphere contralateral (left hemisphere) to the hand and arm performing the movements indicated by the activation protocols. The subjects sat up straight with their head resting back in a quiet, dimly lit room. A PowerPoint animation on a computer screen guided subjects through the protocols. The data acquisition paradigm consisted of a 30 s baseline (no stimulation), immediately followed by a series of ten consecutive epochs of 15 s of stimulation and 25 s of rest, and ended with a 20 s baseline measurement, resulting in a total acquisition time of 450 s. Data was acquired for each subject for five consecutive periods lasting 450 s each, with one of five different activation protocols being executed each time. Four protocols requiring movement were finger tapping, palm squeezing, sequential finger tapping, and card flipping (supination and pronation). Finger tapping consisted of the subject repeatedly tapping with all fingers and the palm squeezing protocol consisted of the subject repeatedly forming a fist by squeezing a stress ball. For sequential tapping, the index finger, middle finger, ring finger, and pinky were correspondingly numbered from 1 to 4. The PowerPoint animation presented the numbers in a random order, as determined by a random number generator in MATLAB (Mathworks, Natick, Massachusetts), during the stimulation portion of the protocol. The last activation protocol was a card flipping task in which the subject was asked to flip individual cards from one deck to a separate deck of cards. The two decks were placed apart by a distance equal to the subject's shoulder width and subjects took a card from the left deck and flipped it as they placed it onto the right deck. Importantly, during card flipping subjects were looking at the computer screen, not at the deck of cards, and therefore had to rely on hand sensory input to perform this task. Additionally, a protocol in which the bristle of a toothbrush was rubbed across the tips of the index, middle, and ring fingers was also performed without any concurrent hand movements to locate S1. No set stimulation frequency was required of the subjects. Thus, all motions were self-paced and were in the 1-2 Hz range for each protocol.

A.2.4 fNIR Signal Filtering

In addition to detecting evoked hemodynamic changes, fNIR spectroscopy is sensitive to cerebral hemodynamic fluctuations of systemic origin. Such systemic fluctuations can be caused by cardiac pulsation, respiration, and Mayer waves (100, 239, 241). For typical motor activation protocols, the cortical hemodynamic response can be found in the 0.01–0.4 Hz frequency range, while physiological artifacts, such as cardiac pulsation, can be found between 0.8–2.0 Hz, respiration in the 0.1–0.3 Hz range, and Mayer waves at ~0.1 Hz or lower (100, 241, 242). Because there is a significant overlap between the frequency spectra of respiration and Mayer waves and of the hemodynamic response due to brain activity, band-pass filtering is not effective in removing such physiological artifacts. Recent studies have used component analysis (138, 241, 243, 244), adaptive filtering (138, 145, 239, 240), or a combination (125, 138) to remove physiological artifacts.

This study used a combination of band-pass filtering, adaptive filtering, and component analysis to filter the fNIR signals (125). The first step in the signal filtering was to band-pass filter fNIR signals from all source-detector separations, including two short-distance reference hemodynamics measurements [encircled in Fig. A-1(b)], in the 0.01 and 0.4 Hz range as this frequency window was found to contain the power spectrum of activation signals as well as that of respiration and Mayer waves. Cardiac pulsation, which was in the 1 Hz, range was filtered out of this window though some signal aliasing is possible due to the low sampling rate in this study (1.81 Hz). Subsequently, a combination of an adaptive least mean square (LMS) filter and principal component analysis (PCA) was used to filter the band-pass filtered fNIR signals (125). The physiological hemodynamics reference measurement at the top left FOV was used as the adaptive filter reference for the top half of the optodes shown in Fig. A-1(b) and the hemodynamics reference measurement at the bottom right FOV was used for the bottom half of this optode arrangement.

A.2.5 Data Pruning - A Method for the Elimination of Noisy fNIR Channels

Though the fiber bundles for fNIR measurements were placed on the head with good stability, hair still played a significant role in obstructing these fiber bundles from obtaining good optical contact with the scalp. Including fNIR data from fibers with poor optical contact into the analysis resulted in significant additional noise propagating into the resulting reconstructed images. Therefore a method to remove low signal-to-noise ratio (SNR) pairs was needed. In sparse source-detector arrangements data from such detector fibers can be removed after visual inspection of their time-series signals. Since a large number of source-detector pairs was involved in this work a quantitative automated method, somewhat akin to the jackknife method (245), was developed to identify and remove, or 'prune' the noisy detector channels, as described in more detail here below.

The flowchart of the algorithm used to identify the source-detector pairs with low SNR after filtering is shown in Fig. A-2(a). Firstly, SNR values for all source-detector pairs were determined by Eq (A-1):

$$SNR_{s,d} = 10 \times \log(P_{s,d} / P_d) \quad (\text{A-1})$$

where $SNR_{s,d}$ was the SNR value for a specific source-detector pair, $P_{s,d}$ was the power within the 0.01 Hz to 0.4 Hz frequency range for a specific source-detector pair after being filtered, and P_d was the power within the same frequency range for a dark measurement (no light source on) with the specific detector. As SNR was dependent on detected light intensity, which in turn depended on source-detector separation, comparisons of SNR were first performed within groups of the same source-detector separation. Three groups were thus formed corresponding to 2.1 cm, 2.4 cm, and 3.2 cm source-detector separations. In each group SNR values were ordered from least to greatest and an iterative procedure was applied, the first step of which was to remove the smallest SNR value of the group creating a pruned group. Subsequently, a comparison was made between the mean and standard deviation of this

pruned group and the corresponding values in the original, non-pruned group. These pair-wise comparisons between groups were performed by using the T-test and F-test, respectively. If a significant difference was not found ($p > 0.05$) for either a change in the mean or standard deviation of the pruned group, the lowest SNR value was discarded and the process was repeated for the detector signal with the next smallest SNR value in that group. The first SNR value that, when removed, caused a statistically significant change in either the mean or the standard deviation of the remaining group members was chosen as the noise threshold for that group. Once the SNR threshold values for each of the three source-detector separation groups were determined, the global SNR threshold was set as the minimum of the three group threshold values. Detectors at all three source-detector separations below this global threshold were excluded from further analysis. Selection of a minimum global threshold was empirically found to reject detectors with SNR values significantly lower than the mean SNR of all source-detector pairs in the FOV. The average SNR for this study was 27.33 ± 18.12 dB, while the SNR threshold was found to be 5.32 ± 0.64 dB and the number of source-detector pairs removed was 13.17 ± 7.35 out of a total 178. After pruning, the remaining data was further processed for signal visualization and image reconstruction.

A.2.6 Visualization of fNIR Images and Spatiotemporal Clustering of Activation Regions

Reconstruction and visualization of fNIR activation images resulting from the acquired reflectance data that passed the SNR selection criteria outlined above was performed by the open-source HomER software implemented in MATLAB (246). In this software activation images were reconstructed by use of the Tikhonov perturbation solution to the photon diffusion equation (142, 143), which employed a regularized Moore–Penrose inversion scheme (142, 143). The reconstructed, two-dimensional images (21 x 21 pixels) represented maps of Hb and HbO changes on the cortical surface, within the detector's FOV [Fig. A-1(b)]. Furthermore, 40-s rest-activation intervals were removed from the analysis of all channels if motion artifacts were

detected within a rest-activation interval. Motion artifacts were determined by spikes that were more than three standard deviations above the mean of the rest-activation intervals (244). If a 40-s rest-activation interval was removed, the two adjacent rest-activation intervals were concatenated together to form again a continuous time signal for each pixel. Images were then reconstructed for every 0.55 s time interval and time-averaged images of activation were created [Fig. A-2(b), panel (1)] by averaging all images in the interval between 5 s and 20 s after the beginning of each activation protocol, as these times presented activation that was visually discernible over baseline values for all protocols presented in this work.

After the fNIR images were reconstructed, regions of activation were determined by a T-test in an approach similar to that used in fMRI image analysis (247). Areas of activation were identified by comparing, for the time-series of each pixel, the mean and standard deviation of the changes in HbO and Hb during the activation period (5 s to 20 s) relative to changes in baseline values acquired just prior to activation (-10 s to 0 s). After considering Bonferroni's correction for multiple comparisons (146), pixels in reconstructed images were considered to have significant activation when $p < 0.0001$, and color-coded T-value maps were plotted [Fig. A-2(b), panel (2)]. The resulting T-value maps showed that the activation areas expanded further than what was seen from the time-averaged activation images.

Once activation regions were identified it was subsequently investigated if there were cases where spatially distinct sub-regions had similar time-series activation profiles for the different hand and arm motions performed in each activation protocol. To that end, the time-series pattern of fNIR signals with significant activation ($p < 0.0001$) were decomposed into a signal harmonic subspace and then clustered into source-detector pairs with similar harmonic content using a cluster component analysis (CCA) algorithm (238). The details of how this algorithm was applied to this study are described in the Appendix. CCA grouped the source-detector pairs with similar temporal patterns into clusters that were displayed as connected circles having a different color for each cluster [Fig. A-2(b), panel (3)]. In that panel the grey

circles indicate the location of bifurcated source-detector fibers with no significant activation as determined by the above mentioned T-test.

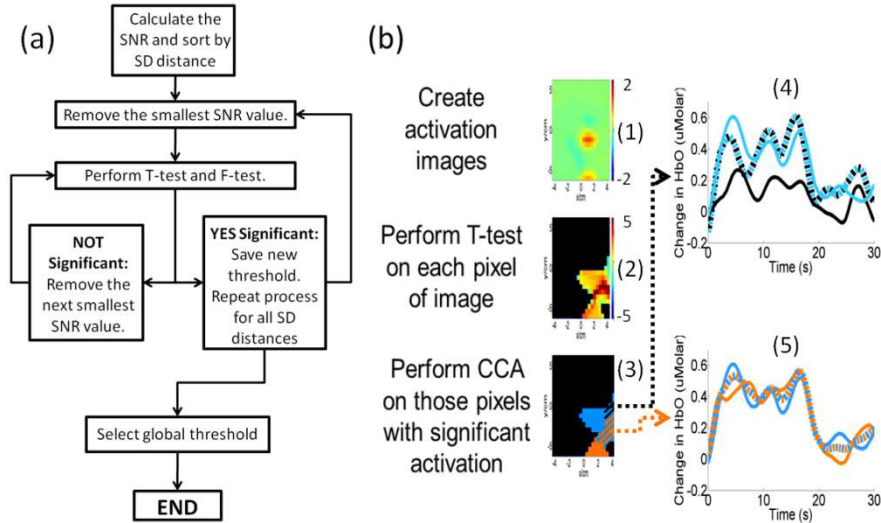


Figure A-0-2 (a) A flowchart of the algorithm used to remove source-detector pairs with low SNR due to poor optical contact. (b) In time-averaged activation images produced with data from the remaining source-detector pairs [panel (1)], pixel-wise T-tests were performed with corresponding baseline values to identify regions of activation [panel (2)], which were subsequently clustered according to their similarity in temporal activation patterns [panel (3); S1/PPC orange, M1 blue, background black]. Some clusters were the result of the superposition of activation and background hemodynamics [black and blue striped area in panel (3)], or the superposition of two separate activation areas [blue and orange striped area in panel (3)]. Panel (4) shows cluster-averaged time-series data for activation in the M1 region (solid blue curve), the background region (solid black curve) and the region of overlap (dashed black and blue curve). Panel (5) shows the corresponding color-coordinated time-series data for the M1 (solid blue curve), S1/PPC regions (solid orange curve) and their overlap (dashed orange and blue curve).

It should be noted that due to the diffuse light scattering occurring for fNIR spectroscopy signals a detector channel can see activation changes from multiple spatial locations, which can

result in some fiber locations being assigned to more than one cluster. Nevertheless, it was found that CCA showed little overlap between different source-detector pair clusters. For example, for a palm squeezing task in Subject 2 there was overlap for only a single source/detector fiber location [Fig. A-2(b), panel (3), right edge]. An example of the difference in time-series profiles between different source-detector clusters is shown in Fig. A-2, panel (4). Finally, it is important to mention that, in conjunction with CCA, it is critical to use the fNIR signal filtering procedure described in Section 2.4 above to avoid clustering errors due to activation signal contamination from large amplitude physiological hemodynamics.

A.2.7 Spatial and Temporal Metrics

After creating the activation images and determining the regions of activation, spatial and temporal metrics were used to quantify the repeatability of the location and temporal pattern of the hemodynamic response for each protocol. These metrics were applied to those pixels in the activation images which were considered significantly active by the T-test ($p < 0.01$) where the spatial metric, the center of mass of the activation area, was applied to the time-averaged images and the temporal metrics, time-to-peak (TtP) and duration of activation, were applied to the time-series images. The center of mass for the activation area was determined separately for the x- and y-directions, and was defined by Eq. (A-2), where CoM is the center of mass, $w_{x,y}$ is the change in HbO for a pixel, and d is the distance of a pixel from the left edge of the FOV for the x-direction or the distance from the FOV bottom for the y-direction.

$$CoM = \sum_X \sum_Y w_{x,y} \cdot d_{x,y} \quad (\text{A-2})$$

Additionally, analyzing the time-series images the TtP was defined as the difference between the beginning of the activation interval and the time point of maximum HbO change (188). Determining the duration was more computationally expensive, in which the time-series of each pixel were first placed into a matrix where the rows were the pixels and the columns were pixel values at each 0.55 s time point. Then a k-means clustering algorithm (188) was

applied to divide the time-series pixels into activation, baseline, and deactivation. The duration was then found to be the amount of time a pixel was found to have activation (188).

A.2.8 Statistical Analysis

All statistical tests were performed, using SAS 9.1 (SAS Institute Inc., Cary, North Carolina) to see if there was a significant difference ($p < 0.05$) between visits or between groups. One-sampled T-tests were performed to see if there was a difference in spatial and temporal metric means between visits. The null hypothesis was defined as a zero difference in the means between the two visits. After source-detector pairs were clustered with CCA, the temporal metrics, TtP and duration, were compared between clusters for sequential finger tapping and card flipping using a two-sampled T-test. Furthermore, the frequency that a given cluster was assigned to each source-detector pair was tested across motion tasks using the Fisher's exact test. The analysis was first applied for all tasks as a group, and then applied as a post-hoc analysis to compare each possible pair of tasks.

A.3 Results and Discussion

A.3.1 Analysis of Time-Averaged Activation Images

For each of the five activation protocols performed by each subject the detector signal intensities for the properly executed (no motion artifacts) 40-s stimulation-rest intervals of each source-detector pair retained after data pruning were time-averaged for each 0.55 s time point (a total of 72 time points). Activation images over the measured FOV were then reconstructed for every time point from the averaged temporal response of all kept source-detector pairs (248). The resulting images were used to determine spatial locations and temporal patterns of the hemodynamic response due to each protocol, and their repeatability between visits.

In Fig. 3, time-averaged images for the 5 s to 20 s interval are shown for each task, for both visits of each subject. From these images the locations of activation were visually identified

for each protocol, and were seen to be repeatable for each subject where the center of mass of the activation area within a cortical region between visits was not significantly different in either the x-direction (0.47 ± 0.88 cm, $p = 0.39$) or the y-direction (0.64 ± 0.94 cm, $p = 0.31$). The probe placement accuracy between repeat sessions was ~ 3 mm in the x- and y-directions, as estimated from sagittal and coronal measurements done for the probe placement procedures described in the Methods Section. Though the true locations of cortical regions activated by the protocols used in this work were not validated by concurrent fMRI imaging the approximate anterior-posterior location of the PMC/SMA, M1, S1, and PPC regions were estimated by comparison of previously reported MRI and fMRI studies with fNIR imaging results obtained from the finger tapping and sensory stimulation protocols. More specifically, the placement of the dividing line separating S1 from M1 in Fig. 3 was made under the assumption that these cortical regions were each ~ 2 cm in width in the anterior-posterior direction, as MRI images have shown for the adult human cortex (189, 249, 250). Also, as was found in previous fMRI studies, finger tapping elicits activation in the M1 and S1 cortical regions (102, 181, 182, 251), and sensory stimulation by the bristle end of a toothbrush results in activation of the S1 and PPC regions (122, 181, 252, 253). Activation in the corresponding regions was seen with fNIR imaging (Fig. A-3, rows 1 and 2), though the activation of the PPC during finger tapping is not seen. Nevertheless, T-value maps of the fNIR data did show that there was significant activation ($p < 0.01$) in the PPC (Fig. A-4, column 1).

A.3.2 Analysis of Time-Series Activation Images

A.3.2.1 Quantification of Temporal Metrics

In addition to identifying the spatial location of activation areas, fNIR imaging also enables investigation of the temporal dynamics of each cortical region due to the different activation protocols. Fig. 4 shows the evolution of activation patterns for each protocol, in time-averaged 5 s blocks for the first 30 s for Subject 1. Similar patterns were found for the other two

subjects (time-series images not shown) and were repeatable between the two imaging sessions for all subjects. In order to make some quantitative comparisons between temporal activation patterns, the TtP and duration of activation elicited by each protocol in each spatially distinct activation region was quantified as described in the Methods Section. The TtP (1.17 ± 2.38 s) and duration (1.36 ± 2.97 s) difference between visits for each protocol of each subject were not found to be significant ($p > 0.05$). The corresponding results for TtP are shown in Table 1 and for duration in Table 2.

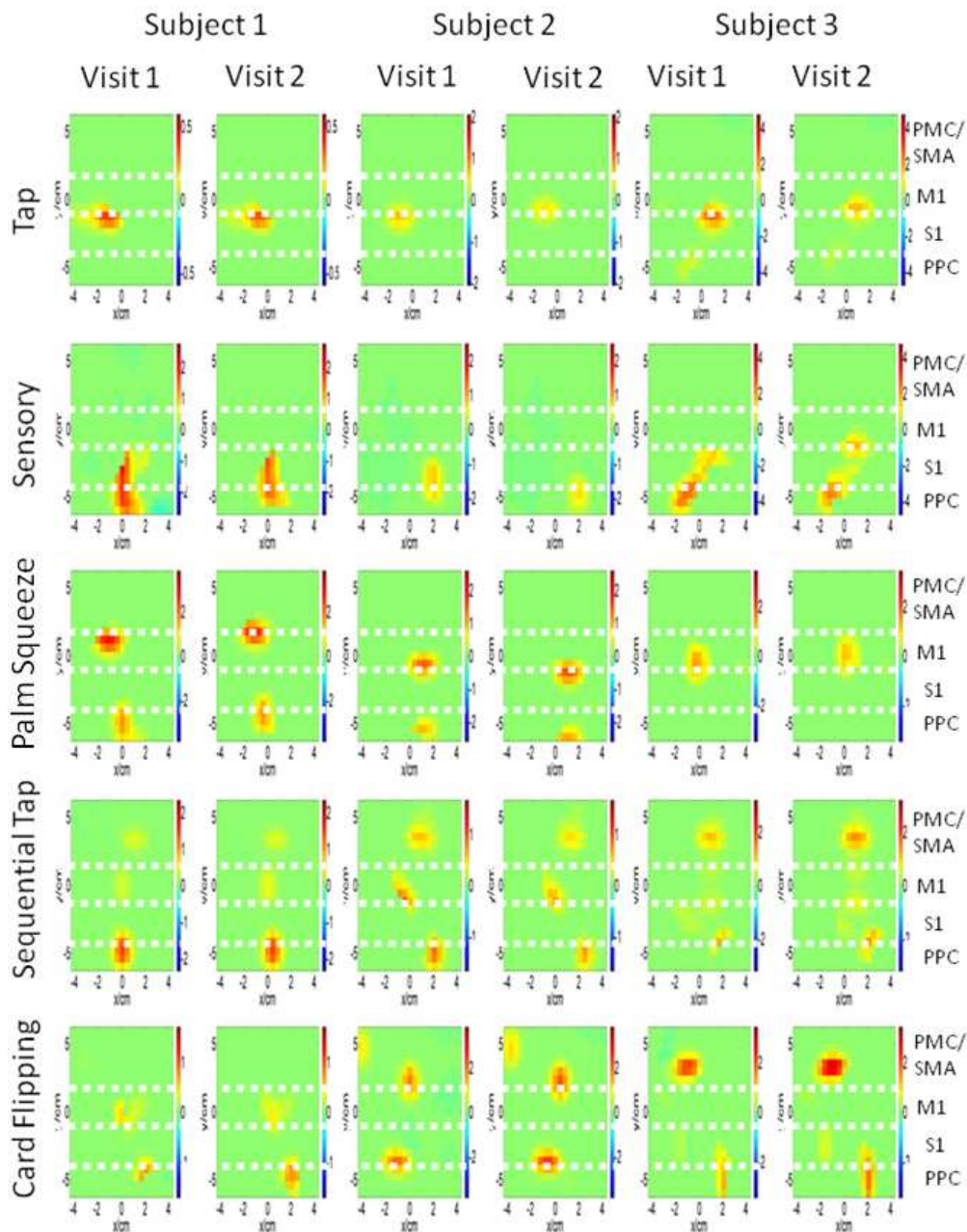


Figure A-0-3 Activation images, having color scales in μMolar , were time-averaged between 5 – 20 s for each task on both visits for all three subjects. The white dashed lines were used to approximately separate the PMC/SMA, M1, S1, and PPC cortical regions, as identified on the far right edge of the figure.

From observing Table A-1 it is seen that cortical regions involved with higher amount of physical or mental effort for any given activation protocol have shorter TtP values, i.e. they reach an activation peak more quickly. For example, the M1 column of Table A-1 shows that finger tapping, the simplest motor protocol, had a TtP of 18.13 ± 2.35 s, whereas palm squeezing (14.21 ± 1.84 s) and card flipping (9.55 ± 2.47 s) had earlier TtPs since they used more arm and hand muscles. Though there is a strong trend, the small number of subjects ($n = 3$) prevented any statistical analysis to conclude a significant change due to the low statistical power ($\beta = 0.32$). Furthermore, the more refined movements of sequential tapping also had an early TtP (12.39 ± 3.55 s) matching with previous fNIR results (175). In addition, the S1/PPC column of Table 1 shows a much shorter TtP value for card flipping due to the need for sensory information from the hand to find the decks of cards. Comparing TtP values across the rows of Table A-1, it is seen that sequential tapping peaks relatively early in M1, but card flipping peaks early both in M1 and S1/PPC. These results are consistent with the idea that both protocols require more effort compared to the other protocols used in this work, but card flipping is more demanding in terms of sensory feedback. Finally, as a point of validation, the constant sensory stimulation from a brush resulted in a hemodynamic response with a strong early rise and peaked at 14.21 ± 1.84 s, which agreed with previous fMRI studies using vibrotactile stimulation of the finger tips (181, 254).

Table A-1 A summary of the activated cortical regions and their TtPs for each protocol.

| | PMC/SMA | M1 | S1/PPC |
|---------------------------|--------------------|--------------------|--------------------|
| Tapping | -- | 18.13 ± 2.35 s | 18.13 ± 2.35 s |
| Sensory | -- | -- | 14.21 ± 1.84 s |
| Palm Squeezing | -- | 13.24 ± 2.86 s | 14.04 ± 2.55 s |
| Sequential Tapping | 16.21 ± 2.18 s | 12.39 ± 3.55 s | 16.92 ± 2.14 s |
| Card Flipping | 17.31 ± 2.22 s | 10.64 ± 1.88 s | 9.55 ± 2.47 s |

Further investigation shows that increased effort also increases the duration of the hemodynamic response, as shown in Table A-2.

Table A-2 A summary of the activated cortical regions and their durations for each protocol.

| | PMC/SMA | M1 | S1/PPC |
|---------------------------|----------------|----------------|----------------|
| Tapping | -- | 18.68 ± 2.83 s | 18.68 ± 2.83 s |
| Sensory | -- | -- | 23.52 ± 2.94 s |
| Palm Squeezing | -- | 35.13 ± 3.21 s | 33.07 ± 3.01 s |
| Sequential Tapping | 22.67 ± 3.57 s | 15.43 ± 2.46 s | 22.13 ± 3.24 s |
| Card Flipping | 23.18 ± 2.84 s | 16.23 ± 2.87 s | 23.17 ± 2.67 s |

Palm squeezing, the most physically enduring task, had a very large increase in duration in comparison to the other tasks, as seen in the columns of M1 (35.13 ± 3.21 s) and S1/PPC (33.07 ± 3.01 s). The palm squeezing hemodynamic response did decay before the measured 40 s (data not shown), though the figure only shows up to 30 s due to space constraints. Moreover across the rows, sequential tapping and card flipping both had shorter durations in M1 (15.43 ± 2.46 s and 16.23 ± 2.87 s, respectively) than those found in PMC/SMA (22.67 ± 3.57 s and 23.18 ± 2.84 s, respectively) and S1/PPC (22.13 ± 3.24 s and 23.17 ± 2.67 s, respectively). The large amount of continuous external sensory information and feedback needed for these latter tasks explains the extended activation duration for the PMC/SMA and S1/PPC regions. Though the increased effort shortened the TtP in M1 (Table A-1), the amount of physical strain was not to the extent of that in palm squeezing and this may be the reason why the duration of hemodynamic response for sequential tapping and card flipping in M1 was not as prolonged.

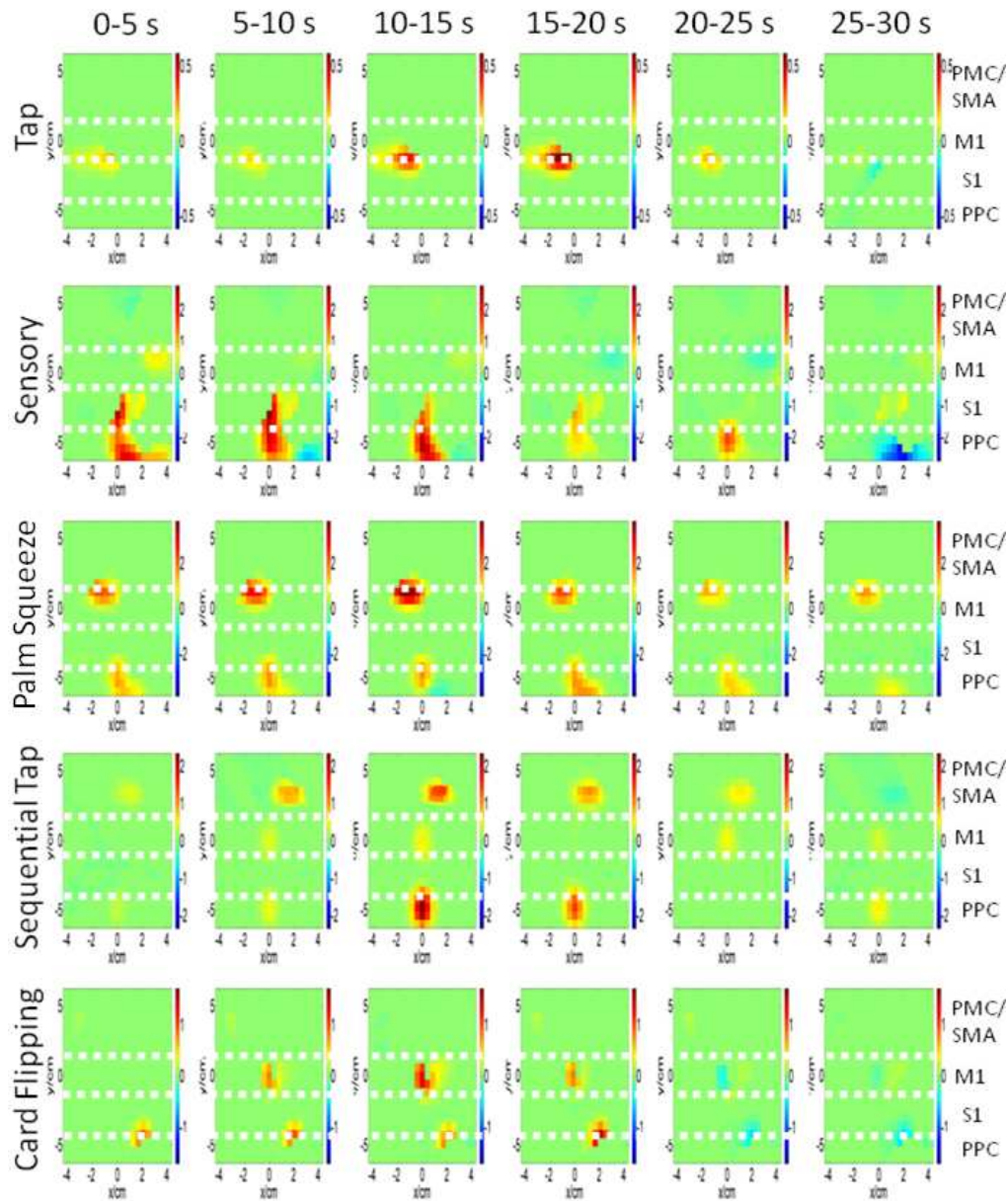


Figure A-0-4 A time series of activation images, having color scales in μMolar , were time-averaged for every 5 s block over a 30 s period of 15 s stimulation – 15 s rest for a single subject performing all five protocols. The white, dashed lines were used to differentiate between the PMC/SMA, M1, S1, and PPC cortical regions, as identified on the far right edge of the figure.

The palm squeezing, sequential tapping and card flipping protocols increased the amount of effort compared to finger tapping either physically or mentally. The squeezing of a stress ball (palm squeeze) increased the physical effort and induced activation in the M1, S1, and PPC regions of the cortex (Fig. A-3, row 3), in agreement with previous fMRI studies (255). Next a sequential tapping protocol increased the mental effort required of the subjects in executing a physical task. Images for this protocol (Fig. A-3, row 4) show additional activation in the PMC/SMA cortex. Finally, the same cortical regions were found to be activated due to card flipping as for the sequential finger tapping protocol. It is important to iterate that sensory feedback was important for the card flipping protocol due to the subject's need to feel for the card's location by hand without looking at the deck, since the subject's visual attention was directed towards the computer screen. The results for both the sequential tapping and card flipping protocols are consistent with the notion that when sensory feedback is needed in order to execute a motion, there is activity in the PMC/SMA cortical areas (232, 256-259).

A.3.2.2 Spatiotemporal Clustering

Though TtP and duration were found to be useful metrics for identifying similarities and differences between time-series activation patterns, these were not necessarily indicative of the overall temporal pattern similarity between different cortical regions. It was hypothesized that if similar time-series activation patterns existed between spatially distinct cortical regions, irrespective of activation amplitude, this pattern similarity could indicate a possible functional relation between these regions.

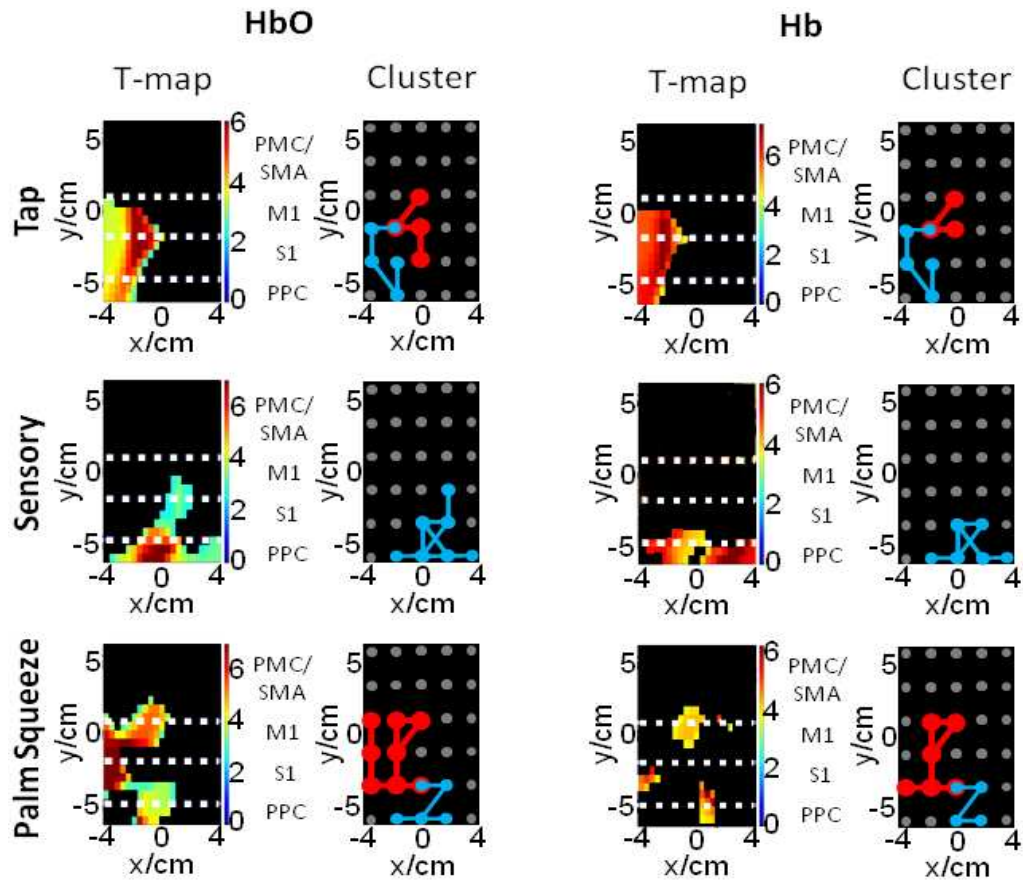


Figure A-0-5 T-maps and clustered source-detector maps for HbO (left columns) and Hb (right columns) for Subject 1 performing the finger tapping, sensory stimulation, and palm squeezing protocols (rows). The white dashed lines indicate approximate boundaries for the PMC/SMA, M1, S1, and PPC regions. The connected circles in the cluster maps indicate the source-detector pairs that CCA grouped in the same cluster as they had similar time-series activation profiles [Tapping: M1/S1 – red, S1/PPC – blue; Sensory Stimulation: S1/PPC – blue; Palm Squeezing: M1/S1 – red; S1/PPC – blue].

In this analysis the source-detector pairs with statistically significant activation over the background hemodynamic fluctuations were first identified using a T-test (247), and subsequently fNIR signals were clustered into regions with respect to their similarity in temporal patterns by use of the CCA algorithm (238), as described in the Methods Section. The results

for finger tapping, sensory stimulation, and palm squeeze T-value maps and clustered regions are shown in Fig. A-5 for Subject 1. Similar results were found for the other subjects, but are not shown here for brevity. The HbO T-tests indicated activation region sizes that appear larger than the activation images shown in Figs. A-3 and A-4. Moreover, in the cluster images (Fig. A-5) S1 and PPC were grouped into one cluster and the M1 region into another for finger tapping and palm squeezing, suggesting communication between the cortical regions, which is consistent with previous fMRI and electrophysiological studies (100, 102, 181, 251, 260). Additionally, the Hb T-maps presented smaller areas of activation in the same locations as that found for HbO, which is consistent with results of previous studies (100, 261).

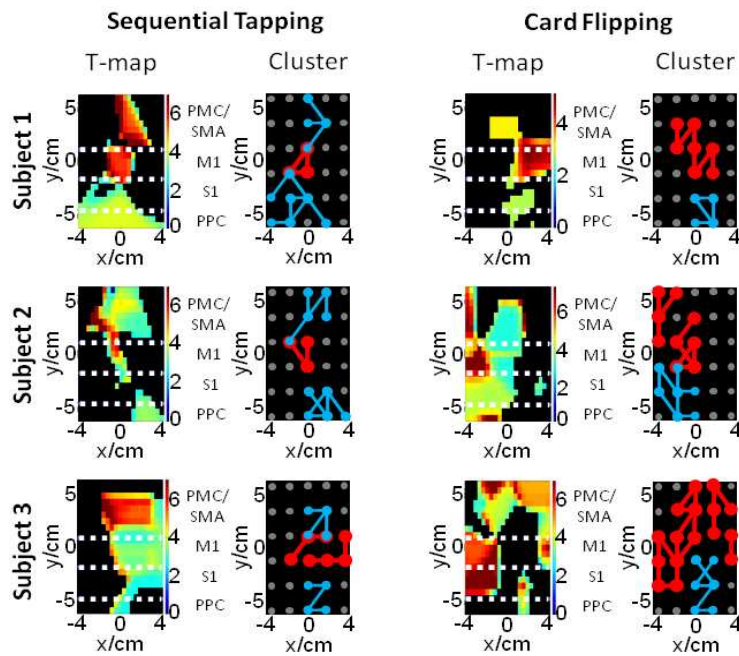


Figure A-0-6 HbO T-maps and clustered source-detector maps for sequential finger tapping (left columns) and card flipping (right columns) for each Subject (rows). The white dashed lines indicate approximate boundaries for the PMC/SMA, M1, S1, and PPC regions. The connected circles in the cluster maps indicate the source-detector pairs that CCA grouped in the same cluster as they had similar time-series activation profiles [Sequential Tapping: M1 – red, S1/PPC and SMA/PMC – blue; Card Flipping: M1 and SMA/PMC – red, S1/PPC – blue].

The cluster analysis was then focused on the sequential tapping and card flipping protocols since these protocols stimulated multiple cortical regions within the FOV due to the complexity of the tasks involved. Comparison, of the cluster map results for these two tasks showed differences in the temporal relation between the involved cortical regions (Fig. A-6). After CCA, both temporal and spatial group analysis were performed to prove the statistical significance of these observed differences. The temporal group analyses proved the statistical significance of the trends seen in Tables A-1 and A-2, above. Specifically, analysis on the card flipping data was performed by combining CCA-selected source-detector pairs with similar patterns in the M1 region to compute a cluster-average TtP (Table A-1, Section A.3.1) and this value was compared with that of corresponding clusters created from CCA of the finger tapping and palm squeezing tasks. The TtP for card flipping was found to be significantly different ($p = 0.019$) with respect to these other two motion tasks with high statistical power ($\beta = 0.98$). Similarly, if the clusters with similar patterns for sequential finger tapping were merged, the duration (Table A-2, Section A.3.1) of activation in M1 was found to be significantly different from the S1/PPC and PMC/SMA cluster duration ($p = 0.04$). The spatial group analyses showed that source-detector patterns with activation were arranged in different spatial patterns depending on the motion task performed. Specifically, the difference in the frequency that a given cluster was assigned to each source-detector pair was tested across motion tasks with Fisher's exact test and was found to be significantly different between all tasks ($p < 0.0001$). Also, the post-hoc analysis found that each task was significantly different from all the others ($p < 0.05$), except between palm squeezing and card flipping ($p = 0.56$). Moreover, group T-maps created by the T-test of the concatenated time-series pixels of each subject for the sequential tapping and card flipping tasks showed that the S1/PPC, M1, and PMC/SMA regions had significant activation consistently for all subjects ($p < 0.0001$) [60].

When comparing T-maps with corresponding HbO activation images (e.g. Fig. A-4 with Fig. A-5, or Fig. A-3 with Fig. A-6) it was found that, even after applying Bonferroni's correction ($p < 0.0001$), T-maps typically indicated larger areas of activation that engulfed the areas seen in HbO images. This apparent activation pattern difference occurred because T-maps included areas of low amplitude activation that were statistically significant, as deduced from univariate analysis of each pixel's amplitude fluctuations with respect to baseline values. In contrast, in HbO images the color assigned by the HomER analysis software for a pixel with a given activation amplitude depended on its relative magnitude with respect to the image maximum and minimum values. In that case the low amplitude activation pixels were assigned colors very close to those of background and were therefore not visually discernible, thus making the apparent size of activation areas smaller. Furthermore, due to the better ability of T-maps to indicate lower amplitude activation areas, there were few instances where activation in functionally distinct regions was only discernible in the T-maps. An example can be seen for Subject 1 doing finger tapping, where no activation was discernible in the PPC (FOV bottom) for HbO images (Fig. A-4 – top row) but activation was seen in the PPC for T-maps (Fig. A-5 – top left panel), consistent with prior fMRI studies [16, 46-48]. This difference was also observed in the other subjects (images not shown for brevity).

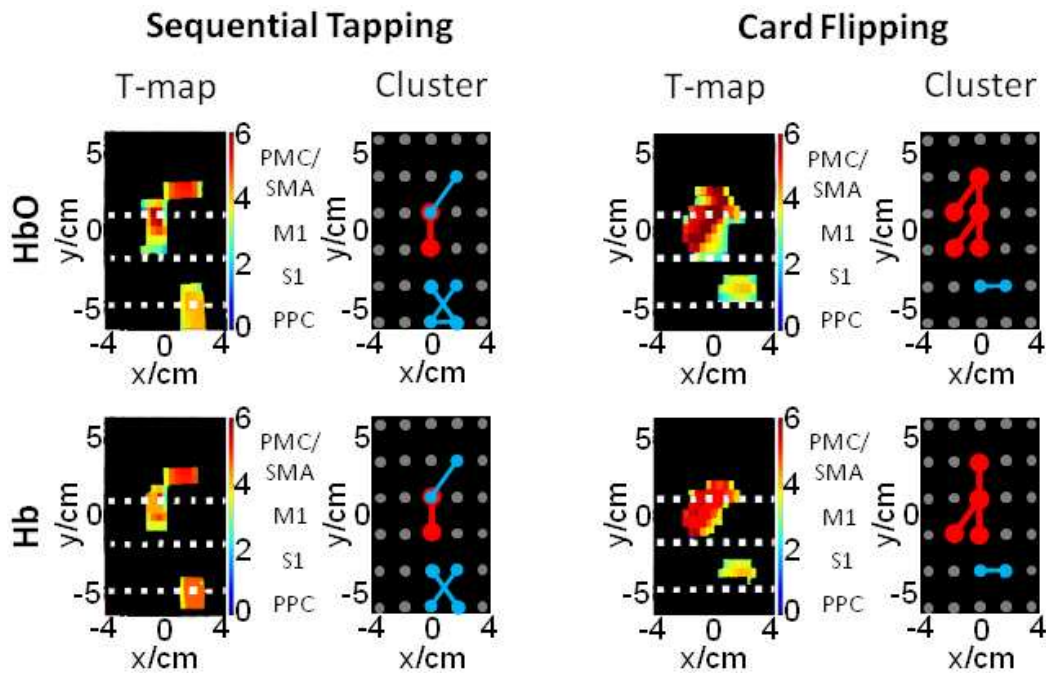


Figure A-0-7 Group analysis T-maps and the clustered fNIR signals for sequential tapping and card flipping. The white dashed lines were used to approximately separate the PMC/SMA, M1, S1, and PPC regions. The connected circles in the cluster maps indicate the source-detector pairs that CCA grouped in the same cluster as they had similar time-series activation profiles

[Sequential Tapping: M1/S1 – red, S1/PPC and M1/PMC/SMA – blue; Card Flipping: M1/SMA/PMC – red, S1/PPC - blue.

Fascinatingly, in Fig. A-7 it is seen that the secondary motor cortices (PMC and SMA) clustered together with the S1 and PPC areas for sequential tapping, which depended on visual cues to execute the protocol. In contrast, for the card flipping task, which depended more heavily on sensory information from the hand and arm to identify the location of the decks of cards, the S1, PPC, and M1 regions clustered together. Though previous fMRI studies have used sensory based protocols to determine the relation of the PPC to the motor and sensory systems (181, 251, 261), there are no studies to our knowledge, which compare the temporal hemodynamic profiles of these separate cortical regions. On the other hand electrophysiological

studies in monkeys have shown that the PMC/SMA region is active before the movement, between movements, and during the movement if there is an external cue (252, 256, 257, 259, 262). The fact that the spatiotemporal clustering results were consistent with prior literature suggests that similarity in hemodynamic activation patterns, though slower and secondary to neuronal activation, could be indicative of the functional relations between these different cortical regions.

Resting state functional connectivity has also been used to determine the functional relations between cortical regions by looking at their temporal correlations (263, 264). Since this is done at a resting state, a cortical region may be found to be well correlated with several regions of the brain, though some of these connections may not be functionally relevant for a specified task. Previous fNIR studies, including this study (data not shown), found broad cortical connectivity between motor and sensory cortical regions using resting state and functional connectivity analysis. On the other hand, the use of CCA for a stimulation paradigm gives functional relations between cortical regions during a specified task, thus giving a more indicative task-specific functional connection between cortical regions.

A.4 Conclusions

This work demonstrated the feasibility of performing fNIR measurements over an extended FOV (12 x 8.4 cm) spanning the primary sensorimotor and secondary motor cortex and identified spatiotemporal interrelations between different activation regions for various hand and arm movements. In addition to activation by the popular finger tapping and sensory stimulation protocols (181, 182, 251), palm squeezing, sequential tapping, and card flipping (supination and pronation) protocols were also demonstrated for this extended FOV. The variety of protocols enabled detecting concurrent activation from several cortical regions within the measured FOV including the SMA, PMC, M1, S1 and PPC. Our results of the areas activated and temporal activation characteristics of the hemodynamic response for each protocol

matched well with previous fMRI and electrophysiological studies (252, 259, 262), though to our knowledge, card flipping has not been done before in previous fMRI or fNIR studies.

Additionally, a CCA algorithm was used to cluster cortical regions with similar temporal activation patterns (238), indicating functional relations between cortical regions for a specified task. Analysis of time-series fNIR data for the different protocols performed showed earlier peaking of activation as well as longer activation duration for the tasks requiring higher physical effort (palm squeezing), or higher mental effort (sequential tapping and card flipping). As can be seen from Table A-1, with increasing physical demand or sensory feedback needed to perform a task, there was an earlier TtP found in M1, S1 and PPC with finger tapping being the simplest motor task. On the other hand, sequential tapping did not follow this pattern in S1 and PPC since there was no increase of sensory stimuli from the arm or hand, but there was an increase of sensory information from the visual cortex in order to identify the number with the proper finger. Additional analysis in Table A-2 presented an increase in duration in M1, S1, and PPC if there was large increase in physical demand (palm squeezing), or in the PMC/SMA, S1, and PPC if there was a large increase in sensory feedback (sequential tapping and card flipping).

A clustering analysis method for comparing the similarity of time-series activation data irrespective of amplitude was also used to compare patterns between spatially distinct activation regions (238). It was found that when the subject relied more heavily on visual guidance to perform a protocol, temporal patterns between the PPC/S1 and the secondary motor regions (PMC/SMA) of the cortex had similar temporal patterns. Furthermore, when sensory information from the hand directed the movement of flipping playing cards, the PPC/S1 had similar temporal profiles with the M1 region of the cortex. With the large FOV and the diverse protocols used in this study, there is noticeable importance in imaging the PPC and secondary motor cortical regions (PMC/SMA) due to the sensory feedback they provide for the execution of more complex tasks.

The findings of this work indicate that there is rich information to be obtained from the spatiotemporal relations between different cortical activation regions when performing fNIR imaging over an extended area encompassing the sensorimotor, secondary motor cortex, and PPC. Unfortunately, the limited number of source-detector channels in our currently available fNIR imaging system limited functional imaging to only one brain hemisphere for this FOV size. The commercial availability of future fNIR imaging systems with substantially higher source-detector channels will enable performing extended FOV measurements bilaterally in the brain. Such measurements will be of great use for many functional imaging studies, including ones underlying the motivation for the present work, namely the longitudinal monitoring of cortical plasticity during rehabilitation of patients with motor deficits (115, 116, 125).

Appendix B

CCA Algorithm for FNIR Imaging

This Section describes how the CCA algorithm, originally used in the fMRI field (238), was adapted in this work to perform the analysis of fNIR imaging data. In the fNIR spectroscopy field, blood concentration and oxygenation changes secondary to neuronal activation are reconstructed into maps of absorbance change after applying a modified Beer-Lambert law (96). More specifically, maps for the change in optical density (ΔOD_λ) for every wavelength (λ) detected by a given number of source-detector pairs (SD) at any one time point are reconstructed by inverting Eq. B-1. In that equation y_λ is an SD x 1 array of the ΔOD_λ for each source-detector, A_λ is the joint probability distribution for each source-detector pairs [46], and x_λ is the reconstructed ΔOD_λ image (N pixels) for one time point. A ΔOD_λ image is then reconstructed by taking the regularized inverse of A_λ as shown in Eq. B-2, where A^T is the transpose of A , α is the regularization parameter (0.01), s_{\max} is the largest eigenvalue of $E[AA^T]$, and I is the identity matrix (96):

$$y_\lambda = A_\lambda x_\lambda \quad \text{(B-1)}$$

$$x_\lambda = A_\lambda^T (A_\lambda^T A_\lambda + \alpha s_{\max} I)^{-1} y_\lambda = A_{inv,\lambda} y_\lambda \quad \text{(B-2)}$$

However, because the target of this work was to identify and cluster fNIR signals with similar temporal patterns it was necessary to consider data for all time points at once. Therefore time-series source-detector signals and their corresponding time-series images were expressed in a form described by Eq. B-3, where X_λ (time x N) was the time-series for each pixel from the reconstructed ΔOD_λ images and Y_λ (SD x time) were the ΔOD_λ time signals for each source-detector pair:

$$X_\lambda = Y_\lambda^T A_{inv,\lambda}^T \quad \text{(B-3)}$$

Before the fNIR signals could be decomposed into a signal harmonic subspace, a model matrix was created in which each column consisted of a full time-series (450 s) of sine waves whose frequencies were multiples of the fundamental frequency. A

fundamental frequency of 0.02 Hz was assigned as that was the frequency equal to the inverse of the duration of a task epoch. Each column of the model matrix did not extend the full 450-s time-series if some of the 40-s activation-rest intervals were removed due to motion artifacts (see Section A.2.6). All harmonics (f) of the fundamental frequency up to half the sampling rate (Nyquist frequency) were input into the model matrix H (time x f). From Eq. B-3, each ΔOD_λ was then decomposed into harmonic components using a general linear model ($Y_\lambda^T = H_\lambda \theta_\lambda + v$), where θ_λ ($f \times SD$) was the harmonic image matrix consisting of the weight coefficients (arbitrary units of ΔOD_λ) to each frequency harmonic and v (time x SD) was the noise estimated from the residuals of the linear model. This noise consisted of instrumentation dark noise and the residual signal from the physiological hemodynamics that were not removed by the PCA and adaptive filtering procedures applied to the measured fNIR signals. This noise was determined to be effectively white. The above considerations resulted in Eq. B-4:

$$X_\lambda = (H\theta_\lambda + v)A_{inv,\lambda}^T \quad (\text{B-4})$$

Beginning with the reconstructed ΔOD_λ images for the whole time series, a least squares estimate of θ ($\hat{\theta}_\lambda$) was computed (Eq. B-5), which consisted of the weight coefficients to each frequency harmonic. The resulting estimation error was then found by Eq. B-6.

$$\hat{\theta}_\lambda = (H^T H)^{-1} H^T X_\lambda A_\lambda^T \quad (\text{B-5})$$

$$\tilde{\theta}_\lambda = \hat{\theta}_\lambda - \theta_\lambda = (H^T H)^{-1} H^T v A_{inv,\lambda}^T A_\lambda^T \quad (\text{B-6})$$

By computing the covariance matrix of the least squares estimate (Eq. B-7) and the estimation error of the harmonic image matrix (Eq. B-8), the covariance matrix of the noiseless harmonic image matrix θ was found (Eq. B-9). By computing the eigenvalues of

the covariance matrix of θ (Eq. B-9), using Schur decomposition (125, 265), and eliminating all components with negative amplitude, the harmonic subspace was reduced to include only those harmonics that spanned the ΔOD_λ time-series signals. The reduced harmonic subspace θ_λ^* for those ΔOD_λ signals was determined by Eq. B-10 where U^* was the reduced eigenvector matrix that included only the eigenvectors corresponding to positive eigenvalues Λ_λ (from Eq. B-9):

$$R_{sn,\lambda} = \frac{1}{SD} E[\hat{\theta}_\lambda \hat{\theta}_\lambda^T] \quad (\text{B-7})$$

$$R_{n,\lambda} = \frac{1}{SD} E[\tilde{\theta}_\lambda \tilde{\theta}_\lambda^T] \quad (\text{B-8})$$

$$R_{s,\lambda} = R_{sn,\lambda} - R_{n,\lambda} = U_\lambda \Lambda_\lambda U_\lambda^T \quad (\text{B-9})$$

$$\theta_\lambda^* = U_\lambda^T \hat{\theta}_\lambda \quad (\text{B-10})$$

Since the harmonic subspace θ_λ^* was in arbitrary units of ΔOD_λ , the conversion to change in HbO and Hb, Eqs. B-11-12, for each matrix entry was performed by applying the modified Beer-Lambert Law at the two wavelengths (96). In these equations ϵHbO_λ was the extinction coefficient of HbO at wavelength λ , ϵHb_λ was the extinction coefficient of Hb at wavelength λ , and L was the pathlength of the light through the tissue (calculated as source-detector separation times a differential pathlength factor of six (98)):

$$\Delta[\text{Hb}] = (\epsilon HbO_{\lambda_2} \Delta OD_{\lambda_1} - \epsilon HbO_{\lambda_1} \Delta OD_{\lambda_2}) / (L(\epsilon Hb_{\lambda_1} \epsilon HbO_{\lambda_2} - \epsilon Hb_{\lambda_2} \epsilon HbO_{\lambda_1})) \quad (\text{B-11})$$

$$\Delta[\text{HbO}] = (\epsilon Hb_{\lambda_2} \Delta OD_{\lambda_1} - \epsilon Hb_{\lambda_1} \Delta OD_{\lambda_2}) / (L(\epsilon Hb_{\lambda_2} \epsilon HbO_{\lambda_1} - \epsilon Hb_{\lambda_1} \epsilon HbO_{\lambda_2})) \quad (\text{B-12})$$

Finally, only those source-detector pairs with significant HbO and Hb activation were fed into the CCA algorithm. Significant activation was identified by comparing, for

the time-series of each fNIR signal, the mean and standard deviation of the changes in Hb and HbO during the activation period (5 s to 20 s) relative to changes in baseline values acquired just prior to activation (-10 s to 0 s). After applying Bonferroni's correction for multiple comparisons (146) source-detector pairs were considered to have significant activation when $p < 0.0001$. The CCA algorithm (238) then clustered fNIR signals into a self-determined number of groups with similarly weighted harmonic components and therefore similar time-series shapes irrespective of activation magnitude.

Appendix C

Setup for ptDCS Titration and Scalp Effects

This section describes the tDCS and fNIRS setup used to test if tDCS effects on scalp hemodynamics affected fNIRS cortical measurements, and to demonstrate that effects at lower currents on muscle activity have a similar trend at higher currents. In order to do so, tDCS electrodes were placed over the primary motor cortex (M1) of each hemisphere (C₃ and C₄ positions of EEG 10/20 system), such that the anode was placed over the contralateral hemisphere and the cathode over the ipsilateral hemisphere (Fig. 2M). This montage was used since it was shown to increase WF activity (Chapter 4). FNIRS fiber bundles were placed around each electrode, in which the multiple short (1 cm) source-detector pairs measured ΔHbO from the scalp, while the long (2.5 cm - 3.5 cm) source-detector pairs measured ΔHbO from the cortex. Additionally, sEMG measurements and task performance measures were recorded for each subjects (Khan 2013).

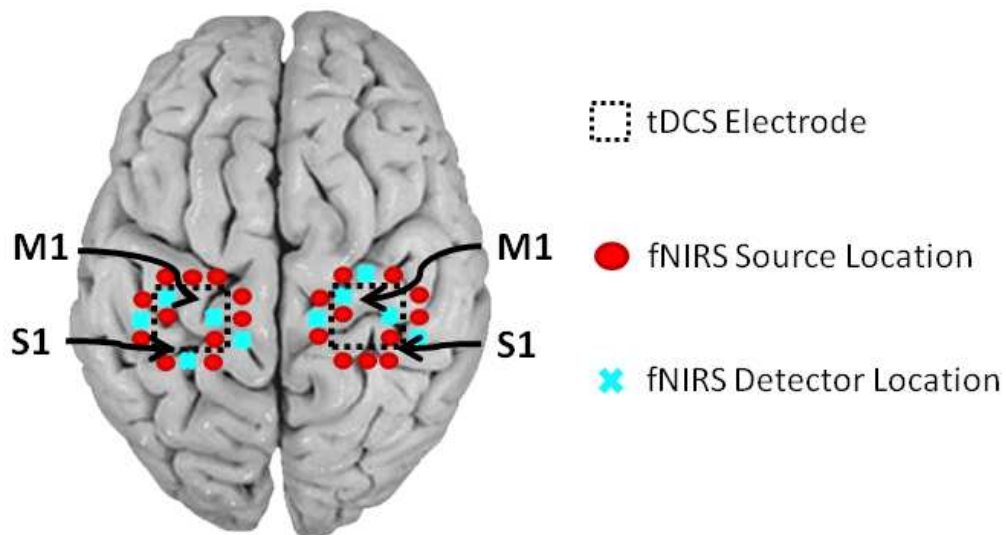


Figure C-1 TDCS and fNIRS setup used to determine tDCS effects on scalp hemodynamics and current increase effects on muscle activity.

A single session had five measurements where each measurement followed the protocol described in Fig. 5-2B, with the exception of one. The first measurement comprised of no tDCS stimulation. The second applied tDCS with a current of 0.5 mA, however the subjects remained at rest and did not perform the wrist flexion task. The final three measurements consisted of tDCS at 0.5 mA, 1.0 mA, and 2 mA, respectively, while the subjects performed the wrist flexion task. After the 1.0 mA stimulation, subjects waited an additional 10 minutes after the end of the measurement in order for the hemodynamics to return to its original baseline seen before tDCS.

References

1. Corrigan JD, Whiteneck G, & Mellick D (2004) Perceived needs following traumatic brain injury. (Translated from eng) *J Head Trauma Rehabil* 19(3):205-216 (in eng).
2. M. Faul LX, M.M. Wald, and V.G. Coronado (2010) Traumatic Brain Injury in the United States: Emergency Department Visits, Hospitalizations and Deaths 2002–2006.
3. Paneth N, Hong T, & Korzeniewski S (2006) The descriptive epidemiology of cerebral palsy. (Translated from eng) *Clin Perinatol* 33(2):251-267 (in eng).
4. Roger VL, *et al.* (2012) Heart disease and stroke statistics--2012 update: a report from the American Heart Association. (Translated from eng) *Circulation* 125(1):e2-e220 (in eng).
5. Bonifer NM, Anderson KM, & Arciniegas DB (2005) Constraint-induced movement therapy after stroke: efficacy for patients with minimal upper-extremity motor ability. (Translated from eng) *Arch Phys Med Rehabil* 86(9):1867-1873 (in eng).
6. Caimmi M, *et al.* (2008) Using kinematic analysis to evaluate constraint-induced movement therapy in chronic stroke patients. (Translated from eng) *Neurorehabil Neural Repair* 22(1):31-39 (in eng).
7. Eliasson AC, Krumlinde-sundholm L, Shaw K, & Wang C (2005) Effects of constraint-induced movement therapy in young children with hemiplegic cerebral palsy: an adapted model. (Translated from eng) *Dev Med Child Neurol* 47(4):266-275 (in eng).
8. Geerdink Y, Aarts P, & Geurts AC (2013) Motor learning curve and long-term effectiveness of modified constraint-induced movement therapy in children with unilateral cerebral palsy: a randomized controlled trial. (Translated from eng) *Res Dev Disabil* 34(3):923-931 (in eng).
9. Gordon AM, *et al.* (2008) Both constraint-induced movement therapy and bimanual training lead to improved performance of upper extremity function in children with hemiplegia. (Translated from eng) *Dev Med Child Neurol* 50(12):957-958 (in eng).
10. Hoare BJ, Imms C, Rawicki HB, & Carey L (2010) Modified constraint-induced movement therapy or bimanual occupational therapy following injection of Botulinum toxin-A to improve bimanual performance in young children with hemiplegic cerebral palsy: a randomised controlled trial methods paper. (Translated from eng) *BMC Neurol* 10:58 (in eng).
11. Kagawa S, *et al.* (2013) Effects of constraint-induced movement therapy on spasticity in patients with hemiparesis after stroke. (Translated from eng) *J Stroke Cerebrovasc Dis* 22(4):364-370 (in eng).
12. McIntyre A, *et al.* (2012) Systematic review and meta-analysis of constraint-induced movement therapy in the hemiparetic upper extremity more than six months post stroke. (Translated from eng) *Top Stroke Rehabil* 19(6):499-513 (in eng).
13. Shaw SE, *et al.* (2005) Constraint-induced movement therapy for recovery of upper-limb function following traumatic brain injury. (Translated from eng) *J Rehabil Res Dev* 42(6):769-778 (in eng).
14. Smania N, *et al.* (2012) Reduced-intensity modified constraint-induced movement therapy versus conventional therapy for upper extremity rehabilitation

- after stroke: a multicenter trial. (Translated from eng) *Neurorehabil Neural Repair* 26(9):1035-1045 (in eng).
15. Stearns GE, Burtner P, Keenan KM, Qualls C, & Phillips J (2009) Effects of constraint-induced movement therapy on hand skills and muscle recruitment of children with spastic hemiplegic cerebral palsy. (Translated from eng) *NeuroRehabilitation* 24(2):95-108 (in eng).
 16. van Delden AL, *et al.* (2013) Unilateral versus bilateral upper limb training after stroke: the Upper Limb Training After Stroke clinical trial. (Translated from eng) *Stroke* 44(9):2613-2616 (in eng).
 17. Wang Q, Zhao JL, Zhu QX, Li J, & Meng PP (2011) Comparison of conventional therapy, intensive therapy and modified constraint-induced movement therapy to improve upper extremity function after stroke. (Translated from eng) *J Rehabil Med* 43(7):619-625 (in eng).
 18. Wu CY, Chuang LL, Lin KC, Chen HC, & Tsay PK (2011) Randomized trial of distributed constraint-induced therapy versus bilateral arm training for the rehabilitation of upper-limb motor control and function after stroke. (Translated from eng) *Neurorehabil Neural Repair* 25(2):130-139 (in eng).
 19. Bovolenta F, Sale P, Dall'Armi V, Clerici P, & Franceschini M (2011) Robot-aided therapy for upper limbs in patients with stroke-related lesions. Brief report of a clinical experience. (Translated from eng) *J Neuroeng Rehabil* 8:18 (in eng).
 20. Norouzi-Gheidari N, Archambault PS, & Fung J (2012) Effects of robot-assisted therapy on stroke rehabilitation in upper limbs: systematic review and meta-analysis of the literature. (Translated from eng) *J Rehabil Res Dev* 49(4):479-496 (in eng).
 21. Squeri V, Masia L, Giannoni P, Sandini G, & Morasso P (2013) Wrist Rehabilitation in Chronic Stroke Patients by Means of Adaptive, Progressive Robot Aided Therapy. (Translated from Eng) *IEEE Trans Neural Syst Rehabil Eng* (in Eng).
 22. Jost WH, Hefter H, Reissig A, Kollwe K, & Wissel J (2013) Efficacy and safety of botulinum toxin type A (Dysport) for the treatment of post-stroke arm spasticity: Results of the German-Austrian open-label post-marketing surveillance prospective study. (Translated from Eng) *J Neurol Sci* (in Eng).
 23. Platz T, *et al.* (2005) Amphetamine fails to facilitate motor performance and to enhance motor recovery among stroke patients with mild arm paresis: interim analysis and termination of a double blind, randomised, placebo-controlled trial. (Translated from eng) *Restor Neurol Neurosci* 23(5-6):271-280 (in eng).
 24. Lowe K, Novak I, & Cusick A (2007) Repeat injection of botulinum toxin A is safe and effective for upper limb movement and function in children with cerebral palsy. (Translated from eng) *Dev Med Child Neurol* 49(11):823-829 (in eng).
 25. Butler AJ & Wolf SL (2007) Putting the brain on the map: use of transcranial magnetic stimulation to assess and induce cortical plasticity of upper-extremity movement. (Translated from eng) *Phys Ther* 87(6):719-736 (in eng).
 26. Kandel M, Beis JM, Le Chapelain L, Guesdon H, & Paysant J (2012) Non-invasive cerebral stimulation for the upper limb rehabilitation after stroke: A review. (Translated from eng) *Annals of physical and rehabilitation medicine* 55(9-10):657-680 (in eng).
 27. Kim YH, *et al.* (2006) Repetitive transcranial magnetic stimulation-induced corticomotor excitability and associated motor skill acquisition in chronic stroke. (Translated from eng) *Stroke* 37(6):1471-1476 (in eng).

28. Kirton A, *et al.* (2008) Contralesional repetitive transcranial magnetic stimulation for chronic hemiparesis in subcortical paediatric stroke: a randomised trial. (Translated from eng) *Lancet Neurol* 7(6):507-513 (in eng).
29. Tarkka IM, Pitkanen K, Popovic DB, Vanninen R, & Kononen M (2011) Functional electrical therapy for hemiparesis alleviates disability and enhances neuroplasticity. (Translated from eng) *Tohoku J Exp Med* 225(1):71-76 (in eng).
30. Boggio PS, *et al.* (2007) Repeated sessions of noninvasive brain DC stimulation is associated with motor function improvement in stroke patients. (Translated from eng) *Restorative neurology and neuroscience* 25(2):123-129 (in eng).
31. Hummel F, *et al.* (2005) Effects of non-invasive cortical stimulation on skilled motor function in chronic stroke. (Translated from eng) *Brain : a journal of neurology* 128(Pt 3):490-499 (in eng).
32. Lindenberg R, Renga V, Zhu LL, Nair D, & Schlaug G (2010) Bihemispheric brain stimulation facilitates motor recovery in chronic stroke patients. (Translated from eng) *Neurology* 75(24):2176-2184 (in eng).
33. Nowak DA, Grefkes C, Ameli M, & Fink GR (2009) Interhemispheric competition after stroke: brain stimulation to enhance recovery of function of the affected hand. (Translated from eng) *Neurorehabilitation and neural repair* 23(7):641-656 (in eng).
34. Vines BW, Cerruti C, & Schlaug G (2008) Dual-hemisphere tDCS facilitates greater improvements for healthy subjects' non-dominant hand compared to uni-hemisphere stimulation. (Translated from eng) *BMC neuroscience* 9:103 (in eng).
35. Barros Galvao SC, Borba Costa Dos Santos R, Borba Dos Santos P, Cabral ME, & Monte-Silva K (2013) Efficacy of Coupling Repetitive Transcranial Magnetic Stimulation and Physical Therapy to Reduce Upper-Limb Spasticity in Patients With Stroke: A Randomized Controlled Trial. (Translated from Eng) *Arch Phys Med Rehabil* (in Eng).
36. Lee SJ & Chun MH (2013) Combination Transcranial Direct Current Stimulation and Virtual Reality Therapy for Upper Extremity Training in Patients With Subacute Stroke. (Translated from Eng) *Arch Phys Med Rehabil* (in Eng).
37. Bolognini N, *et al.* (2011) Neurophysiological and behavioral effects of tDCS combined with constraint-induced movement therapy in poststroke patients. (Translated from eng) *Neurorehabilitation and neural repair* 25(9):819-829 (in eng).
38. Hesse S, *et al.* (2007) Combined transcranial direct current stimulation and robot-assisted arm training in subacute stroke patients: a pilot study. (Translated from eng) *Restor Neurol Neurosci* 25(1):9-15 (in eng).
39. Nair DG, Renga V, Lindenberg R, Zhu L, & Schlaug G (2011) Optimizing recovery potential through simultaneous occupational therapy and non-invasive brain-stimulation using tDCS. (Translated from eng) *Restorative neurology and neuroscience* 29(6):411-420 (in eng).
40. Kakuda W, *et al.* (2010) Low-frequency repetitive transcranial magnetic stimulation and intensive occupational therapy for poststroke patients with upper limb hemiparesis: preliminary study of a 15-day protocol. (Translated from eng) *Int J Rehabil Res* 33(4):339-345 (in eng).
41. Kakuda W, *et al.* (2011) Anti-spastic effect of low-frequency rTMS applied with occupational therapy in post-stroke patients with upper limb hemiparesis. (Translated from eng) *Brain Inj* 25(5):496-502 (in eng).

42. Kakuda W, et al. (2011) Application of combined 6-Hz primed low-frequency rTMS and intensive occupational therapy for upper limb hemiparesis after stroke. (Translated from eng) *NeuroRehabilitation* 29(4):365-371 (in eng).
43. Kakuda W, et al. (2012) Combined therapeutic application of botulinum toxin type A, low-frequency rTMS, and intensive occupational therapy for post-stroke spastic upper limb hemiparesis. (Translated from eng) *Eur J Phys Rehabil Med* 48(1):47-55 (in eng).
44. Wang RY, et al. (2012) rTMS combined with task-oriented training to improve symmetry of interhemispheric corticomotor excitability and gait performance after stroke: a randomized trial. (Translated from eng) *Neurorehabil Neural Repair* 26(3):222-230 (in eng).
45. Corbetta D, Sirtori V, Moja L, & Gatti R (2010) Constraint-induced movement therapy in stroke patients: systematic review and meta-analysis. (Translated from eng) *Eur J Phys Rehabil Med* 46(4):537-544 (in eng).
46. Fritz SL, Butts RJ, & Wolf SL (2012) Constraint-induced movement therapy: from history to plasticity. (Translated from eng) *Expert Rev Neurother* 12(2):191-198 (in eng).
47. Pomeroy VM, et al. (2007) Transcranial magnetic stimulation and muscle contraction to enhance stroke recovery: a randomized proof-of-principle and feasibility investigation. (Translated from eng) *Neurorehabil Neural Repair* 21(6):509-517 (in eng).
48. Tretriluxana J, Gordon J, Fisher BE, & Winstein CJ (2009) Hemisphere specific impairments in reach-to-grasp control after stroke: effects of object size. (Translated from eng) *Neurorehabil Neural Repair* 23(7):679-691 (in eng).
49. Emara TH, et al. (2010) Repetitive transcranial magnetic stimulation at 1Hz and 5Hz produces sustained improvement in motor function and disability after ischaemic stroke. (Translated from eng) *Eur J Neurol* 17(9):1203-1209 (in eng).
50. Tretriluxana J, Kantak S, Tretriluxana S, Wu AD, & Fisher BE (2013) Low frequency repetitive transcranial magnetic stimulation to the non-lesioned hemisphere improves paretic arm reach-to-grasp performance after chronic stroke. (Translated from eng) *Disabil Rehabil Assist Technol* 8(2):121-124 (in eng).
51. Mansur CG, et al. (2005) A sham stimulation-controlled trial of rTMS of the unaffected hemisphere in stroke patients. (Translated from eng) *Neurology* 64(10):1802-1804 (in eng).
52. Saucedo Marquez CM, Zhang X, Swinnen SP, Meesen R, & Wenderoth N (2013) Task-specific effect of transcranial direct current stimulation on motor learning. (Translated from eng) *Front Hum Neurosci* 7:333 (in eng).
53. Nitsche MA & Paulus W (2011) Transcranial direct current stimulation--update 2011. (Translated from eng) *Restorative neurology and neuroscience* 29(6):463-492 (in eng).
54. Lefebvre S, et al. (2012) Dual-tDCS Enhances Online Motor Skill Learning and Long-Term Retention in Chronic Stroke Patients. (Translated from eng) *Front Hum Neurosci* 6:343 (in eng).
55. Lefebvre S, et al. (2014) Single session of dual-tDCS transiently improves precision grip and dexterity of the paretic hand after stroke. (Translated from eng) *Neurorehabil Neural Repair* 28(2):100-110 (in eng).
56. Schambra HM, et al. (2011) Probing for hemispheric specialization for motor skill learning: a transcranial direct current stimulation study. (Translated from eng) *Journal of neurophysiology* 106(2):652-661 (in eng).

57. Leite J, Carvalho S, Fregni F, Boggio PS, & Goncalves OF (2013) The effects of cross-hemispheric dorsolateral prefrontal cortex transcranial direct current stimulation (tDCS) on task switching. (Translated from eng) *Brain Stimul* 6(4):660-667 (in eng).
58. Cha HK, Ji SG, Kim MK, & Chang JS (2014) Effect of transcranial direct current stimulation of function in patients with stroke. (Translated from eng) *J Phys Ther Sci* 26(3):363-365 (in eng).
59. Kasahara K, Tanaka S, Hanakawa T, Senoo A, & Honda M (2013) Lateralization of activity in the parietal cortex predicts the effectiveness of bilateral transcranial direct current stimulation on performance of a mental calculation task. (Translated from eng) *Neurosci Lett* 545:86-90 (in eng).
60. Kim GW & Ko MH (2013) Facilitation of corticospinal tract excitability by transcranial direct current stimulation combined with voluntary grip exercise. (Translated from eng) *Neuroscience Letters* 548:181-184 (in eng).
61. O'Shea J, *et al.* (2014) Predicting behavioural response to TDCS in chronic motor stroke. (Translated from eng) *Neuroimage* 85 Pt 3:924-933 (in eng).
62. Reis J, *et al.* (2009) Noninvasive cortical stimulation enhances motor skill acquisition over multiple days through an effect on consolidation. (Translated from eng) *Proc Natl Acad Sci U S A* 106(5):1590-1595 (in eng).
63. Hidler J, Hodics T, Xu B, Dobkin B, & Cohen LG (2006) MR compatible force sensing system for real-time monitoring of wrist moments during fMRI testing. (Translated from eng) *Journal of neuroscience methods* 155(2):300-307 (in eng).
64. Lindenberg R, Nachtigall L, Meinzer M, Sieg MM, & Floel A (2013) Differential effects of dual and unihemispheric motor cortex stimulation in older adults. (Translated from eng) *J Neurosci* 33(21):9176-9183 (in eng).
65. Cuypers K, *et al.* (2013) Anodal tDCS increases corticospinal output and projection strength in multiple sclerosis. (Translated from eng) *Neurosci Lett* 554:151-155 (in eng).
66. Medvedev AV, Kainerstorfer JM, Borisov SV, Gandjbakhche AH, & Vanmeter J (2010) "Seeing" electroencephalogram through the skull: imaging prefrontal cortex with fast optical signal. (Translated from eng) *J Biomed Opt* 15(6):061702 (in eng).
67. Funane T, *et al.* (2011) Synchronous activity of two people's prefrontal cortices during a cooperative task measured by simultaneous near-infrared spectroscopy. (Translated from eng) *J Biomed Opt* 16(7):077011 (in eng).
68. Liao SM, *et al.* (2010) Neonatal hemodynamic response to visual cortex activity: high-density near-infrared spectroscopy study. (Translated from eng) *J Biomed Opt* 15(2):026010 (in eng).
69. Merzagora AC, *et al.* (2010) Prefrontal hemodynamic changes produced by anodal direct current stimulation. (Translated from eng) *NeuroImage* 49(3):2304-2310 (in eng).
70. Zheng X, Alsop DC, & Schlaug G (2011) Effects of transcranial direct current stimulation (tDCS) on human regional cerebral blood flow. (Translated from eng) *NeuroImage* 58(1):26-33 (in eng).
71. Mordillo-Mateos L, *et al.* (2012) Effects of simultaneous bilateral tDCS of the human motor cortex. (Translated from eng) *Brain stimulation* 5(3):214-222 (in eng).
72. Carmichael MD, *et al.* (2010) Role of brain macrophages on IL-1beta and fatigue following eccentric exercise-induced muscle damage. (Translated from eng) *Brain Behav Immun* 24(4):564-568 (in eng).

73. Wieloch T & Nikolich K (2006) Mechanisms of neural plasticity following brain injury. (Translated from eng) *Curr Opin Neurobiol* 16(3):258-264 (in eng).
74. Kleim JA (2011) Neural plasticity and neurorehabilitation: teaching the new brain old tricks. (Translated from eng) *J Commun Disord* 44(5):521-528 (in eng).
75. Chen JL & Schlaug G (2013) Resting state interhemispheric motor connectivity and white matter integrity correlate with motor impairment in chronic stroke. (Translated from eng) *Front Neurol* 4:178 (in eng).
76. Chouinard PA, Leonard G, & Paus T (2006) Changes in effective connectivity of the primary motor cortex in stroke patients after rehabilitative therapy. (Translated from eng) *Exp Neurol* 201(2):375-387 (in eng).
77. Nudo RJ (2011) Neural bases of recovery after brain injury. (Translated from eng) *J Commun Disord* 44(5):515-520 (in eng).
78. Perederiy JV & Westbrook GL (2013) Structural plasticity in the dentate gyrus-revisiting a classic injury model. (Translated from eng) *Front Neural Circuits* 7:17 (in eng).
79. Chen H, Epstein J, & Stern E (2010) Neural plasticity after acquired brain injury: evidence from functional neuroimaging. (Translated from eng) *PM R* 2(12 Suppl 2):S306-312 (in eng).
80. Arai K, Jin G, Navaratna D, & Lo EH (2009) Brain angiogenesis in developmental and pathological processes: neurovascular injury and angiogenic recovery after stroke. (Translated from eng) *FEBS J* 276(17):4644-4652 (in eng).
81. Font MA, Arboix A, & Krupinski J (2010) Angiogenesis, neurogenesis and neuroplasticity in ischemic stroke. (Translated from eng) *Curr Cardiol Rev* 6(3):238-244 (in eng).
82. Krum JM, Mani N, & Rosenstein JM (2008) Roles of the endogenous VEGF receptors flt-1 and flk-1 in astroglial and vascular remodeling after brain injury. (Translated from eng) *Exp Neurol* 212(1):108-117 (in eng).
83. Bolognini N, Pascual-Leone A, & Fregni F (2009) Using non-invasive brain stimulation to augment motor training-induced plasticity. (Translated from eng) *J Neuroeng Rehabil* 6:8 (in eng).
84. Carey JR, Fregni F, & Pascual-Leone A (2006) rTMS combined with motor learning training in healthy subjects. (Translated from eng) *Restor Neurol Neurosci* 24(3):191-199 (in eng).
85. Liebetanz D, Nitsche MA, Tergau F, & Paulus W (2002) Pharmacological approach to the mechanisms of transcranial DC-stimulation-induced after-effects of human motor cortex excitability. (Translated from eng) *Brain* 125(Pt 10):2238-2247 (in eng).
86. Chaieb L, Antal A, Terney D, & Paulus W (2012) Pharmacological modulation of the short-lasting effects of antagonistic direct current-stimulation over the human motor cortex. (Translated from eng) *Front Psychiatry* 3:67 (in eng).
87. Stagg CJ, Bachtar V, & Johansen-Berg H (2011) The role of GABA in human motor learning. (Translated from eng) *Curr Biol* 21(6):480-484 (in eng).
88. Ruohonen J & Karhu J (2012) tDCS possibly stimulates glial cells. (Translated from eng) *Clin Neurophysiol* 123(10):2006-2009 (in eng).
89. Edwards DJ, *et al.* (2009) Raised corticomotor excitability of M1 forearm area following anodal tDCS is sustained during robotic wrist therapy in chronic stroke. (Translated from eng) *Restorative neurology and neuroscience* 27(3):199-207 (in eng).

90. Williams JA, Pascual-Leone A, & Fregni F (2010) Interhemispheric modulation induced by cortical stimulation and motor training. (Translated from eng) *Physical therapy* 90(3):398-410 (in eng).
91. Amadi U, Ilie A, Johansen-Berg H, & Stagg CJ (2013) Polarity-specific effects of motor transcranial direct current stimulation on fMRI resting state networks. (Translated from Eng) *Neuroimage* 88C:155-161 (in Eng).
92. Reis J, *et al.* (2008) Consensus: "Can tDCS and TMS enhance motor learning and memory formation?". (Translated from Eng) *Brain Stimul* 1(4):363-369 (in Eng).
93. Mahmoudi H, *et al.* (2011) Transcranial direct current stimulation: electrode montage in stroke. (Translated from eng) *Disabil Rehabil* 33(15-16):1383-1388 (in eng).
94. Kang EK & Paik NJ (2011) Effect of a tDCS electrode montage on implicit motor sequence learning in healthy subjects. (Translated from eng) *Experimental & translational stroke medicine* 3(1):4 (in eng).
95. Bunce SC, Izzetoglu M, Izzetoglu K, Onaral B, & Pourrezaei K (2006) Functional near-infrared spectroscopy. (Translated from eng) *IEEE Eng Med Biol Mag* 25(4):54-62 (in eng).
96. Boas DA, Dale AM, & Franceschini MA (2004) Diffuse optical imaging of brain activation: approaches to optimizing image sensitivity, resolution, and accuracy. (Translated from English) *Neuroimage* 23:S275-S288 (in English).
97. Gibson A & Dehghani H (2009) Diffuse optical imaging. (Translated from eng) *Philos Transact A Math Phys Eng Sci* 367(1900):3055-3072 (in eng).
98. Gibson AP, Hebden JC, & Arridge SR (2005) Recent advances in diffuse optical imaging. (Translated from eng) *Phys Med Biol* 50(4):R1-43 (in eng).
99. Franceschini MA, Fantini S, Thompson JH, Culver JP, & Boas DA (2003) Hemodynamic evoked response of the sensorimotor cortex measured noninvasively with near-infrared optical imaging. (Translated from eng) *Psychophysiology* 40(4):548-560 (in eng).
100. Huppert TJ, Hoge RD, Diamond SG, Franceschini MA, & Boas DA (2006) A temporal comparison of BOLD, ASL, and NIRS hemodynamic responses to motor stimuli in adult humans. (Translated from eng) *NeuroImage* 29(2):368-382 (in eng).
101. Strangman G, Franceschini MA, & Boas DA (2003) Factors affecting the accuracy of near-infrared spectroscopy concentration calculations for focal changes in oxygenation parameters. (Translated from eng) *NeuroImage* 18(4):865-879 (in eng).
102. Strangman G, Culver JP, Thompson JH, & Boas DA (2002) A quantitative comparison of simultaneous BOLD fMRI and NIRS recordings during functional brain activation. (Translated from eng) *NeuroImage* 17(2):719-731 (in eng).
103. Girouard H & Iadecola C (2006) Neurovascular coupling in the normal brain and in hypertension, stroke, and Alzheimer disease. (Translated from eng) *J Appl Physiol (1985)* 100(1):328-335 (in eng).
104. Filosa JA & Blanco VM (2007) Neurovascular coupling in the mammalian brain. (Translated from eng) *Exp Physiol* 92(4):641-646 (in eng).
105. Paemeleire K (2002) The cellular basis of neurovascular metabolic coupling. (Translated from eng) *Acta Neurol Belg* 102(4):153-157 (in eng).
106. Vannucci SJ, Maher F, & Simpson IA (1997) Glucose transporter proteins in brain: delivery of glucose to neurons and glia. (Translated from eng) *Glia* 21(1):2-21 (in eng).

107. Magistretti PJ & Pellerin L (1999) Cellular mechanisms of brain energy metabolism and their relevance to functional brain imaging. (Translated from eng) *Philos Trans R Soc Lond B Biol Sci* 354(1387):1155-1163 (in eng).
108. Benarroch EE (2005) Neuron-astrocyte interactions: partnership for normal function and disease in the central nervous system. (Translated from eng) *Mayo Clin Proc* 80(10):1326-1338 (in eng).
109. Fox PT & Raichle ME (1986) Focal physiological uncoupling of cerebral blood flow and oxidative metabolism during somatosensory stimulation in human subjects. (Translated from eng) *Proc Natl Acad Sci U S A* 83(4):1140-1144 (in eng).
110. Cooper R, Crow HJ, Walter WG, & Winter AL (1966) Regional control of cerebral vascular reactivity and oxygen supply in man. (Translated from eng) *Brain Res* 3(2):174-191 (in eng).
111. Koehler RC, Roman RJ, & Harder DR (2009) Astrocytes and the regulation of cerebral blood flow. (Translated from eng) *Trends Neurosci* 32(3):160-169 (in eng).
112. Lin PY, Chen JJ, & Lin SI (2013) The cortical control of cycling exercise in stroke patients: an fNIRS study. (Translated from eng) *Hum Brain Mapp* 34(10):2381-2390 (in eng).
113. Fujimoto H, *et al.* (2014) Cortical changes underlying balance recovery in patients with hemiplegic stroke. (Translated from eng) *Neuroimage* 85 Pt 1:547-554 (in eng).
114. Miyai I, *et al.* (2002) Premotor cortex is involved in restoration of gait in stroke. (Translated from eng) *Ann Neurol* 52(2):188-194 (in eng).
115. Strangman G, Goldstein R, Rauch SL, & Stein J (2006) Near-infrared spectroscopy and imaging for investigating stroke rehabilitation: test-retest reliability and review of the literature. (Translated from eng) *Arch Phys Med Rehabil* 87(12 Suppl 2):S12-19 (in eng).
116. Terborg C, *et al.* (2009) Noninvasive assessment of cerebral perfusion and oxygenation in acute ischemic stroke by near-infrared spectroscopy. (Translated from eng) *Eur Neurol* 62(6):338-343 (in eng).
117. Bai X, Liu Z, Zhang N, Chen W, & He B (2009) Three-dimensional source imaging from simultaneously recorded ERP and BOLD-fMRI. (Translated from eng) *IEEE Trans Neural Syst Rehabil Eng* 17(2):101-106 (in eng).
118. Li K, Guo L, Nie J, Li G, & Liu T (2009) Review of methods for functional brain connectivity detection using fMRI. (Translated from eng) *Comput Med Imaging Graph* 33(2):131-139 (in eng).
119. Muehllehner G & Karp JS (2006) Positron emission tomography. (Translated from eng) *Phys Med Biol* 51(13):R117-137 (in eng).
120. Dilharreguy B, Jones RA, & Moonen CT (2003) Influence of fMRI data sampling on the temporal characterization of the hemodynamic response. (Translated from eng) *NeuroImage* 19(4):1820-1828 (in eng).
121. Abdelnour F, Schmidt B, & Huppert TJ (2009) Topographic localization of brain activation in diffuse optical imaging using spherical wavelets. (Translated from eng) *Phys Med Biol* 54(20):6383-6413 (in eng).
122. Koch SP, *et al.* (2010) High-resolution optical functional mapping of the human somatosensory cortex. (Translated from eng) *Front Neuroenergetics* 2:12 (in eng).

123. Izzetoglu M, Devaraj A, Bunce S, & Onaral B (2005) Motion artifact cancellation in NIR spectroscopy using Wiener filtering. (Translated from eng) *IEEE Trans Biomed Eng* 52(5):934-938 (in eng).
124. Suto T, Fukuda M, Ito M, Uehara T, & Mikuni M (2004) Multichannel near-infrared spectroscopy in depression and schizophrenia: cognitive brain activation study. (Translated from eng) *Biol Psychiatry* 55(5):501-511 (in eng).
125. Khan B, *et al.* (2010) Identification of abnormal motor cortex activation patterns in children with cerebral palsy by functional near-infrared spectroscopy. (Translated from eng) *J Biomed Opt* 15(3):036008 (in eng).
126. Tian F, *et al.* (2010) Quantification of functional near infrared spectroscopy to assess cortical reorganization in children with cerebral palsy. (Translated from eng) *Opt Express* 18(25):25973-25986 (in eng).
127. Burns DH, *et al.* (2009) Near-infrared spectroscopy of blood plasma for diagnosis of sporadic Alzheimer's disease. (Translated from eng) *J Alzheimers Dis* 17(2):391-397 (in eng).
128. Kubota M, *et al.* (2008) Fast (100-175 ms) components elicited bilaterally by language production as measured by three-wavelength optical imaging. (Translated from eng) *Brain Res* 1226:124-133 (in eng).
129. Zhang Q, Yan X, & Strangman GE (2011) Development of motion resistant instrumentation for ambulatory near-infrared spectroscopy. (Translated from eng) *J Biomed Opt* 16(8):087008 (in eng).
130. Schytz HW, Ciftci K, Akin A, Ashina M, & Bolay H (2010) Intact neurovascular coupling during executive function in migraine without aura: interictal near-infrared spectroscopy study. (Translated from eng) *Cephalalgia* 30(4):457-466 (in eng).
131. Orihuela-Espina F, Leff DR, James DR, Darzi AW, & Yang GZ (2010) Quality control and assurance in functional near infrared spectroscopy (fNIRS) experimentation. (Translated from eng) *Phys Med Biol* 55(13):3701-3724 (in eng).
132. Barman JM, Astore I, & Pecoraro V (1965) THE NORMAL TRICHOGRAM OF THE ADULT. (Translated from eng) *J Invest Dermatol* 44:233-236 (in eng).
133. Khan B, *et al.* (2011) Functional near infrared brain imaging with a brush-fiber optode to improve optical contact on subjects with dense hair. eds Kollias N, Choi B, Zeng H, Kang HW, Knudsen BE, Wong BJ, Ilgner JFR, Gregory KW, Tearney GJ, Marcu L, *et al.* (SPIE), pp 78834V-78811.
134. Franceschini MA, Joseph DK, Huppert TJ, Diamond SG, & Boas DA (2006) Diffuse optical imaging of the whole head. (Translated from eng) *J Biomed Opt* 11(5):054007 (in eng).
135. Julien C (2006) The enigma of Mayer waves: Facts and models. (Translated from eng) *Cardiovasc Res* 70(1):12-21 (in eng).
136. Selb J, Fau - Stott JJ, *et al.* (Improved sensitivity to cerebral hemodynamics during brain activation with a time-gated optical system: analytical model and experimental validation
Brain specificity of diffuse optical imaging: improvements from superficial signal regression and tomography. LID - 14 [pii]. (Translated from eng) (1083-3668 (Print)) (in eng).
137. Gregg NM, White BR, Zeff BW, Berger AJ, & Culver JP (2010) Brain specificity of diffuse optical imaging: improvements from superficial signal regression and tomography. (Translated from eng) *Front Neuroenergetics* 2 (in eng).

138. Morren G, *et al.* (2004) Detection of fast neuronal signals in the motor cortex from functional near infrared spectroscopy measurements using independent component analysis. (Translated from eng) *Med Biol Eng Comput* 42(1):92-99 (in eng).
139. Zhang Q, Brown EN, & Strangman GE (2007) Adaptive filtering for global interference cancellation and real-time recovery of evoked brain activity: a Monte Carlo simulation study. (Translated from eng) *J Biomed Opt* 12(4):044014 (in eng).
140. Khan B, Chand P, & Alexandrakis G (2011) Spatiotemporal relations of primary sensorimotor and secondary motor activation patterns mapped by NIR imaging. *Biomed. Opt. Express* 2(12):3367-3386.
141. Huppert TJ, Diamond SG, Franceschini MA, & Boas DA (2009) HomER: a review of time-series analysis methods for near-infrared spectroscopy of the brain. (Translated from eng) *Appl Opt* 48(10):D280-298 (in eng).
142. Brooksby B, *et al.* (2005) Spectral priors improve near-infrared diffuse tomography more than spatial priors. (Translated from eng) *Opt Lett* 30(15):1968-1970 (in eng).
143. Li A, Zhang Q, Culver JP, Miller EL, & Boas DA (2004) Reconstructing chromosphere concentration images directly by continuous-wave diffuse optical tomography. (Translated from eng) *Opt Lett* 29(3):256-258 (in eng).
144. Beckmann CF, Jenkinson M, & Smith SM (2003) General multilevel linear modeling for group analysis in fMRI. (Translated from eng) *NeuroImage* 20(2):1052-1063 (in eng).
145. Abdelnour AF & Huppert T (2009) Real-time imaging of human brain function by near-infrared spectroscopy using an adaptive general linear model. (Translated from eng) *NeuroImage* 46(1):133-143 (in eng).
146. Singh AK & Dan I (2006) Exploring the false discovery rate in multichannel NIRS. (Translated from eng) *NeuroImage* 33(2):542-549 (in eng).
147. Tseng SH, Bargo P, Durkin A, & Kollias N (2009) Chromophore concentrations, absorption and scattering properties of human skin in-vivo. (Translated from eng) *Opt Express* 17(17):14599-14617 (in eng).
148. Jimenez F, Izeta A, & Poblet E (2011) Morphometric analysis of the human scalp hair follicle: practical implications for the hair transplant surgeon and hair regeneration studies. (Translated from eng) *Dermatol Surg* 37(1):58-64 (in eng).
149. Kharin A, Varghese B, Verhagen R, & Uzunbajakava N (2009) Optical properties of the medulla and the cortex of human scalp hair. (Translated from eng) *J Biomed Opt* 14(2):024035 (in eng).
150. Cuccia DJ, Bevilacqua F, Durkin AJ, Ayers FR, & Tromberg BJ (2009) Quantitation and mapping of tissue optical properties using modulated imaging. (Translated from eng) *J Biomed Opt* 14(2):024012 (in eng).
151. Haskell RC, *et al.* (1994) Boundary conditions for the diffusion equation in radiative transfer. (Translated from eng) *J Opt Soc Am A Opt Image Sci Vis* 11(10):2727-2741 (in eng).
152. Knoll FK (1988) *Radiation detection and measurement* (John Wiley & Sons, New York-Chichester-Brisbane-Toronto-Singapore).
153. Cheong WF, Prahl SA, & Welch AJ (1990) A review of the optical properties of biological tissues. *Quantum Electronics, IEEE Journal of* 26(12):2166-2185.
154. Yudovsky D & Pilon L (2010) Modeling the local excitation fluence rate and fluorescence emission in absorbing and strongly scattering multilayered media. *Appl. Opt.* 49(31):6072-6084.

155. Mylius V, Zouari HG, Ayache SS, Farhat WH, & Lefaucheur JP (2012) Stroke rehabilitation using noninvasive cortical stimulation: aphasia. (Translated from eng) *Expert review of neurotherapeutics* 12(8):973-982 (in eng).
156. Hummel FC, et al. (2010) Facilitating skilled right hand motor function in older subjects by anodal polarization over the left primary motor cortex. (Translated from eng) *Neurobiol Aging* 31(12):2160-2168 (in eng).
157. Hummel FC, et al. (2006) Effects of brain polarization on reaction times and pinch force in chronic stroke. (Translated from eng) *BMC neuroscience* 7:73 (in eng).
158. Tretriluxana J, Kantak S, Tretriluxana S, Wu AD, & Fisher BE (2012) Low frequency repetitive transcranial magnetic stimulation to the non-lesioned hemisphere improves paretic arm reach-to-grasp performance after chronic stroke. (Translated from Eng) *Disability and rehabilitation. Assistive technology* (in Eng).
159. Zimerman M, et al. (2012) Modulation of training by single-session transcranial direct current stimulation to the intact motor cortex enhances motor skill acquisition of the paretic hand. (Translated from eng) *Stroke; a journal of cerebral circulation* 43(8):2185-2191 (in eng).
160. Ragert P, Vandermeeren Y, Camus M, & Cohen LG (2008) Improvement of spatial tactile acuity by transcranial direct current stimulation. (Translated from eng) *Clinical neurophysiology : official journal of the International Federation of Clinical Neurophysiology* 119(4):805-811 (in eng).
161. Song S, Sandrini M, & Cohen LG (2011) Modifying somatosensory processing with non-invasive brain stimulation. (Translated from eng) *Restorative neurology and neuroscience* 29(6):427-437 (in eng).
162. Keeser D, et al. (2011) Prefrontal transcranial direct current stimulation changes connectivity of resting-state networks during fMRI. (Translated from eng) *The Journal of neuroscience : the official journal of the Society for Neuroscience* 31(43):15284-15293 (in eng).
163. Pena-Gomez C, et al. (2012) Modulation of large-scale brain networks by transcranial direct current stimulation evidenced by resting-state functional MRI. (Translated from eng) *Brain stimulation* 5(3):252-263 (in eng).
164. Polania R, Nitsche MA, & Paulus W (2011) Modulating functional connectivity patterns and topological functional organization of the human brain with transcranial direct current stimulation. (Translated from eng) *Human brain mapping* 32(8):1236-1249 (in eng).
165. Polania R, Paulus W, & Nitsche MA (2012) Reorganizing the intrinsic functional architecture of the human primary motor cortex during rest with non-invasive cortical stimulation. (Translated from eng) *PLoS one* 7(1):e30971 (in eng).
166. Paquette C, Sidel M, Radinska BA, Soucy JP, & Thiel A (2011) Bilateral transcranial direct current stimulation modulates activation-induced regional blood flow changes during voluntary movement. (Translated from eng) *Journal of cerebral blood flow and metabolism : official journal of the International Society of Cerebral Blood Flow and Metabolism* 31(10):2086-2095 (in eng).
167. Nitsche MA, et al. (2005) Modulating parameters of excitability during and after transcranial direct current stimulation of the human motor cortex. (Translated from eng) *J Physiol* 568(Pt 1):291-303 (in eng).
168. Nitsche MA & Paulus W (2000) Excitability changes induced in the human motor cortex by weak transcranial direct current stimulation. (Translated from eng) *J Physiol* 527 Pt 3:633-639 (in eng).

169. Priori A, Berardelli A, Rona S, Accornero N, & Manfredi M (1998) Polarization of the human motor cortex through the scalp. (Translated from eng) *Neuroreport* 9(10):2257-2260 (in eng).
170. Antal A, *et al.* (2012) Cathodal stimulation of human MT+ leads to elevated fMRI signal: a tDCS-fMRI study. (Translated from eng) *Restorative neurology and neuroscience* 30(3):255-263 (in eng).
171. Lang N, *et al.* (2005) How does transcranial DC stimulation of the primary motor cortex alter regional neuronal activity in the human brain? (Translated from eng) *The European journal of neuroscience* 22(2):495-504 (in eng).
172. Antal A, Polania R, Schmidt-Samoa C, Dechent P, & Paulus W (2011) Transcranial direct current stimulation over the primary motor cortex during fMRI. (Translated from eng) *NeuroImage* 55(2):590-596 (in eng).
173. Holland R, *et al.* (2011) Speech facilitation by left inferior frontal cortex stimulation. (Translated from eng) *Curr Biol* 21(16):1403-1407 (in eng).
174. Antal A, *et al.* (2012) Imaging artifacts induced by electrical stimulation during conventional fMRI of the brain. (Translated from Eng) *NeuroImage* (in Eng).
175. Holper L, Biallas M, & Wolf M (2009) Task complexity relates to activation of cortical motor areas during uni- and bimanual performance: a functional NIRS study. (Translated from eng) *NeuroImage* 46(4):1105-1113 (in eng).
176. C. Terborg KG, A. Petrovitch, T. Ringer, S. Schnaudigel, O. W. Witte, and A. Kastrup (2009) Noninvasive Assessment of Cerebral Perfusion and Oxygenation in Acute Ischemic Stroke by Near-Infrared Spectroscopy. *Eur. Neurol.* 62:6.
177. Villringer A (1997) Understanding functional neuroimaging methods based on neurovascular coupling. (Translated from eng) *Adv Exp Med Biol* 413:177-193 (in eng).
178. Oldfield RC (1971) The assessment and analysis of handedness: the Edinburgh inventory. (Translated from eng) *Neuropsychologia* 9(1):97-113 (in eng).
179. Poreisz C, Boros K, Antal A, & Paulus W (2007) Safety aspects of transcranial direct current stimulation concerning healthy subjects and patients. (Translated from eng) *Brain Res Bull* 72(4-6):208-214 (in eng).
180. Klem GH, Luders HO, Jasper HH, & Elger C (1999) The ten-twenty electrode system of the International Federation. The International Federation of Clinical Neurophysiology. (Translated from eng) *Electroencephalogr Clin Neurophysiol Suppl* 52:3-6 (in eng).
181. Gelnar PA, Krauss BR, Sheehe PR, Szeverenyi NM, & Apkarian AV (1999) A comparative fMRI study of cortical representations for thermal painful, vibrotactile, and motor performance tasks. (Translated from eng) *NeuroImage* 10(4):460-482 (in eng).
182. Lepage M, *et al.* (1999) Frontal cortex and the programming of repetitive tapping movements in man: lesion effects and functional neuroimaging. (Translated from eng) *Brain Res Cogn Brain Res* 8(1):17-25 (in eng).
183. Hansson T & Brismar T (1999) Tactile stimulation of the hand causes bilateral cortical activation: a functional magnetic resonance study in humans. (Translated from eng) *Neuroscience letters* 271(1):29-32 (in eng).
184. Praamstra P & Oostenveld R (2003) Attention and movement-related motor cortex activation: a high-density EEG study of spatial stimulus-response compatibility. (Translated from eng) *Brain Res Cogn Brain Res* 16(3):309-322 (in eng).

185. Boggio PS, *et al.* (2006) Enhancement of non-dominant hand motor function by anodal transcranial direct current stimulation. (Translated from eng) *Neuroscience letters* 404(1-2):232-236 (in eng).
186. M. F. Folstein aRL (1973) Reliability, validity, and clinical application of the Visual Analogue Mood Scale. *Psychological Medicine* 3:479–486.
187. Floel A, *et al.* (2004) Influence of somatosensory input on motor function in patients with chronic stroke. (Translated from eng) *Ann Neurol* 56(2):206-212 (in eng).
188. B. Khan FT, K. Behbehani, M. I. Romero, M. R. Delgado, N. J. Clegg, L. Smith, D. Reid, H. Liu, and G. Alexandrakis (2010) Identification of abnormal motor cortex activation patterns in children with cerebral palsy by functional near-infrared spectroscopy. *J. Biomed. Opt* 15(3):14.
189. T. J. Huppert RDHSGD, M. A. Franceschini, and D. A. Boas (2006) A temporal comparison of BOLD, ASL, and NIRS hemodynamic responses to motor stimuli in adult humans. *NeuroImage* 29:15.
190. Stam CJ, Jones BF, Nolte G, Breakspear M, & Scheltens P (2007) Small-world networks and functional connectivity in Alzheimer's disease. (Translated from eng) *Cerebral cortex (New York, N.Y. : 1991)* 17(1):92-99 (in eng).
191. Sanz-Arigita EJ, *et al.* (2010) Loss of 'small-world' networks in Alzheimer's disease: graph analysis of fMRI resting-state functional connectivity. (Translated from eng) *PLoS one* 5(11):e13788 (in eng).
192. Luca CJD (1997) The use of surface electromyography in biomechanics. *Journal of Applied Biomechanics* 13(2):135-163.
193. Suminski AJ, Zimbelman JL, & Scheidt RA (2007) Design and validation of a MR-compatible pneumatic manipulandum. (Translated from eng) *Journal of neuroscience methods* 163(2):255-266 (in eng).
194. Leite J, Carvalho S, Fregni F, & Goncalves OF (2011) Task-specific effects of tDCS-induced cortical excitability changes on cognitive and motor sequence set shifting performance. (Translated from eng) *PLoS one* 6(9):e24140 (in eng).
195. Stagg CJ, *et al.* (2011) Polarity and timing-dependent effects of transcranial direct current stimulation in explicit motor learning. (Translated from eng) *Neuropsychologia* 49(5):800-804 (in eng).
196. Muellbacher W, *et al.* (2002) Early consolidation in human primary motor cortex. (Translated from eng) *Nature* 415(6872):640-644 (in eng).
197. Stefan K, *et al.* (2006) Temporary occlusion of associative motor cortical plasticity by prior dynamic motor training. (Translated from eng) *Cerebral cortex (New York, N.Y. : 1991)* 16(3):376-385 (in eng).
198. Ziemann U, Ilic TV, Pauli C, Meintzschel F, & Ruge D (2004) Learning modifies subsequent induction of long-term potentiation-like and long-term depression-like plasticity in human motor cortex. (Translated from eng) *The Journal of neuroscience : the official journal of the Society for Neuroscience* 24(7):1666-1672 (in eng).
199. Abbott LF & Nelson SB (2000) Synaptic plasticity: taming the beast. (Translated from eng) *Nat Neurosci* 3 Suppl:1178-1183 (in eng).
200. Bienenstock EL, Cooper LN, & Munro PW (1982) Theory for the development of neuron selectivity: orientation specificity and binocular interaction in visual cortex. (Translated from eng) *The Journal of neuroscience : the official journal of the Society for Neuroscience* 2(1):32-48 (in eng).
201. Sejnowski TJ (1977) Statistical constraints on synaptic plasticity. (Translated from eng) *J Theor Biol* 69(2):385-389 (in eng).

202. Abraham WC, Mason-Parker SE, Bear MF, Webb S, & Tate WP (2001) Heterosynaptic metaplasticity in the hippocampus in vivo: a BCM-like modifiable threshold for LTP. (Translated from eng) *Proc Natl Acad Sci U S A* 98(19):10924-10929 (in eng).
203. Lang N, *et al.* (2004) Preconditioning with transcranial direct current stimulation sensitizes the motor cortex to rapid-rate transcranial magnetic stimulation and controls the direction of after-effects. (Translated from eng) *Biol Psychiatry* 56(9):634-639 (in eng).
204. Siebner HR, *et al.* (2004) Preconditioning of low-frequency repetitive transcranial magnetic stimulation with transcranial direct current stimulation: evidence for homeostatic plasticity in the human motor cortex. (Translated from eng) *The Journal of neuroscience : the official journal of the Society for Neuroscience* 24(13):3379-3385 (in eng).
205. Gandiga PC, Hummel FC, & Cohen LG (2006) Transcranial DC stimulation (tDCS): a tool for double-blind sham-controlled clinical studies in brain stimulation. (Translated from eng) *Clinical neurophysiology : official journal of the International Federation of Clinical Neurophysiology* 117(4):845-850 (in eng).
206. Kessler SK, Turkeltaub PE, Benson JG, & Hamilton RH (2012) Differences in the experience of active and sham transcranial direct current stimulation. (Translated from eng) *Brain stimulation* 5(2):155-162 (in eng).
207. Ambrus GG, *et al.* (2012) The fade-in--short stimulation--fade out approach to sham tDCS--reliable at 1 mA for naive and experienced subjects, but not investigators. (Translated from eng) *Brain stimulation* 5(4):499-504 (in eng).
208. Brunoni AR, Schestatsky P, Lotufo PA, Bensenor IM, & Fregni F (2014) Comparison of blinding effectiveness between sham tDCS and placebo sertraline in a 6-week major depression randomized clinical trial. (Translated from eng) *Clinical neurophysiology : official journal of the International Federation of Clinical Neurophysiology* 125(2):298-305 (in eng).
209. Davis NJ & van Koningsbruggen MG (2013) "Non-invasive" brain stimulation is not non-invasive. (Translated from eng) *Front Syst Neurosci* 7:76 (in eng).
210. Palm U, *et al.* (2013) Evaluation of sham transcranial direct current stimulation for randomized, placebo-controlled clinical trials. (Translated from eng) *Brain stimulation* 6(4):690-695 (in eng).
211. O'Connell NE, *et al.* (2013) Transcranial direct current stimulation of the motor cortex in the treatment of chronic nonspecific low back pain: a randomized, double-blind exploratory study. (Translated from eng) *Clin J Pain* 29(1):26-34 (in eng).
212. Lee MY, *et al.* (2009) Cortical activation pattern of compensatory movement in stroke patients. (Translated from eng) *NeuroRehabilitation* 25(4):255-260 (in eng).
213. Bikson M, Datta A, & Elwassif M (2009) Establishing safety limits for transcranial direct current stimulation. (Translated from eng) *Clinical neurophysiology : official journal of the International Federation of Clinical Neurophysiology* 120(6):1033-1034 (in eng).
214. Nitsche MA, *et al.* (2004) MRI study of human brain exposed to weak direct current stimulation of the frontal cortex. (Translated from eng) *Clinical neurophysiology : official journal of the International Federation of Clinical Neurophysiology* 115(10):2419-2423 (in eng).
215. Miranda PC, Faria P, & Hallett M (2009) What does the ratio of injected current to electrode area tell us about current density in the brain during tDCS? (Translated

- from eng) *Clinical neurophysiology : official journal of the International Federation of Clinical Neurophysiology* 120(6):1183-1187 (in eng).
216. Faria P, Hallett M, & Miranda PC (2011) A finite element analysis of the effect of electrode area and inter-electrode distance on the spatial distribution of the current density in tDCS. (Translated from eng) *J Neural Eng* 8(6):066017 (in eng).
217. Datta A, Elwassif M, Battaglia F, & Bikson M (2008) Transcranial current stimulation focality using disc and ring electrode configurations: FEM analysis. (Translated from eng) *J Neural Eng* 5(2):163-174 (in eng).
218. Suh HS, Lee WH, & Kim TS (2012) Influence of anisotropic conductivity in the skull and white matter on transcranial direct current stimulation via an anatomically realistic finite element head model. (Translated from eng) *Phys Med Biol* 57(21):6961-6980 (in eng).
219. Edwards D, *et al.* (2013) Physiological and modeling evidence for focal transcranial electrical brain stimulation in humans: a basis for high-definition tDCS. (Translated from eng) *NeuroImage* 74:266-275 (in eng).
220. Parazzini M, *et al.* (2014) Modelling the electric field and the current density generated by cerebellar transcranial DC stimulation in humans. (Translated from eng) *Clinical neurophysiology : official journal of the International Federation of Clinical Neurophysiology* 125(3):577-584 (in eng).
221. Bastani A & Jaberzadeh S (2013) a-tDCS differential modulation of corticospinal excitability: the effects of electrode size. (Translated from eng) *Brain stimulation* 6(6):932-937 (in eng).
222. Villamar MF, *et al.* (2013) Technique and considerations in the use of 4x1 ring high-definition transcranial direct current stimulation (HD-tDCS). (Translated from eng) *J Vis Exp* (77):e50309 (in eng).
223. Xu Y, Graber HL, & Barbour RL (2007) Image correction algorithm for functional three-dimensional diffuse optical tomography brain imaging. (Translated from eng) *Applied optics* 46(10):1693-1704 (in eng).
224. Ohta H, *et al.* (2008) Hypofrontality in panic disorder and major depressive disorder assessed by multi-channel near-infrared spectroscopy. (Translated from eng) *Depress Anxiety* 25(12):1053-1059 (in eng).
225. Takeda K, *et al.* (2007) Shift of motor activation areas during recovery from hemiparesis after cerebral infarction: a longitudinal study with near-infrared spectroscopy. (Translated from eng) *Neurosci Res* 59(2):136-144 (in eng).
226. Zeller JB, Herrmann MJ, Ehlis AC, Polak T, & Fallgatter AJ (2010) Altered parietal brain oxygenation in Alzheimer's disease as assessed with near-infrared spectroscopy. (Translated from eng) *Am J Geriatr Psychiatry* 18(5):433-441 (in eng).
227. Azpiroz J, *et al.* (2005) Game motivated and constraint induced therapy in late stroke with fMRI studies pre and post therapy. (Translated from English) *P Ann Int leee Embs*:3695-3698
7776 (in English).
228. Hamzei F, Liepert J, Dettmers C, Weiller C, & Rijntjes M (2006) Two different reorganization patterns after rehabilitative therapy: an exploratory study with fMRI and TMS. (Translated from eng) *NeuroImage* 31(2):710-720 (in eng).
229. Juenger CH, *et al.* (2007) Neuromodulation by constraint-induced movement therapy (CIMT) in congenital hemiparesis: an fMRI study. (Translated from English) *Eur J Pediatr* 166(3):280-280 (in English).

230. Juenger H, *et al.* (2007) Cortical neuromodulation by constraint-induced movement therapy in congenital hemiparesis: An fMRI study. (Translated from English) *Neuropediatrics* 38(3):130-136 (in English).
231. Izzetoglu K, Bunce S, Izzetoglu M, Onaral B, & Pourrezaei K (2004) Functional near-infrared neuroimaging. (Translated from eng) *Conf Proc IEEE Eng Med Biol Soc* 7:5333-5336 (in eng).
232. Hatakenaka M, Miyai I, Mihara M, Sakoda S, & Kubota K (2007) Frontal regions involved in learning of motor skill--A functional NIRS study. (Translated from eng) *NeuroImage* 34(1):109-116 (in eng).
233. Ikegami T & Taga G (2008) Decrease in cortical activation during learning of a multi-joint discrete motor task. (Translated from eng) *Exp Brain Res* 191(2):221-236 (in eng).
234. Holper L, Scholkmann F, Shalom DE, & Wolf M (2011) Extension of mental preparation positively affects motor imagery as compared to motor execution: A functional near-infrared spectroscopy study. (Translated from Eng) *Cortex* (in Eng).
235. Maki A, *et al.* (1995) Spatial and temporal analysis of human motor activity using noninvasive NIR topography. (Translated from eng) *Med Phys* 22(12):1997-2005 (in eng).
236. Sato H, *et al.* (2005) Intersubject variability of near-infrared spectroscopy signals during sensorimotor cortex activation. (Translated from eng) *J Biomed Opt* 10(4):44001 (in eng).
237. Toronov V, *et al.* (2000) Near-infrared study of fluctuations in cerebral hemodynamics during rest and motor stimulation: temporal analysis and spatial mapping. (Translated from eng) *Med Phys* 27(4):801-815 (in eng).
238. Chen S, Bouman CA, & Lowe MJ (2004) Clustered components analysis for functional MRI. (Translated from eng) *IEEE Trans Med Imaging* 23(1):85-98 (in eng).
239. Zhang Q, Brown EN, & Strangman GE (2007) Adaptive filtering to reduce global interference in evoked brain activity detection: a human subject case study. (Translated from eng) *J Biomed Opt* 12(6):064009 (in eng).
240. Zhang Q, Strangman GE, & Ganis G (2009) Adaptive filtering to reduce global interference in non-invasive NIRS measures of brain activation: how well and when does it work? (Translated from eng) *NeuroImage* 45(3):788-794 (in eng).
241. Zhang Y, Brooks DH, Franceschini MA, & Boas DA (2005) Eigenvector-based spatial filtering for reduction of physiological interference in diffuse optical imaging. (Translated from eng) *J Biomed Opt* 10(1):11014 (in eng).
242. Julien C (2006) The enigma of Mayer waves: facts and models. *Cardiovasc. Res.* 70:10.
243. Kohno S, *et al.* (2007) Removal of the skin blood flow artifact in functional near-infrared spectroscopic imaging data through independent component analysis. (Translated from eng) *J Biomed Opt* 12(6):062111 (in eng).
244. Robertson FC, Douglas TS, & Meintjes EM (2010) Motion artifact removal for functional near infrared spectroscopy: a comparison of methods. (Translated from eng) *IEEE Trans Biomed Eng* 57(6):1377-1387 (in eng).
245. Dorfman DD, Berbaum KS, & Metz CE (1992) Receiver Operating Characteristic Rating Analysis - Generalization to the Population of Readers and Patients with the Jackknife Method. (Translated from English) *Invest Radiol* 27(9):723-731 (in English).

246. Huppert TJ, Diamond SG, Franceschini MA, & Boas DA (2009) HomER: a review of time-series analysis methods for near-infrared spectroscopy of the brain. (Translated from English) *Applied optics* 48(10):D280-D298 (in English).
247. Baudendistel K, *et al.* (1995) Postprocessing of Functional Mri Data of Motor Cortex Stimulation Measured with a Standard 1.5 T Imager. (Translated from English) *Magn Reson Imaging* 13(5):701-707 (in English).
248. T. J. Huppert RDHSGD, M. A. Franceschini, and D. A. Boas (2007) HomER: A review of time-series analysis methods for near-infrared spectroscopy of the brain. *Appl. Opt.* 48(10):19.
249. S. P. Koch CH, J. Mehnert, C. H. Schmitz, S. Holtze, A. Villringer, J. Steinbrink, and H. Obrig (2010) High-resolution optical functional mapping of the human somatosensory cortex. *Frontiers in Neuroenergetics* 2(12):8.
250. Kuhtz-Buschbeck JP, *et al.* (2008) Brain activity is similar during precision and power gripping with light force: an fMRI study. (Translated from eng) *NeuroImage* 40(4):1469-1481 (in eng).
251. Khorrami MS, *et al.* (2011) Functional MRI of Sensory Motor Cortex: Comparison Between Finger-to-Thumb and Hand Squeeze Tasks. (Translated from eng) *J Neuroimaging* 21(3):236-240 (in eng).
252. Azanon E, Longo MR, Soto-Faraco S, & Haggard P (2010) The posterior parietal cortex remaps touch into external space. (Translated from eng) *Curr Biol* 20(14):1304-1309 (in eng).
253. Dhillon GS, Lawrence SM, Hutchinson DT, & Horch KW (2004) Residual function in peripheral nerve stumps of amputees: implications for neural control of artificial limbs. (Translated from eng) *J Hand Surg Am* 29(4):605-615; discussion 616-608 (in eng).
254. Burton H, *et al.* (1999) Tactile attention tasks enhance activation in somatosensory regions of parietal cortex: a positron emission tomography study. (Translated from eng) *Cerebral cortex (New York, N.Y. : 1991)* 9(7):662-674 (in eng).
255. Donahue MJ, *et al.* (2011) Spontaneous blood oxygenation level-dependent fMRI signal is modulated by behavioral state and correlates with evoked response in sensorimotor cortex: A 7.0-T fMRI study. (Translated from Eng) *Human brain mapping* (in Eng).
256. Deiber MP, Ibanez V, Sadato N, & Hallett M (1996) Cerebral structures participating in motor preparation in humans: a positron emission tomography study. (Translated from eng) *Journal of neurophysiology* 75(1):233-247 (in eng).
257. Van Oostende S, Van Hecke P, Sunaert S, Nuttin B, & Marchal G (1997) fMRI studies of the supplementary motor area and the premotor cortex. (Translated from eng) *NeuroImage* 6(3):181-190 (in eng).
258. Rushworth MF, Johansen-Berg H, Gobel SM, & Devlin JT (2003) The left parietal and premotor cortices: motor attention and selection. (Translated from eng) *NeuroImage* 20 Suppl 1:S89-100 (in eng).
259. Bremner F, *et al.* (2001) Polymodal motion processing in posterior parietal and premotor cortex: a human fMRI study strongly implies equivalencies between humans and monkeys. (Translated from eng) *Neuron* 29(1):287-296 (in eng).
260. Gountouna VE, *et al.* (2010) Functional Magnetic Resonance Imaging (fMRI) reproducibility and variance components across visits and scanning sites with a finger tapping task. (Translated from eng) *NeuroImage* 49(1):552-560 (in eng).

261. Stringer EA, Chen LM, Friedman RM, Gatenby C, & Gore JC (2011) Differentiation of somatosensory cortices by high-resolution fMRI at 7 T. (Translated from eng) *NeuroImage* 54(2):1012-1020 (in eng).
262. Mountcastle VB, Lynch JC, Georgopoulos A, Sakata H, & Acuna C (1975) Posterior parietal association cortex of the monkey: command functions for operations within extrapersonal space. (Translated from eng) *Journal of neurophysiology* 38(4):871-908 (in eng).
263. Mesquita RC, Franceschini MA, & Boas DA (2010) Resting state functional connectivity of the whole head with near-infrared spectroscopy. (Translated from Eng) *Biomed Opt Express* 1(1):324-336 (in Eng).
264. Kaiming Li LG, Jingxin Nie, Gang Li, and Tianming Liub (2009) Review of methods for functional brain connectivity detection using fMRI. *Computerized Medical Imaging and Graphics* 33:9.
265. Aldhaferi RW (1991) Model Order Reduction Via Real Schur-Form Decomposition. (Translated from English) *Int J Control* 53(3):709-716 (in English).

Biographical Information

Bilal Khan was born in Wichita, Kansas, on March 4, 1984. He received his Bachelors of Science in Electrical Engineering from the University of Texas at Austin in May of 2007. In the fall of 2007 he began his graduate studies in Biomedical Engineering from the joint program of biomedical engineering at the University of Texas at Arlington and the University of Texas Southwestern Medical Center at Dallas. He completed his Masters of Science in Biomedical Engineering in August 2009 and then completed his doctoral studies in May 2014. His research has been in signal processing, bioinstrumentation, and optical imaging. Since he has a passion for teaching he plans on first entering the private sector and then returning back to academia as an instructor.